



SAPIENZA
UNIVERSITÀ DI ROMA

Department of Mechanical and Aerospace Engineering
Ph.D. in Theoretical and Applied Mechanics

PH.D. THESIS

High-Fidelity Numerical Methods for Aeroacoustics Phenomena in Compressible Turbulent Flows

Supervisor

Prof. Matteo Bernardini
Prof. Emanuele Martelli

Tutor

Prof. Paolo Gualtieri

Candidate

Matteo Cimini

Cycle XXXIV

Abstract

The main objective of this dissertation is to perform high-fidelity numerical simulations of compressible turbulent flows for space applications in order to predict aeroacoustic resonance phenomena. The internal flow developing inside the Solid Rocket Motor (SRM) chamber during the ascent phase of a space launcher might cause severe pressure oscillations that could compromise the payload integrity. The formation of aerodynamic side loads owing to shock-wave/turbulent boundary-layer interaction inside the rocket nozzle might produce the same result. Aeroacoustic resonance phenomena could occur inside the system in both circumstances, producing undesirable forces that could endanger the payload and the launcher structure. As a result, accurate evaluation of the aeroacoustic feedback loop is crucial and should be considered throughout the design phase of such systems.

The endeavors of the community in this research field are motivated by a renewed interest in supersonic flights and space vehicles, as well as the resulting engineering request/demand for high-performance rocket launchers, where the problem of aeroacoustic resonance is present for a considerable part of the launchers' ascent phase and constitutes a major design constraint. Despite the knowledge of these phenomena has improved over the last decade, the problem of pressure fluctuations in SRM chambers and aerodynamic side loads in rocket nozzles, both related to an aeroacoustic feedback loop, appears to be far more complicated than previously expected, and certain essential physical mechanisms remain unclear. Moreover, given the complex flow conditions and lack of optical access, the experimental campaigns suffer from a lack of flow measurements inside both systems. Therefore, numerical simulations are an important complement to achieve a more deep understanding of these physics, allowing major unanswered issues to be addressed.

The present dissertation adopts high-fidelity numerical simulations based on the Implicit Large Eddy Simulation (ILES) and the Delayed Detached Eddy Simulation (DDES) techniques to explore the aeroacoustic resonance phenomenon in compressible turbulent flows involved in space applications. In particular, the DDES is a hybrid RANS/LES approach for simulating high-Reynolds number flows characterized by massive separation. In this methodology, the attached boundary layers are handled in RANS mode, which reduces the computational effort, while the most energetic turbulent scales of separated shear layers and turbulent recirculating zones are handled by the LES mode.

The potential of ILES is first tested on the ONERA C1xb solid rocket motor configuration, for which experimental and numerical studies are available, with the prime aim of emphasizing the capability of the full-scale 3D approach to capture the aeroacoustic resonance, the transition to turbulence of the coherent azimuthal vortices detached by the propellant grain, as well as its influence on the induced acoustic feedback, quantified through the level of pressure oscillation. The results indicate that the ILES is able to capture the transition to turbulence, the vortex shedding and the aeroacoustic feedback phenomena inside the SRM chamber. The pressure oscillation RMS is in excellent agreement with the experimental data. The Fourier spectral analysis in time reveals that the detached shear layer is locked on the second acoustic longitudinal mode while the vortex shedding frequency is locked on the third acoustic longitudinal one. These results are also confirmed by the space-time correlation analysis.

The study then focuses on the investigation of the aeroacoustic feedback loop and the flow

unsteadiness in a 3D sub-scale Dual-Bell nozzle, exploiting the DDES methodology. For this nozzle configuration, experimental data are available. In this situation, the analysis concentrates on the DDES capability to detect and reproduce the unsteady flow features in order to determine the intensity of the side loads inside the nozzle, which are generated by an aeroacoustic resonance through the presence of an asymmetric mode of the wall-pressure fluctuations. For this reason, the impact of the dual-bell inflection point on the aeroacoustic feedback loop is inspected. The numerical data agree well with the experimental results in terms of mean and fluctuating wall-pressure statistics. The frequency spectra are characterized by the presence of a persistent large bump in the low-frequency range associated with an axi-symmetric (piston-like) motion of the shock system and a broad and high-amplitude peak at higher frequencies generated by the turbulent activity of the detached shear layer. The presence of the axi-symmetric mode induces thrust oscillations, as occurs for the internal ballistics of SRMs. The Fourier-based spectral analysis, performed in both time and azimuthal wavenumber space, reveals also the presence of a small first (non-symmetrical) pressure mode and its role in the generation of the aerodynamic side loads.

Contents

List of Figures	v
List of Tables	viii
Acronyms	x
1 Introduction	1
1.1 Aeroacoustic Feedback Coupling	2
1.2 Solid Rocket Motor Flow	3
1.2.1 Taylor Flow	7
1.2.2 Hydrodynamic Instabilities and Vortex Shedding	9
1.3 Nozzle Flow	12
1.3.1 Nozzle Configurations	15
1.3.2 Side Loads Generation	20
1.4 High-Fidelity Numerical Simulations	22
1.5 Scope and outline of the thesis	23
2 Governing equations	25
2.1 Continuity	25
2.2 Momentum	26
2.3 Energy	26
3 Methodology	28
3.1 Reynolds Averaged Navier-Stokes Simulations	28
3.1.1 Averaged Equations of Motion	29
3.1.2 RANS Turbulence Modeling	32
3.2 Large-Eddy Simulations (LES)	35
3.2.1 The Smagorinsky Model	37
3.2.2 Implicit LES (ILES)	37
3.3 Hybrid Methods Simulations	38
3.4 Detached Eddy Simulations (DES)	38
3.4.1 DES97	40
3.4.2 DES weaknesses	41
3.4.3 Delayed Detached Eddy Simulations (DDES)	45
4 Finite Volume Solver	48
4.1 Discretization procedure	48
4.2 Discretization of convective terms	50
4.3 WENO Reconstruction	53
4.4 Viscous fluxes	55
4.5 Runge-Kutta time-integration	56
4.6 Implicit treatment of j fluxes	57

4.6.1	Semi-implicit treatment of viscous terms	58
4.6.2	Semi-implicit treatment of convective terms	60
4.6.3	Final semi-implicit scheme	62
4.7	Numerical boundary conditions	63
4.8	Parallelization	66
5	ONERA C1xb SRM	67
5.1	Test case description	67
5.2	Computational strategy	69
5.3	Results	70
5.3.1	Flowfield organization	70
5.3.2	Analysis of the wall-pressure signature	72
5.3.3	Acoustic feedback frequency	79
6	Dual Bell Nozzle	81
6.1	Test case description	81
6.2	Computational strategy	83
6.3	Results	85
6.3.1	Flowfield organisation	85
6.3.2	Analysis of the wall-pressure signature	87
6.3.3	Azimuthal decomposition of the pressure field	91
6.3.4	Aerodynamic loads distribution	95
7	Conclusions and future work	100
A	Transforms	104
A.1	Fourier Transform	104
A.1.1	Transform and Inverse Transform	104
A.1.2	Convolution Theorem	104
A.1.3	Parseval's theorem	105
A.1.4	Basic properties	106
A.1.5	Extension to the n -dimensional Case	106
B	Numerical Issues	107
B.1	Lax-Friedrichs Flux Splitting	107
B.2	WENO Reconstruction	108
B.3	Runge-Kutta time-integration	110
B.3.1	Explicit Runge-Kutta Methods	110
Bibliography		112

List of Figures

1.1	Sketch of the four processes of the aeroacoustic feedback resonance loop.	3
1.2	Sketch of a generic Solid Rocket Motor.	4
1.3	Schematic of SRMs surface grain combustion physical process.	5
1.4	Radial grain configurations and thrust curves in time.	6
1.5	Schematic of SMRs surface grain progression.	6
1.6	Head-end pressure of a generic SRM: (left) whole operative life and (right) ignition transient.	7
1.7	Schematic of the theoretical problem of the Taylor flow.	8
1.8	Representation in the x-r plane of the streamlines and axial velocity magnitude of the Taylor flow.	8
1.9	Schematic of the corner vortex shedding.	9
1.10	Schematic of the obstacle vortex shedding.	10
1.11	Schematic of the parietal vortex shedding.	10
1.12	Schematic of the experimental setup for the ONERA C1xb SRM.	11
1.13	Sketch of a nozzle.	12
1.14	Pressure distribution along the nozzle, according to the quasi-monodimensional model. .	13
1.15	Schlieren of the flow patterns corresponding to the condition: (a) shock at exit, (b) over-expanded flow, (c) under-expanded flow.	13
1.16	Sketch of an internal shock structure under Free Shock Separation regime in a TOP nozzle.	15
1.17	Sketch of the wall pressure in a Free Shock Separation.	15
1.18	Sketch of an internal shock structure under Restricted Shock Separation regime in a TOP nozzle.	16
1.19	Sketch of the wall pressure in a Restricted Shock Separation.	17
1.20	Sketch of a Dual-Bell nozzle.	18
1.21	Sketch of the operating modes and flow development inside the Dual-Bell nozzle: (left) sea-level mode, (middle) transition mode and (right) high-altitude mode.	18
1.22	Schematic representation of the separation line unsteady movement in a generic nozzle. .	21
3.1	Minimum distance to nearest wall examples: correct, inaccurate and incorrect computations.	35
3.2	Original concept sketch of Detached Eddy Simulation (DES) from the Spalart presentation of the 1997.	40
3.3	Summary of DES motivations.	40
3.4	Types of grids in boundary layers.	42
3.5	Velocity contour that shows the GIS phenomenon.	42
3.6	Possible situations for DES-type methods.	43
3.7	Vorticity contours in a jet: (a) standard DES and (b) implicit Large-Eddy Simulation (LES), ν_T disabled.	43
3.8	Vorticity magnitude in a jet meridian plane from Spalart-Allmaras Turbulence Model (SA) LES with Δ_{max} and Δ_{SLA}	44

3.9	Wall-Modeled Large-Eddy Simulation (WMLES) of the channel flow results.	45
3.10	Comparison between SA- and SST-based DDES for the reference calibration case.	47
4.1	Notation used for the grid cells. Grid sketch is in the $x - y$ plane. The grid is uniformly extruded in the third dimension.	49
4.2	Two-dimensional schematic representation of the compound volume used to illustrate the discrete conservation property. The grey filled area is $\bigcup V_{i,j,k}$. The thick black solid line is the border $\partial(\bigcup V_{i,j,k})$	50
4.3	Schematic of the face normal convention adopted. Grid sketch is in the $x - y$ plane.	52
4.4	Schematic of the grid cells involved in the evaluation of $\partial\varphi/\partial n$ appearing in the viscous fluxes on face $i + 1/2$	55
5.1	Three-dimensional visualization of the computational domain and mesh for the simulation of the C1xb test case. For clarity, only 1 node every 4 is shown in the mesh.	68
5.2	Contours of (top) mean axial velocity and (bottom) mean Mach number from ILES	71
5.3	Comparison of (left) mean axial velocity and (right) mean radial velocity distribution from ILES (lines) at various stations with the theoretical solution (symbols).	71
5.4	Contours of instantaneous spanwise vorticity in a longitudinal x-y plane for (a) the 3D ILES and (b) the 2D simulation. Blue and red contours represent clockwise and counter-clockwise rotating vortices. Sixty-four levels in the range $-25 < \omega_z T_{\text{ref}} < 25$ ($T_{\text{ref}} = 1.08 \cdot 10^{-3}$ s) are shown.	72
5.5	Visualization of turbulent structures through an iso-surface of the Q criterion. The blue circles denote the position of the experimental pressure probes.	73
5.6	Comparison of the pressure oscillation signals extracted from 2D (red solid lines) and 3D (green solid lines) simulations at representative probes: (a) PC head, (b) PC 1, (c) PC 3 and (d) PC 5.	74
5.7	Distribution of the rms pressure fluctuations for the current 2D and 3D simulations, compared with reference experimental data (circles) and previous 2D computations.	74
5.8	Contours of premultiplied power spectral densities ($f \cdot E_{pp}$) of the wall pressure signals as a function of the axial position and frequency from ILES. Sixteen contour levels are shown in exponential scale between $1.5 \cdot 10^3 \text{ Pa}^2$ and $5 \cdot 10^5 \text{ Pa}^2$	75
5.9	Frequency spectrum of the axial velocity component at several probes in the shear layer from ILES.	76
5.10	Contours of the space-time pressure correlation coefficient at representative probes from ILES: (a) PC 3 probe, (b) PC 4 probe, (c) PC 5 probe, (d) PC 6 probe. Sixteen equally spaced levels are shown between -0.5 and 1.	77
5.11	Contours of the two-point spatial correlation coefficient of the wall pressure at representative probes from ILES: (a) PC 3 probe, (b) PC 4 probe, (c) PC 5 probe, (d) PC 6 probe. Sixteen equally spaced levels are shown between -0.5 and 1.	78
5.12	Distribution of the local convection velocity of the pressure-carrying eddies at several probes.	78
6.1	Schematic of (a) the dual-bell nozzle geometry and (b) a conventional truncated ideal contour (TIC) nozzle.	81
6.2	Schematic of (a) the computational domain and (b) the computational grid adopted for DDES in the x-y plane (only one every 8th grid nodes is shown).	82
6.3	Contours of the averaged Mach number field from DDES. The white dashed line denotes the sonic level.	85
6.4	Visualisation of (a) the instantaneous density-gradient magnitude (numerical Schlieren) in an x-y plane and of (b) turbulent structures through an iso-surface of the Q criterion, coloured with the local value of the longitudinal velocity.	86

6.5	Comparison of the distribution of the normalized mean wall pressure (a) and standard deviation of wall-pressure fluctuations (b) with experimental data.	88
6.6	Comparison between dual-bell and TIC nozzles of the standard deviation of wall-pressure fluctuations. The black solid line refers to the dual-bell nozzle while the red solid one to the TIC.	88
6.7	Dual-bell nozzle: (a) contours of premultiplied power spectral densities $G(f) \cdot f/\sigma^2$ of the wall-pressure as a function of the streamwise location and frequency; (b) axial evolution of the normalized spectra at representative streamwise locations. Eleven contour levels are shown in exponential scale between $5 \cdot 10^{-4}$ and 0.1.	89
6.8	TIC nozzle: (a) contours of premultiplied power spectral densities $G(f) \cdot f/\sigma^2$ of the wall-pressure as a function of the streamwise location and frequency; (b) axial evolution of the normalized spectra at representative streamwise locations. Eleven contour levels are shown in exponential scale between $5 \cdot 10^{-4}$ and 0.1. The circles in (b) denote reference experimental data.	89
6.9	Physical interpretation of the Fourier azimuthal decomposition. Solid black lines refer to the real ($m > 0$) part of the Fourier coefficients, solid grey lines refer to the unit circle.	91
6.10	Normalized eigenspectra of the Fourier modes as fraction of resolved energy per mode at two different axial stations: (a) dual-bell nozzle and (b) TIC nozzle.	91
6.11	Premultiplied spectra of the zeroth (left) and first (right) Fourier azimuthal mode at $x - x_{sep} = 0.16r_t$ (a,b) and $7.03r_t$ (c,d). The black solid line refers to the dual nozzle while the red solid one to the TIC. For visualization purposes, different scales are applied to the various figures	94
6.12	Comparison between dual-bell and TIC nozzles of the time distribution of the side-loads components F_y and F_z (a) and magnitude $ F $ (b). The black symbols and solid line refer to the dual-bell nozzle while the red symbols and solid line to the TIC.	95
6.13	Time history of side-loads direction: (a) Dual-Bell and (b) TIC nozzle.	96
6.14	Comparison between the dual-bell and TIC nozzles of the probability density function of the side-loads components (a,b) and magnitude (c). Black solid lines represent the dual-bell nozzle, the red solid lines represent the TIC nozzle while the black dashed line is the theoretical distribution.	96
6.15	Evolution along the x-axis of the side-loads magnitude averaged in time for (a) the dual-bell and (b) TIC nozzle. For visualization purposes, different scales are applied to the figures	97
6.16	Normalized premultiplied power spectral densities of the side-loads components F_y (a) and F_z (b). The black solid line refers to the DB nozzle while the red solid one to the TIC.	98
6.17	(a) Time history of the thrust coefficient $F_x/(p_0 A_t)$ for the dual-bell and TIC nozzles and (b) corresponding premultiplied power spectral densities. The black solid line denotes the dual-bell nozzle, the red solid line refers to the TIC nozzle.	99
A.1	A visual explanation of the convolution product and the difference between convolution and correlation.	105
B.1	Three substencils for the reconstruction at $x_{j+1/2}$ using three cells in each stencil. . .	109

List of Tables

3.1	Spalart-Allmaras model constants.	35
5.1	Physical values used for the simulation of the ONERA C1xb test case.	68
5.2	Position along the chamber of the experimental/numerical pressure probes (denoted as PC #).	69
6.1	Dual-Bell and TIC nozzles geometrical parameters.	83
6.2	Comparison of the shock motion peak frequencies with the experimental data.	89
6.3	Modes peak frequency, St and St* numbers for Dual-Bell and TIC nozzles.	93
A.1	Fourier pairs of common functions.	105
B.1	Butcher tableau for s -stages Runge-Kutta method.	111

Acronyms

CFD Computational Fluid Dynamics

CFL Courant–Friedrichs–Lowy

CP Constant Pressure

CT Combustion Time

CVS Corner Vortex Shedding

DB Dual Bell

DDES Delayed Detached Eddy Simulation

DES Detached Eddy Simulation

DIT Decaying Isotropic Turbulence

DNS Direct Numerical Simulation

ENO Essentially Non-Oscillatory

FANS Favres Average Navier-Stokes

FD Finite Difference

FSS Free Shock Separation

FV Finite Volume

GIS Grid-Induced Separation

ILES Implicit Large-Eddy Simulation

LES Large-Eddy Simulation

LEVM Linear Eddy Viscosity Models

LLM Logarithmic-Layer Mismatch

MOC Method of Characteristics

MPI Message Passing Interface

MSD Modeled Stress Depletion

NPR Nozzle Pressure Ratio

ODEs Ordinary Differential Equations

OVS Obstacle Vortex Shedding

PDEs Partial Differential Equations

PDF Probability Density Function

PSD Power Spectral Density

PVS Parietal Vortex Shedding

RANS Reynolds Average Navier-Stokes

RSM Reynolds Stress Modeling

RSS Restricted Shock Separation

SA Spalart-Allmaras Turbulence Model

SGS Sub-Grid Scale

SRM Solid Rocket Motor

SST Menter Shear Stress Transport Model

SVS Surface Vortex Shedding

SWBLI Shock-Wave/Boundary-Layer Interaction

TIC Truncated Ideal Contoured

TOC Thrust Optimized Contoured

TOP Thrust Optimized Parabolic

TP Thermal Protection

URANS Unsteady Reynolds Average Navier-Stokes

VLES Very Large-Eddy Simulation

WENO Weighted-Essentially Non Oscillatory

WMLES Wall-Modeled Large-Eddy Simulation

ZDES Zonal Detached Eddy Simulation

Chapter 1

Introduction

This manuscript aims at performing high-fidelity numerical simulations of compressible turbulent flows for the purpose of predicting aeroacoustic resonance phenomena inside internal flows for space applications. In the ascent phase of a space launcher, the internal flow developing inside the solid rocket motor chamber could create strong oscillations that could affect the payload integrity. The same effect could be generated by the development of aerodynamic side-loads due to the Shock-Wave/Turbulent Boundary-Layer Interaction inside rocket nozzle. In both cases, aeroacoustic resonance phenomena could occur inside the system, leading to the generation of forces that could damage the payload and the launcher structure. For these reasons, a correct evaluation of these phenomena is important and should be taken into account in the design phase of these systems.

Several computational aeroacoustic methods have been developed to correctly capture the unsteady phenomena generated by acoustics waves. Far-field aeroacoustics prediction generally exploit the use of methods that deal with sources that must be known a priori. When dealing with the near-field, the full Navier-Stokes equations must be solved by means of numerical simulations. The efforts of the research community in this field is stimulated by the renewed interest in supersonic flights and space vehicles, where the problem of aeroacoustic resonance and pressure oscillations is present during a substantial part of the ascent of the launchers, and represents a key restraint in the design phase. Although the past decade has seen advancement of our understanding of these phenomena, the problem of the pressure oscillations in solid rocket motor chamber and of the side loads in rocket nozzle has appeared to be substantially more complex than previously realized and some key physical mechanisms are still unclear.

Moreover, the experimental analysis of these flows in both transient and stabilized regimes is very difficult and expensive, because it would need flow visualizations and measurements in the few seconds of the engine run (or milliseconds for the crucial part of the transient). Subscale tests, even if less expensive, keep the difficulties of the full-scale experiments. As a result, the unsteady nature of the flow separation is not easily accessible by experiments in real configurations. On the other hand, Computational Fluid Dynamics (CFD) tools, if previously validated through appropriate benchmark calculations for the appropriate case, have the potential for computing unsteady interaction properties and also for exploring the effects of different configurations and flow variations and to investigate the underlying physics.

1.1 Aeroacoustic Feedback Coupling

Hydrodynamic fluctuations can produce acoustic fluctuations, which can trigger hydrodynamic instabilities in turn. These processes are observed in a wide range of physical problems such as the flow inside solid rocket motors, supersonic nozzles, but also in screeching and impinging jets [1], transonic airfoils [2], pipes and cavities [3]. It is clear that, under certain conditions, a resonance condition between the hydrodynamic instabilities and the acoustic modes may be established. As mentioned in the previous section, the focus of the present work is to capture the aeroacoustic resonance in space applications (i.e. SRMs and overexpanded nozzle flows) by means of high-fidelity numerical simulations.

The resonance phenomenon highlighted here is associated with the production of intense and highly directional discrete-frequency sound, and the desire to predict, and try to suppress, these acoustic waves motivates much of the research into aeroacoustic resonance. While many researchers made contributions to the early understanding of these resonance phenomena from a physical point of view, it is inarguable that the most significant advances came through the work of Alan Powell. In the 1950s, Powell made several and essential contributions on two kinds of jet resonance: the edge-tone [4] and the supersonic jet screech [5]. Each of these flows is characterized by a self-sustaining feedback loop, that is the same found in the other cited flow configurations. This feedback loop can be summarized into four key processes:

1. The downstream propagation of energy, typically due to hydrodynamic perturbations, also called the downstream process.
2. A mechanism where the downstream-propagating perturbation energy is converted into an upstream-propagating disturbance. This mechanism is generally responsible for the generation of acoustic tones, also called the generation process.
3. The upstream propagation of these disturbances to a crucial point where the base flow is sensitive to the perturbation, also called the upstream process.
4. The triggering of this sensitive point in the flow by the upstream-propagating perturbation resulting in the production of a new downstream-propagating hydrodynamic disturbance, also called the receptivity process.

Moreover, through his work on both the edge-tone and screech, Powell identified two criteria that must be met for the feedback loop to sustain itself: i) the phase criterion and ii) the amplitude criterion. According to the former, the frequency of the resonance must be selected such that the feedback loop becomes self-reinforcing. According to the second criterion Powell established that for a feedback loop to be sustained, the gain associated with each of the four processes of the feedback must be enough to guarantee that the amplitude of each new disturbance matches the amplitude of the previous one. Powell expressed this amplitude/gain criterion as:

$$q_d \eta_g \eta_u \eta_r \geq 1 \quad (1.1)$$

where q_d is the gain associated with the downstream process, η_g is the efficiency of the conversion of downstream-propagating energy into upstream-propagating energy, η_u is a transmission efficiency for the upstream-propagating disturbances, and η_r is the efficiency of the receptivity process. The four processes are shown diagrammatically in Fig.1.1.

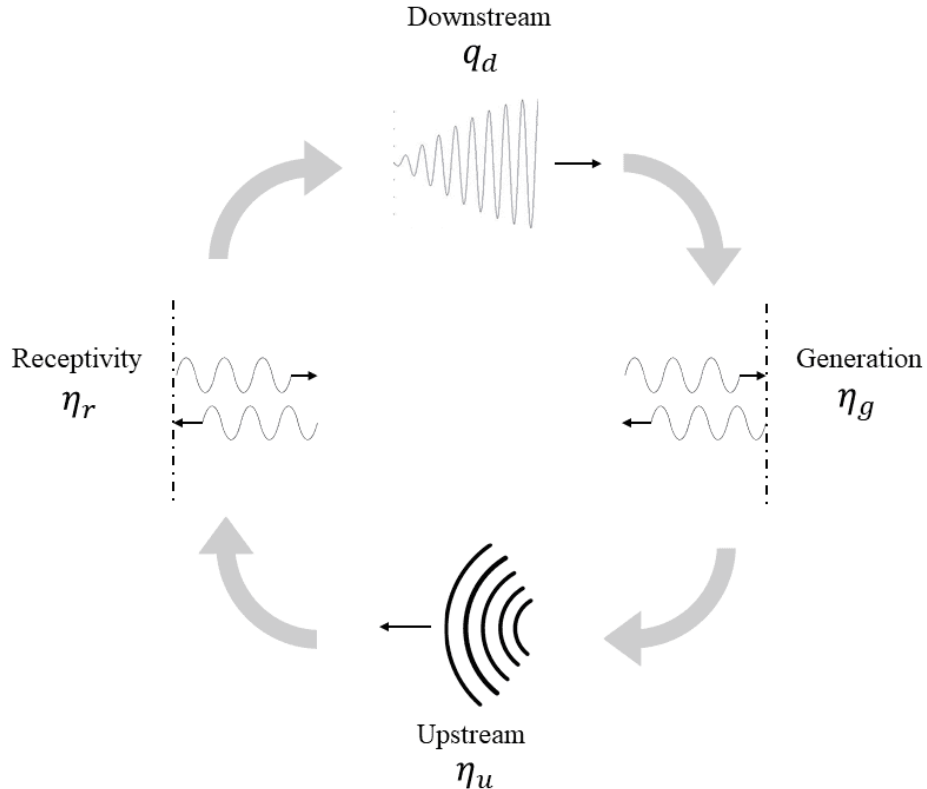


Figure 1.1: Sketch of the four processes of the aeroacoustic feedback resonance loop.

1.2 Solid Rocket Motor Flow

Solid Rocket Motors (SRMs) are chemical thermal rockets, where the enthalpic energy is converted to kinetic energy by a thermodynamic transformation. The thermal energy is obtained by the exothermic reactions characterizing the combustion processes of rocket propellants; the thermal energy is then transformed into kinetic energy by a propulsive nozzle. In a Solid Rocket Motor, the oxidizer and the combustive agent are mixed together in a single “propellant solid grain”. This propellant grain cannot burn itself, rather it has to be ignited by an external source of energy, i.e. the igniter hot jets. As shown in Fig. 1.2, a rocket consists of a chamber, a throat and a nozzle. The rocket generates thrust by accelerating a high-pressure gas to supersonic velocities in a converging-diverging nozzle. The high-pressure gas is generated by high-temperature decomposition of propellants (regression). The application of the momentum conservation leads to look for the highest exhaust velocity. In fact, rocket thrust is generated by momentum exchange between the exhaust and the vehicle and by the pressure imbalance at the nozzle exit (Brown [6]) as:

$$T = \dot{m}u_e + (p_e - p_a)A_e \quad (1.2)$$

where \dot{m} is the exhaust gas mass flow rate, u_e is the jet velocity at the nozzle exit plane, p_e is the static pressure at the nozzle exit plane, p_a is the ambient pressure and A_e is the flow area at the nozzle exit plane.

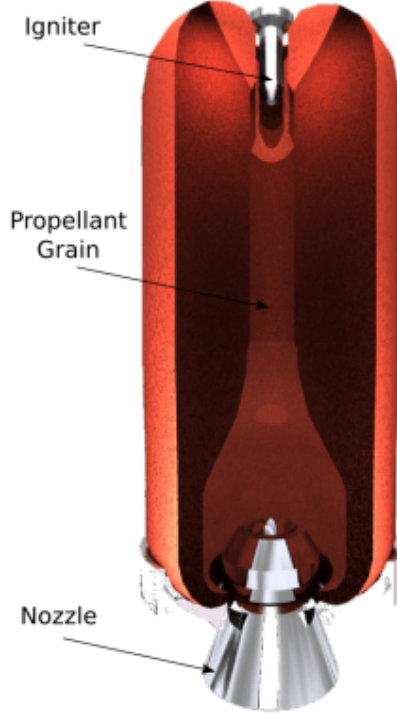


Figure 1.2: Sketch of a generic Solid Rocket Motor.[7]

As already mentioned, SRMs produce energy through high-temperature gases at the grain surface. The surface regresses normal to itself in parallel layers (see Sec. 1.2). The rate of regression is called burning rate (r_0). The mass flow rate of the hot gases leaving the grain surface is proportional to the product of the instantaneous area burning (A_g), the grain density (ρ_g) and the burning rate as:

$$\dot{m}_{in} = A_g \rho_g r_0 \quad (1.3)$$

with,

$$r_0 = a p_c^n \quad (1.4)$$

where a and n are constant that are dependant from the grain composition, and p_c is the combustion chamber pressure. The index n is called combustion index. A sketch of the grain regression is depicted in Fig. 1.3. It is worth to notice that, the combustion is stable only if $n < 1$, due to the equilibrium of the inlet and outlet mass flow rate ($\dot{m}_{in} = \dot{m}_{out}$).

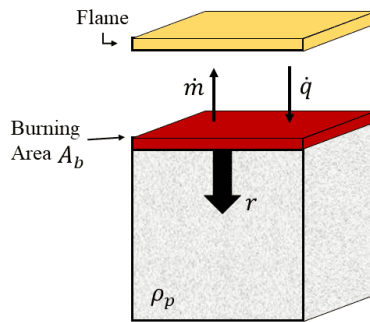


Figure 1.3: Schematic of SRMs surface grain combustion physical process.

Propellant grains

In a solid rocket motor, the propellant tank and the combustion chamber are the same vessel. The viscous propellant mixture is cast and cured in a mold to achieve the desired shape and structural strength. After casting, the propellant is referred to as the grain. The most frequent method of casting is done in-place in the motor case using a mandrel to form the central port (i.e. case-bonded grains). Grains may also be cast separately and loaded into the case at a later time (i.e. cartridge-loaded grains). Large grains are cast in segments, which are then stacked to form a motor. Segmented grains solve the difficult motor transport problem, but require also high temperature case joints (i.e. the inhibitors), which can be a serious source of pressure oscillation and vortex shedding (see Sec. 1.2.2). One case joint was the cause of the Challenger explosion [6].

Grain shape, primarily cross section, determines the surface burning area as a function of time. Burning area, along with burning rate, determines thrust (see eq. 1.2). For a given propellant, the time evolution of the surface area determines the shape of the thrust-time curve. A cylindrical grain inhibited on the end sides (called “cigarette burner” or “end burner”) has a constant burning area and therefore a constant thrust. A grain with an essentially constant burning surface area and thrust-time curve is called neutral burning. A grain that has an increasing burning surface area with time is called progressive. A case-bonded grain with a cylindrical port would be a progressive burning grain (see Fig. 1.4 (1)). A grain that has a decreasing burning surface area with time is called regressive. An example is provided in Fig. 1.4 (3), while other grain cross sections are shown in Fig. 1.4. Neutral burning is the most common design for spacecraft. A star grain is the most commonly used shape and is nearly neutral. The progression of the burning surface in a star grain is as shown in Fig. 1.5.

SRM Internal Ballistics

The SRM internal ballistics studies the internal flowfield development inside a solid propellant rocket motor during all its operative phases, from motor start-up to burn-out. This study completely characterize and define the motor behaviour, its performance and its mission capabilities. Given an overall Combustion Time (CT) of the SRM, it is possible to distinguish three main different phases, each characterized by different physical phenomena.

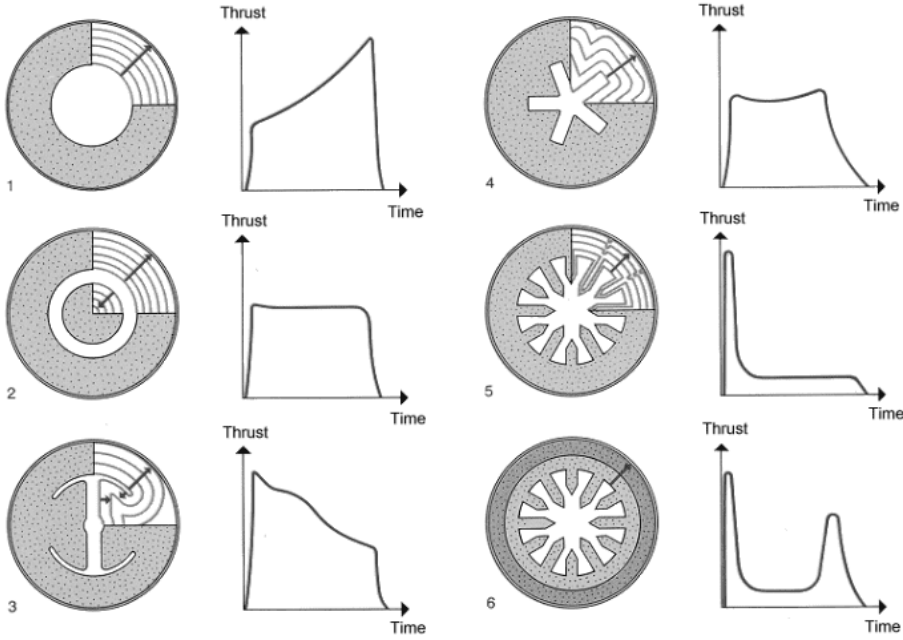


Figure 1.4: Radial grain configurations and thrust curves in time. [8]

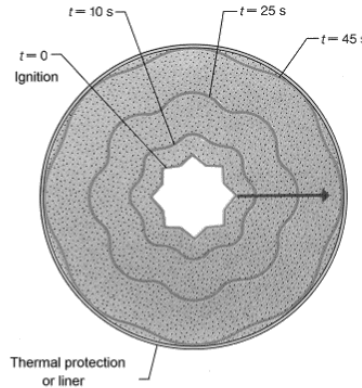


Figure 1.5: Schematic of SMRs surface grain progression. [8]

1. **Ignition Transient.** The impingement of the igniter jets on the grain surface causes the grain propellant ignition, with possible acoustic mode excitement due to the interaction between the jets and the chamber geometry. After this, the flame triggers the ignition of the entire grain propellant surface, causing an increasing mass inlet flux and chamber pressure. In this phase, a pressure overpeak due to the erosive contribution (related to igniter gases high tangential velocities respect to the grain surface) to the burning rate [9], enhances the combustion process mechanism. When the burning surface is completely ignited, a *quasi steady state* condition in the SRM chamber is achieved.
2. **Quasi Steady State.** In this operative phase, the internal SRM ballistics is mainly driven by the grain mass addition and the propellant surface regression due to combustion. Ablation phenomena also occur in the inner parts of the chamber, which get uncovered during the grain regression and, consequently, exposed to the chamber hot gases. In fact, the SRM metallic or composite casing structure is completely covered inwards by ablative materials,

acting as passive thermal control system (see Sec. 1.2). In this phase, the SRM could suffer acoustics instability phenomena, which can cause low-level, but sustained, pressure and thrust oscillations [10] in the chamber, due to the shear layer instability and the related vortex shedding. These phenomena arise as an acoustic longitudinal mode excitation (see Sec. 1.2.2), driven by the coupling with the developed hydrodynamic instability.

3. **Tail Off.** As the grain burning surface recedes in time, parts of the liner and the case Thermal Protections (TPs) get exposed to the chamber hot gases and start to add ablation products inside the chamber itself. Moreover, as the grain combustion products becomes smaller, a rapid and sudden decrease of the chamber pressure occurs, with possible combustion fluctuations generation. Hence, the tail-off phase is characterized by unsteady features that are related to the chamber pressure decrease in time, mixing of gases coming from the residual grain propellant combustion and case thermal protections ablation.

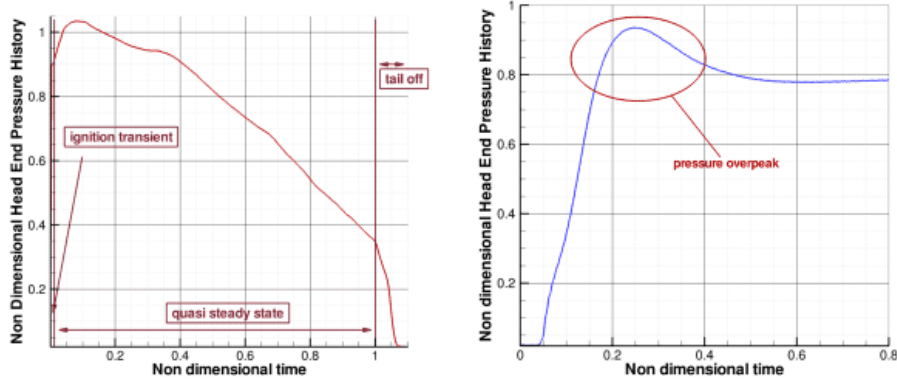


Figure 1.6: Head-end pressure of a generic SRM: (left) whole operative life and (right) ignition transient. [7]

1.2.1 Taylor Flow

In all the types of SRMs, the hot burnt gas flow originates radially from the burning surface of the combustion chamber and develops longitudinally before reaching the exhaust nozzle. When injected radially, the gases lead to the so-called Taylor flow [11–13]. The flow is induced by wall injection in an axisymmetric channel of diameter D without inhibitor and without nozzle, as sketched in Fig. 1.7. The channel is limited upstream by a nonporous wall, called the forward end or head end. At the porous cylinder the injection velocity U_i is supposed to be perpendicular to the wall, uniform and constant. The cylindrical coordinates are (x, r, θ) , where x is aligned with the channel axis and originates at the forward end ($x = 0$). The corresponding velocities are (U_x, U_r, U_θ) .

The flow is considered incompressible, single phase and nonreactive. The gravity is neglected. The governing equations are the Navier–Stokes equations (see Chapter 2), which are expressed in cylindrical coordinates. As result, the flow is axisymmetric, so that $U_\theta = 0$ and $\left(\frac{\partial}{\partial \theta}\right) = 0$. The Navier-Stokes equations are made non-dimensional by using the injection length L_i , the radius $D/2$, and the injection velocity U_i . For this problem, Taylor [11] obtained an analytical solution of the Euler equation (see also Dunlap et al. [12], Griffond et al. [13]) expressed as:

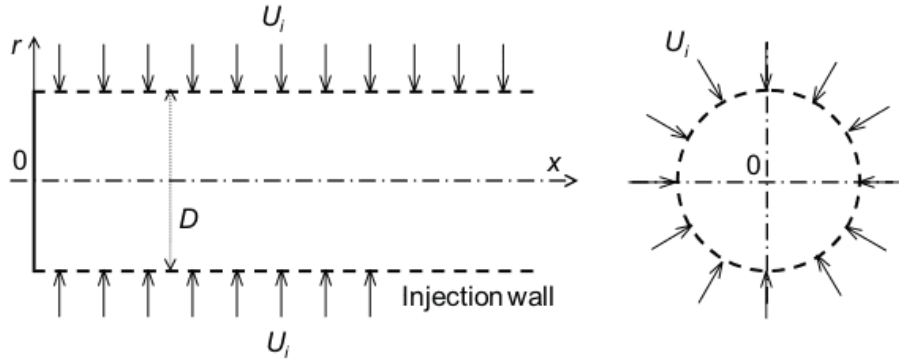


Figure 1.7: Schematic of the theoretical problem of the Taylor flow. [8]

$$\bar{U}_x = \pi \bar{x} \cos\left(\frac{\pi}{2} \bar{r}^2\right) \quad (1.5)$$

$$\bar{U}_r = -\frac{1}{\bar{r}} \sin\left(\frac{\pi}{2} \bar{r}^2\right) \quad (1.6)$$

In dimensional form, the Taylor flow is described by:

$$U_x = \pi |U_i| \frac{2x}{D} \cos\left(2\pi \frac{r^2}{D^2}\right) \quad (1.7)$$

$$U_r = -U_i \frac{D}{2r} \sin\left(2\pi \frac{r^2}{D^2}\right) \quad (1.8)$$

A straightforward calculation shows that the Taylor solution is a good approximation of the viscous flow for injection Reynolds numbers greater than 1000 [13]. Fig.1.8 provides an example of the streamlines and axial velocity magnitude of the Taylor flow [8]. The x-axis represents the axial position extended from the head-end to the exit of a porous cylinder. The r-axis gives the radial position starting from the symmetry axis and ending at the porous cylinder. The evolution of the mean velocity on the axis is linear. Moreover, because of the superposition of the radial injection along the axial distance, the velocity magnitude is increasing from the wall to the symmetry axis.

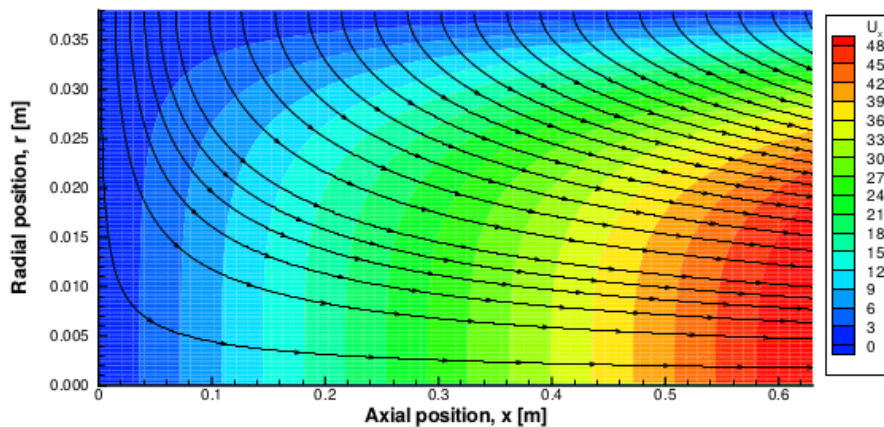


Figure 1.8: Representation in the x-r plane of the streamlines and axial velocity magnitude of the Taylor flow. [8]

1.2.2 Hydrodynamic Instabilities and Vortex Shedding

As already mentioned in Sec. 1.2, the internal ballistics of SRMs is characterized by complex physical phenomena, involving the interaction of the shear layers that develop in different parts of the motor and the acoustic field of the combustion chamber. The possible coupling between the hydrodynamic instabilities and the acoustic resonant modes can trigger pressure and thrust oscillations, which can damage the motor structures, the thrust vector control system, and the payload comfort.

Three different vortex shedding phenomena have been identified to be responsible of pressure oscillations in SRMs by Fabignon et al. [14]:

- Corner Vortex Shedding (CVS)
- Obstacle Vortex Shedding (OVS)
- Surface/Parietal Vortex Shedding (SVS or PVS)

In the corner vortex shedding, the vortices develop in the shear layer from a backward facing step, or chamfered edge (see Fig. 1.9). This backward step can be the end of a propellant grain. Behind the step, the flow injection is absent. In these conditions, the mean flow downstream the shedding point can be considered as parallel. The vortices travel at constant speed between the shedding point and the nozzle. This configuration is the most simple and was mainly investigated in the past [15–17]. It is commonly used to validate physical models introduced in computational codes.

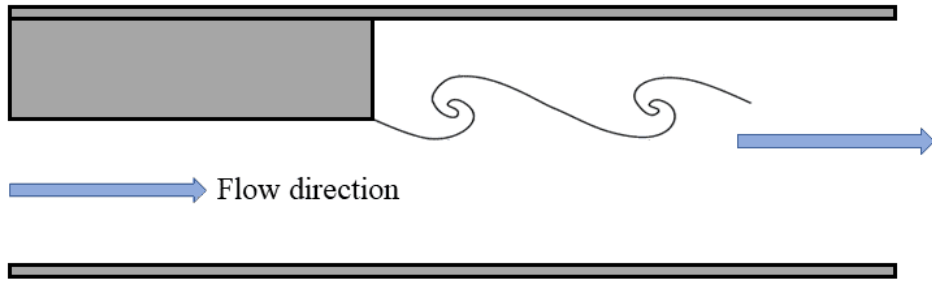


Figure 1.9: Schematic of the corner vortex shedding.

In the obstacle vortex shedding, a shear layer is generated at the thermal protection (TP) protruding into the flow (see Sec. 1.2). If the shear layer is unstable, vortices develop behind the thermal protection, as clearly visible in Fig. 1.10. The analysis is complex because the inhibitor could be followed by another propellant grain with side mass injection (segmented SRMs). The vortices are accelerated downstream the shedding point due to this additional mass flow injection.

In the surface or parietal vortex shedding, vortices are not generated by a shear layer. The shedding point is not clearly located and the vortices develop from a natural instability of the flow itself (see Fig. 1.11). Griffond et al. [13] developed a local linear spatial theory to investigate the stability of incompressible pipe flows resulting from wall injection. They showed that the flow is highly non-parallel and the radial injection promotes non negligible variation of the transverse velocity component. The flow instability originates coherent structures downstream the critical axial

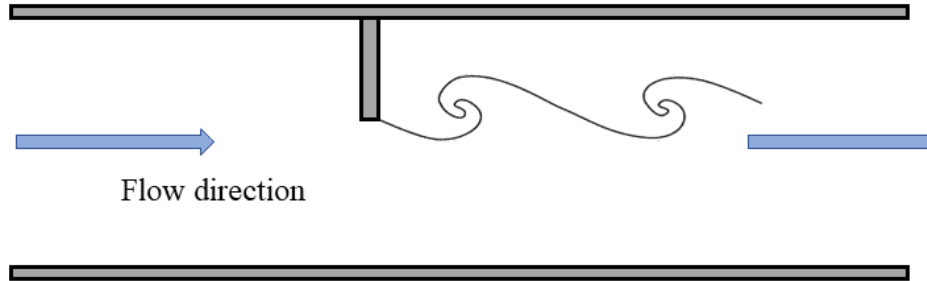


Figure 1.10: Schematic of the obstacle vortex shedding.

position.

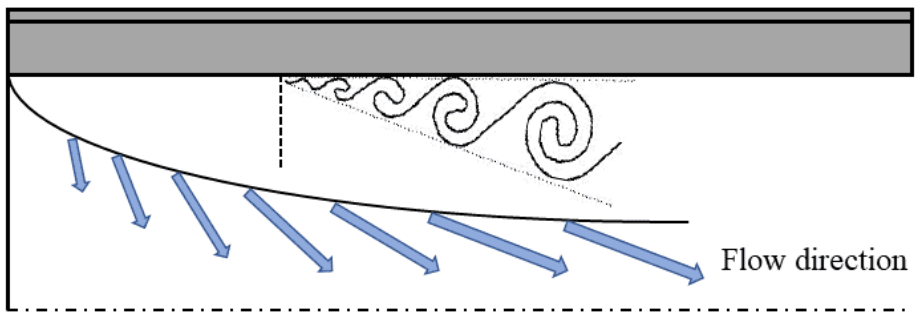


Figure 1.11: Schematic of the parietal vortex shedding.

Flandro and Jacobs [18] were the first authors to suggest the risk of excitation of the acoustic modes of the chamber due to the shear-induced hydrodynamic instabilities of the mean flow. Since then, considerable research effort was concentrated to understand the physical mechanisms leading to the coupling, mainly in connection with the development of large segmented solid-propellant boosters for space-launcher applications [10, 19–21] (e.g. the US Space Shuttle and the European Ariane SLS 5 segments booster). Even though classical stability methods predict stable conditions for these motors, all of them experienced low-level but sustained thrust oscillations during the firing. The low-frequency range of this unsteadiness is of great concern due to the possible coupling with the launcher structural modes, and for the payload comfort, especially when occurring in an advanced phase into the firing.

ONERA C1/C1xb SRMs

Given the intrinsic limitation of simplified methods to predict instabilities in SRMs [22], several studies have been carried out in the last decades to characterize the flow behavior in the chamber [23–26] and to assess the capability of full numerical simulations to predict vortex shedding and pressure oscillations in SRMs [27]. For the purpose of validation and development of adequate numerical models, specific hot-flow experiments were designed in particular at ONERA to develop a sustained vortex shedding [28], both in planar (“C1”) and axisymmetric (“C1xb”, “C1experimental”) configurations. This target was achieved by placing the chamfered propellant edge in the middle of the chamber, a location corresponding to a node of the acoustic pressure field and to an acoustic velocity antinode [29, 30], in order to maximize the acoustic feedback for the even acoustic longi-

tudinal modes. A sketch of the ONERA C1xb is represented in Fig. 1.12. Many 2D simulations of both the C1 and C1xb configurations have been performed in the past for various burning times, with the main aim of investigating the vortex shedding phenomenon and predicting the level of pressure oscillations [16, 31–33]. As a general result, the simulations were able to qualitatively capture the corner vortex shedding behavior in the combustion chamber, and a good agreement with the experimental data was found in the prediction of the peak frequency of pressure oscillations, particularly for grain configurations in the second half of the burning time. However, it was noticed by Lupoglazoff and Vuillot [17] that, at times close to ignition, the level of pressure oscillations in the computation was remarkably higher than the experimental one, a result then confirmed by the 2D simulations of Kourta [31] and French et al. [34]. Moreover, the frequency pressure spectra at the motor aft-end obtained by the computations displayed the occurrence of distinct resonant tones not observed in the experimental spectra, characterized by a more broadband shape. It was speculated [17] that a possible cause of the observed discrepancies could be the transition to small-scale, fine turbulence of the vortices shed by the grain edge, due to the high-shear levels that characterize the initial part of the burn. In fact, the spreading of energy over a wide range of turbulent scales is expected to reduce the coherence of the vortices responsible of the acoustic feedback loop, thus modifying the coupling between vortical structures and chamber acoustic, and in turn, the pressure signals measured at the motor head-end. The role played by turbulence in the combustion chamber and its influence on the coupling between the vortex shedding and pressure oscillations is still an open issue to be clarified. In addition, it also represents a challenging task from the numerical point of view, which inherently requires the use of large-scale, high-fidelity 3D simulations to capture the energy cascade process and the development of small-scale turbulent structures.

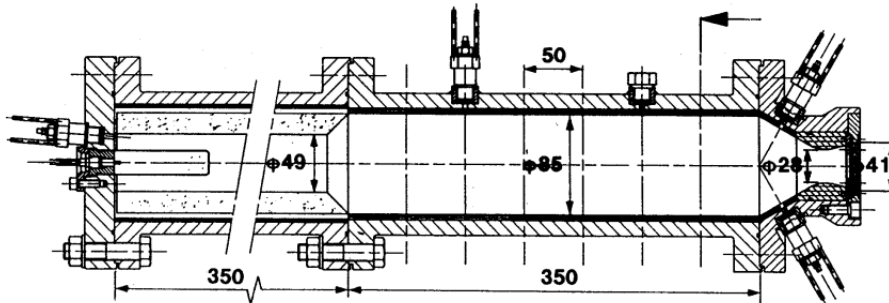


Figure 1.12: Schematic of the experimental setup for the ONERA C1xb SRM [15].

1.3 Nozzle Flow

The nozzle is an essential part of space launchers and more specifically of rocket motors. A jet exhaust produces a net thrust from the energy obtained from combusting fuel by accelerating the fluid flow. Rocket motors maximise thrust and exhaust velocity by using convergent-divergent nozzles with very large area ratios and therefore extremely high pressure ratios. A general nozzle flow can be studied, on first approximation [35], under the assumption of isentropic and stationary flow, of ideal gas and considering a duct with only a slow variation of area in axial direction (de Laval nozzle). Under these hypotheses, the quasi-one-dimensional flow equations can be derived, leading to

$$\frac{dA}{A} = (M^2 - 1) \frac{du}{u} \quad (1.9)$$

For a compressible isentropic flow in a duct, if the Mach number M is lower than one, an increase in the cross section area A results in a decrease of the velocity u , whereas, if the Mach number M is greater than one, an increase in the cross section area causes an increase of the velocity.

Fig. 1.13 shows a schematic of a general convergent-divergent nozzle. The flow is driven through the nozzle by the difference between the inlet total pressure, p_0 , and the external ambient pressure, p_a . The fluid enters the convergent section, generally at a very high total pressure p_0 and at low subsonic velocities. The decrease in the cross section area results in an acceleration of the flow until it reaches sonic conditions $M = 1$ at the nozzle throat. Then, an increase in the cross section area results in an acceleration of the flow to supersonic velocities in the divergent part.

The ratio between the inlet total pressure and the external ambient pressure p_0/p_a is called Nozzle Pressure Ratio (NPR).

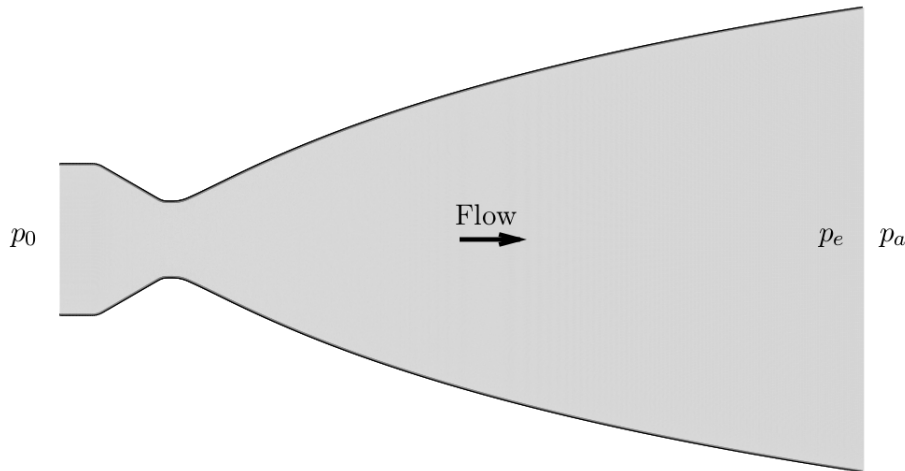


Figure 1.13: Sketch of a nozzle.

It is clear that the proposed model is really simplistic and it is not adequate to understand the complex physical phenomena that involve also the effects of boundary layer, turbulence and strong unsteadiness. However, it represents the simplest approach to the nozzle problem, useful to give a first idea of nozzle flows.

Fig. 1.14 shows the development of the flow properties along the axis of a supersonic nozzle. Depending on the Nozzle Pressure Ratio (NPR), different flow configurations can be observed. Points

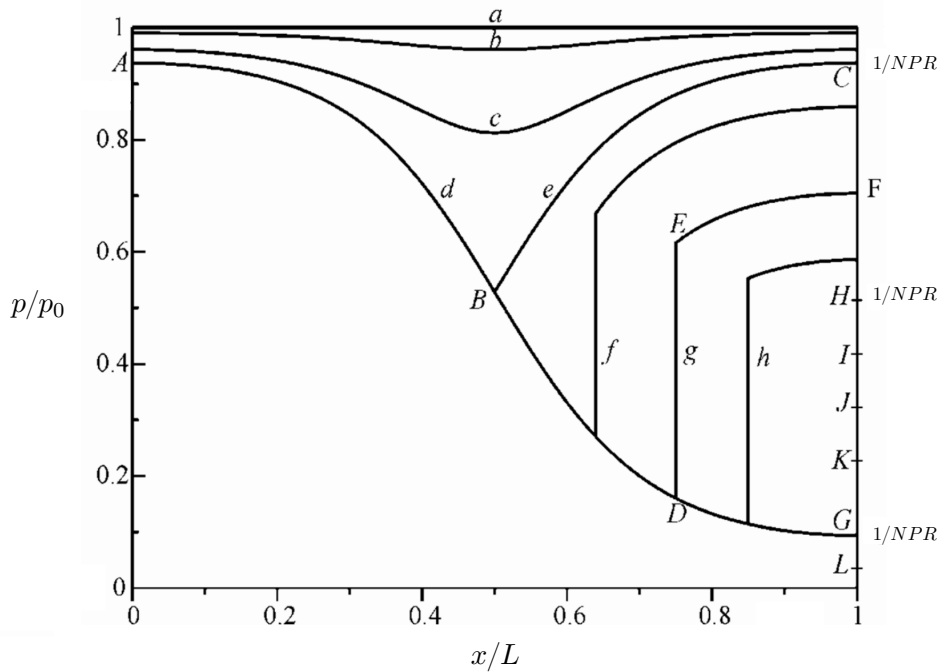


Figure 1.14: Pressure distribution along the nozzle, according to the quasi-monodimensional model.

C, H and G correspond to the three critical pressure ratio.

If the pressure at the exit section of the nozzle is equal to the ambient pressure (curve d, project conditions), the nozzle is said to be *adapted*. For pressure ratios higher than the pressure ratio corresponding to the point C, the flow is completely subsonic throughout the nozzle (curves a, b and c). In the other cases, shocks or expansion waves are responsible for adapting the pressure at the exit of the nozzle to the ambient pressure. In the proper-defined over-expanded interval of pressure ratios (from point C to point H), the pressure at the exit is higher than the ambient pressure and a shock system takes place outside of the nozzle, whereas in under-expanded condition (under point H) the pressure at the exit is lower than the ambient pressure and expansion waves are present at the end. Fig. 1.15 shows the flow patterns corresponding to the described condition.

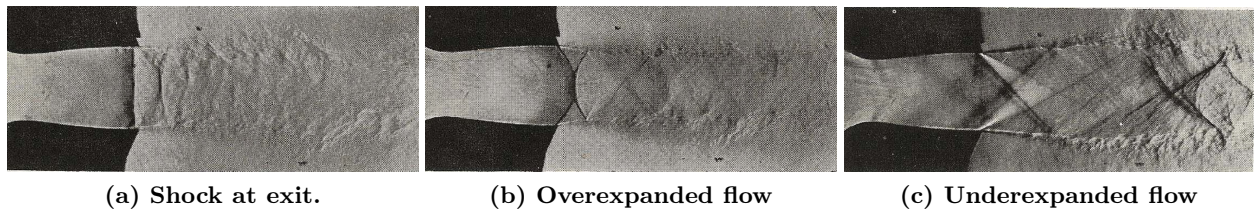


Figure 1.15: Schlieren of the flow patterns corresponding to the condition: (a) shock at exit, (b) over-expanded flow, (c) under-expanded flow. [36]

A flow exposed to an adverse pressure gradient of sufficient strength can cause the boundary layer to separate from the wall, i.e. over-expanded nozzle. When the pressure ratio p_e/p_a is slightly reduced below 1, an oblique shock system arise from the trailing edge of the nozzle wall due to

the induced adverse pressure gradient. When the pressure ratio p_e/p_a is further reduced, to about $0.4 \div 0.8$, the viscous layer cannot sustain the adverse gradient imposed upon it by the inviscid flow, and the boundary layer separates from the wall. This is the case when a rocket engine designed for altitude operation is tested at sea level, but it also occurs during start transients, shut-off transients, or engine throttling modes. In this context, several research [37–41] found that two different separation patterns could occur:

- Free Shock Separation (FSS)
- Restricted Shock Separation (RSS)

Figs. 1.16 and 1.18 show a schematic of the two separation patterns together with the definition of their characteristic points. The occurrence of a specific pattern is mainly determined by the geometry and the nozzle pressure ratio (NPR).

In the Free Shock Separation case, the over-expanded nozzle flow fully separates from the wall and never reattaches. The resulting streamwise wall pressure evolution is mainly governed by the physics of Shock-Wave/Boundary-Layer Interactions (SWBLI) occurring in any supersonic flow separation. However, in contrast to obstacle-induced separation, the separation location is not fixed by the geometrical properties of the test configuration, rather it results mainly from the degree of over-expansion. As the degree of over-expansion is reduced (i.e. NPR is increased toward one) the separation shock moves out of the nozzle. Based on the static wall pressure distribution, the flow can be divided into three regions, as sketched in Fig. 1.17. Upstream of the point of minimum static wall pressure (usually indexed i), the boundary layer is attached and its behavior is similar to that of a full-flowing nozzle. The following region of steep pressure rise, which is ended as soon as a certain plateau (often indexed p) is reached, is usually referred to as separation zone. In the following, we will also refer to it as the interaction or the intermittent region. In this region, the whole separation process, i.e., thickening of boundary layer and actual separation (here indexed s) at the zero wall friction point ($\tau_w = 0$), takes place. The last portion of the nozzle, where the flow is fully separated and which is referred to as the recirculation zone, shows a weak pressure increase until a wall pressure slightly below the ambient pressure p_a is reached at the nozzle exit. This gradual pressure rise from p_p to p_e is due to the inflow and upstream acceleration of gas from the ambient into the recirculating region. In fact, in the recirculating region caused by separation, the external fluid is sucked into a subsonic region, at the origin of an oblique shock wave near the wall (separation shock). The separation shock interacts with the Mach disk at the triple point, where a reflection shock arises. The annular supersonic plume is limited by two mixing layer, an internal and external one.

In over-expanded operating regimes, which only occur at certain pressure ratios, the pressure downstream of the separation point can exhibit an irregular behavior and can partially reach values above the ambient pressure. This is due to a reattachment of the separated flow to the nozzle wall, inducing a pattern of alternating shocks and expansion waves along the wall. Due to the short separated region, this flow regime is called Restricted Shock Separation. The separation shock and the strong reflected shock interact and two reflected shock waves are generated through a regular interaction from a quadruple point. The cap-shock is the structure composed of separation shock,

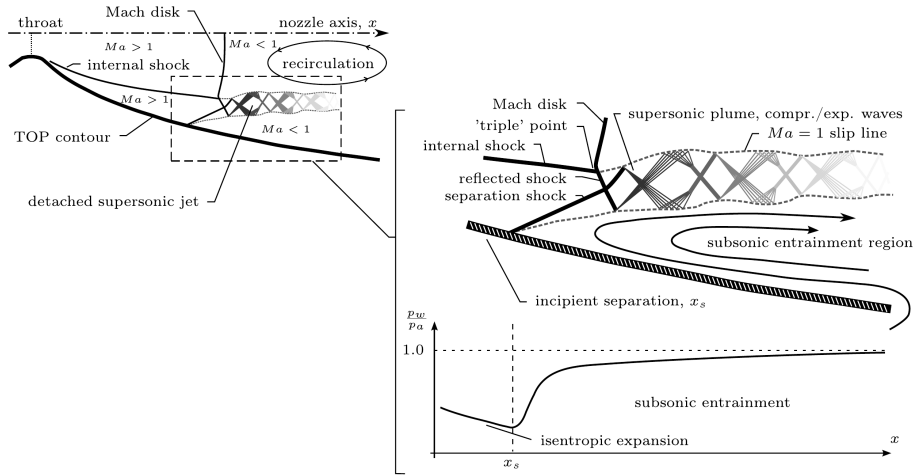


Figure 1.16: Sketch of an internal shock structure under Free Shock Separation regime in a TOP nozzle. [42]

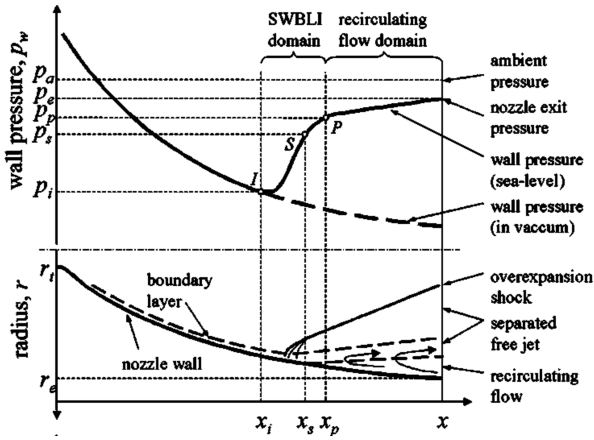


Figure 1.17: Sketch of the wall pressure in a Free Shock Separation. [41]

strong reflected shock and the Mach disk/stem. The separation and reattachment on the wall can happen more than one time.

The existence of two distinct separation processes, the Free Shock Separation, in which the boundary layer separates from the nozzle wall and never reattaches, and the Restricted Shock Separation, characterized by a closed recirculation bubble downstream of the separation point with reattachment on the wall, has been experimentally demonstrated by Nave and Coffey [37], Schmucker [43, 44], Nguyen et al. [45], Hagemann et al. [40] and Östlund [41] on either subscale or full-scale optimized nozzles and numerically by Chen et al. [38], Gross and Weiland [46], Deck and Nguyen [47], Nasuti and Onofri [39] and Moríñigo and Salvá [48].

1.3.1 Nozzle Configurations

The performance of liquid rocket engines for space launchers is highly dependent on the fluid dynamic behaviour of the expansion nozzle and, large values of the ratio between the exit and throat areas are desirable for optimisation purposes. The maximum limit to this ratio is imposed by the need to avoid internal flow separation, since at sea level the flow is highly overexpanded. However, during the start-up phase the chamber pressure is below the design pressure and the flow separates

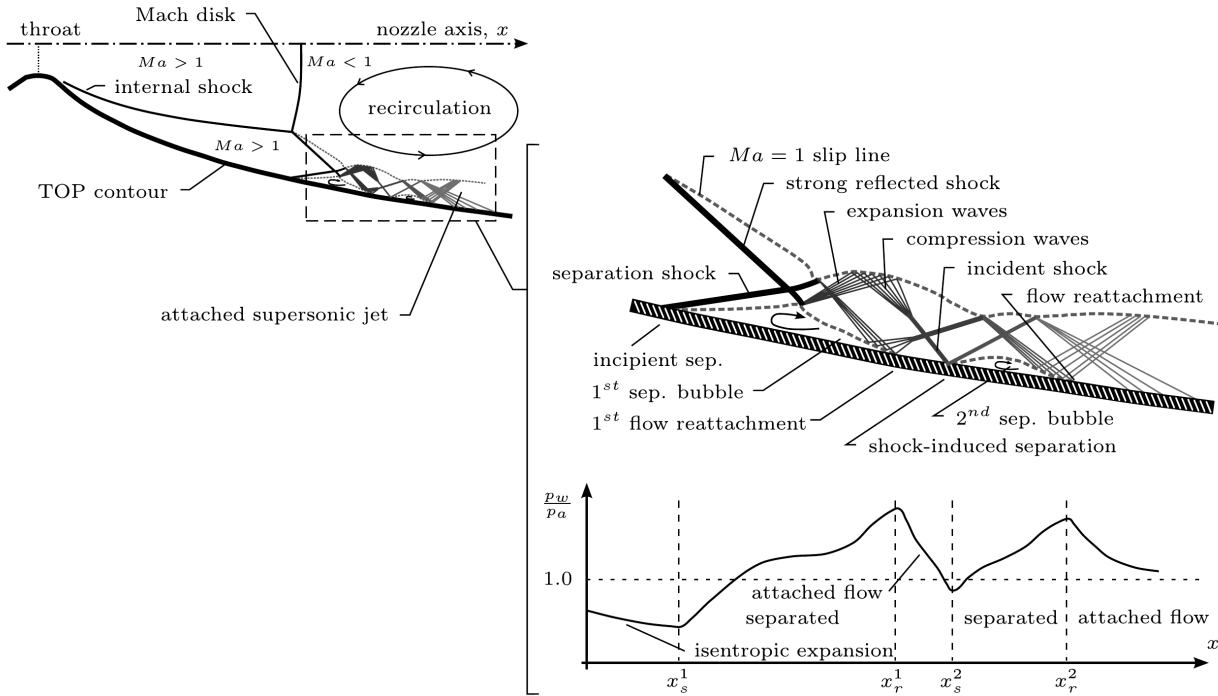


Figure 1.18: Sketch of an internal shock structure under Restricted Shock Separation regime in a TOP nozzle. [42]

from the nozzle wall. This condition is characterized by complex physical features, including the formation of a shock-wave system that adapts the exhaust flow to the higher ambient pressure, Shock-Wave/Boundary-Layer Interactions, and a turbulent recirculating zone with a fluctuating pressure field. As a global effect, the nozzle experiences non-axial forces, known as side-loads, which can be of sufficient strength to cause structural damage to the engine. These side loads are generated by a variety of physical mechanisms, depending on nozzle contour type, mechanical structure, and ambient conditions [49].

With the method of characteristics (MOC) an ideal nozzle contour can be designed, providing an isentropic and shock-free supersonic gas expansion with a uniform exit velocity profile. However, these nozzles are extremely long and consequently heavy and difficult to install [50]. Thus, they are usually shorted to reduce weight without suffering significant thrust losses and giving low side-load levels compared to other configurations. The obtained contours are called Truncated Ideal Contoured (TIC) nozzles. Nowadays, TIC nozzles are mainly considered for research purposes and, although they have been already mounted on rocket engines in the past, they remain a potential choice for the future.

With the same methodology (MOC) and on the basis of a previously developed theory by Guderley and Hantsch [51], Rao [52] derived a nozzle contour for optimal thrust, the Thrust Optimized Contoured (TOC) nozzle, that significantly increased geometrical efficiency compared to a 15° half angle conical nozzle with the same expansion ratio. Nevertheless, the contour that is commonly used on rocket engines was proposed later by Rao [53]. He proposed a skewed parabolic approximation to TOC nozzles, the Thrust Optimized Parabolic (TOP) nozzle, that due to a discontinuity formed at the intersection between the circular arc at the throat and the parabolic curve that defines

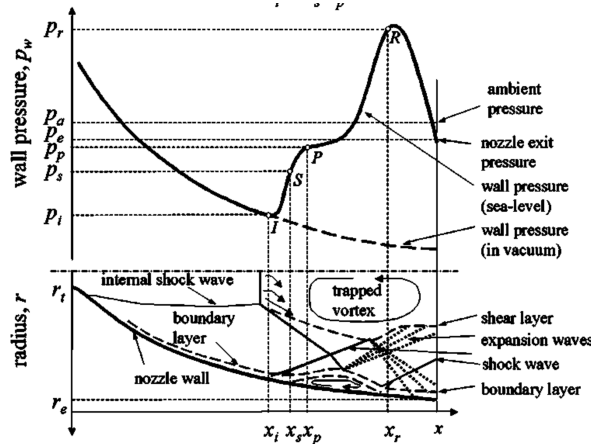


Figure 1.19: Sketch of the wall pressure in a Restricted Shock Separation. [41]

the rest of the divergent section, produces weak compression waves along the wall which coalesce into an internal shock wave further away from the wall. The resulting increase in wall pressure, makes the TOP contour more resistant to flow separation [50]. TOC and TOP nozzles display both FSS and RSS depending on the nozzle pressure ratio, whereas the separation in TIC nozzles occurs only with a shear layer that never reattach to the wall (as FSS). TIC and TOP nozzles are currently subject of intense research with the aim of elucidating the dynamic side loads phenomenon.

As mentioned, for optimisation purposes, large values of the ratio between the exit and throat areas are desirable. However, space launchers operate from sea level to near-vacuum condition during their ascent phase, and as the atmospheric pressure decreases, the adaptation of the exhaust flow is reached at only one altitude. Extendible nozzles with variable area ratio have been conceived [54, 55]. However, the complex mechanical mechanism used to change the exit area and the additional weight introduced lead to a series of disadvantages. In this scenario, altitude compensating nozzle concepts would be more appropriate candidates as for a cryogenic main engine of upper stage space launchers.

The Dual Bell Nozzle

The Dual-Bell (DB) nozzle is a kind of one-step altitude compensating nozzle that may represent a possible alternative to replace conventional bell nozzles in future launcher upper-stage engines. The main feature of this advanced concept is the particular shape of the divergent section, composed by two bells, namely the base and the extension, separated by an inflection point, as shown in Fig. 1.20. It has two main operating conditions:

- **Sea-Level Mode:** in this mode, the DB operates with a low area ratio, with a controlled and symmetrical flow separation at the inflection point, thus avoiding the onset of dangerous side loads than can induce structural damages to the engine. A representation of this working mode is depicted in Fig. 1.21 (a).
- **High-Altitude Mode:** in this mode, the flow attaches to the extension and the nozzle works with a higher area ratio, thus increasing the thrust coefficient. A representation of this working mode is shown in Fig. 1.21 (c).

The parameter governing the transition between the two operating modes is the NPR. In the transition between these two modes the separation front moves into the wall inflection region [56], located immediately downstream the inflection point and characterized by a negative wall-pressure gradient (due to viscosity) like conventional nozzles. As a consequence, the dual-bell can experience non-axial forces [57] before the full transition takes place.¹ The length of the inflection region is of the order of one throat radius and as shown by Martelli et al. [57] it depends on multiple factors, including the boundary-layer thickness at the end of the base, the Prandtl-Meyer expansion fan at the inflection point and the design wall-pressure gradient imposed to the extension during its construction with the method of characteristics [56]. Génin and Stark [58] confirmed experimentally the existence of the inflection region and that during the transition of the separation point in this zone the level of the side loads is similar to that suffered by a conventional nozzle. A representation of the transition mode is represented in Fig. 1.21 (b).

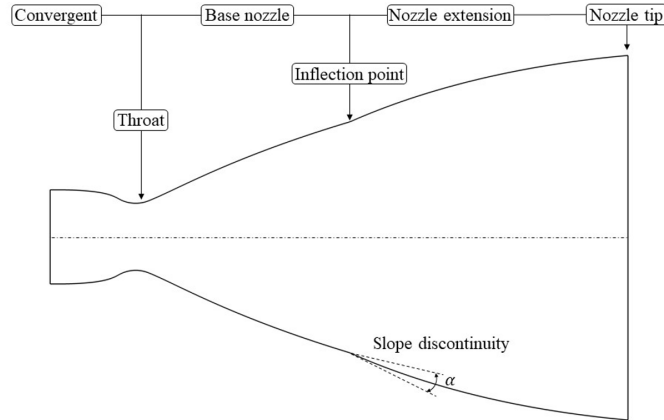


Figure 1.20: Sketch of a Dual-Bell nozzle.

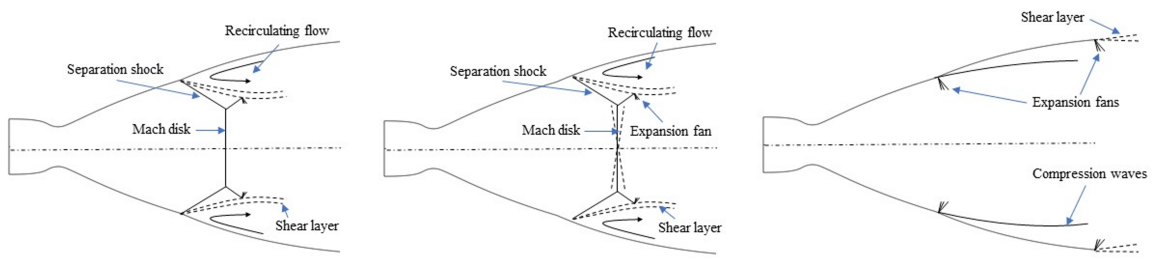


Figure 1.21: Sketch of the operating modes and flow development inside the Dual-Bell nozzle: (left) sea-level mode, (middle) transition mode and (right) high-altitude mode.

The DB nozzle was first proposed by Cowles and Foster [59] in 1949, and all the studies carried out since then highlighted three main critical issues: i) the transition between the two operating modes, ii) the detached flow unsteadiness in sea-level mode, and iii) the hot flow behavior and

¹ According to Schmucker [43], side loads are caused by a non-symmetrical shock-induced flow separation and the degree of this non-symmetric behavior is proportional to the inverse of the wall-pressure gradient magnitude (see Sec. 1.3.2). The inflection point in the dual-bell contour induces a Prandtl-Meyer expansion and, consequently, an infinite wall-pressure gradient (in the inviscid sense) thus zeroing the side-load magnitude.

cooling effects.

The first experimental test campaign was performed by Horn and Fisher [60] in 1993 using cold-gas sub-scale dual-bell nozzles. They found that both the constant-pressure and increasing-pressure extension exhibit good transition characteristics with a transition time of the order of 30 ms. Several numerical studies [56, 61] confirmed a quick transition behavior. In particular, Nasuti et al. [56, 62] found that the dual-bell extension with a positive pressure gradient can ensure a transition faster than the one with a constant pressure profile (CP). On the other hand, this profile can ensure higher thrust performances, and for this reason a trade-off is necessary.

After the experiments by Horn and Fisher, the transition phenomenon was studied through an extensive test campaign conducted at the German Aerospace Research Center (DLR) [63, 64], which investigated the effect of different geometrical parameters on the transition process and on the side-loads generation in cold-gas sub-scale nozzles. They found that both modes (sea-level and high-altitude) are associated to a level of side loads lower than the ones suffered by a comparable TIC nozzle. Nevertheless, the transition was characterized by a short-time high-peak side load, that could debase the nozzle structure. Verma et al. [65] studied the flow unsteadiness when the separation front was located in the inflection region by analyzing the spectral content of the wall-pressure signature. They related the onset of side loads during the transition in the inflection region to the high level of unsteadiness suffered by the flow in this regime (see Sec. 1.3.2). Proschanka et al. [66] performed a numerical study of a cold-gas dual-bell nozzle in sea-level mode, and found three types of pressure fluctuations: one symmetric and two asymmetric, the latter being associated with side-loads generation.

Another important aspect considered in literature was the effect of the launcher-base flow on the nozzle internal flow behavior. In this context, the investigation of the complex interaction of a dual-bell exhaust flow with the unsteady external flow is of particular interest, especially when the nozzle works in sea-level mode. As observed and demonstrated [67–69], an external pressure fluctuation can cause an internal amplification of the pressure oscillations, which can be dangerous for the side-loads generation. Verma et al. [70] suggested that the external unsteady perturbation could lead to a transition/re-transition cycle, generally known as flip-flop effect. The same results have been found by Bolgar et al. [71], which experimentally studied the interaction of an external transonic and supersonic flow with a dual-bell nozzle. Freestream supersonic conditions seem to trigger the flip-flop effect, while for transonic conditions the re-transition is eliminated. Loosen et al. [72] studied numerically the interference of a turbulent wake coming from a generic space launcher with a dual-bell nozzle exhaust flow in sea-level mode. It was found that in supersonic freestream conditions, the presence of the outer flow leads to a premature transition, thus reducing the transition NPR. The same results have been found experimentally and numerically by Barklage et al. [73], Martelli et al. [74] which demonstrated that the transition NPR and the movement of the separation point is particularly sensitive to the outer flow conditions and perturbations. Loosen et al. [72, 75] performed a simulation in transonic freestream conditions. They found an increased pressure oscillations level inside the nozzle, associated to an asymmetric mode in the azimuthal plane.

Most of the studies available in literature refer to cold-gas flow investigations. In real flight conditions however, the dual-bell nozzle would work with hot exhaust flow, and a film cooling technique could be used to protect the nozzle structure from thermal fatigue. Génin et al. [76]

performed one of the first experimental test campaign in order to study the nozzle behavior with inert hot air flow. The presence of the inflection point induces thermal loads during the transition process, and the generated heat flux raises in the inflection region. This phenomenon seems to happen in all the operation regimes. Moreover, during the first stage of the transition to high-altitude mode, the flow detachment contributes to the thermal loads growth. Martelli et al. [77] studied the effect of a film cooling injected in the base nozzle near the inflection point by means of numerical simulations. The emerging results highlighted the efficiency of the film which is strongly influenced by the expansion fan at the inflection point. Unfortunately, from the study emerges also that the secondary gas increases the inflection region extension, leading to an increased risk of side-loads generation.

From the analysis of the available literature, it is clear that the development of side loads inside the nozzle is one of the main critical aspects that must be taken under consideration for the development and the realisation of a dual-bell nozzle.

1.3.2 Side Loads Generation

At the very beginning, the asymmetric tilted separation surface that takes place in the Free Shock Separation (FSS) was considered the cause of the dangerous side loads [37, 43, 44].

The first research efforts were thus directed towards the development of analytical and empirical methods to predict the occurrence of side-loads and quantify their magnitude. Schmucker [43, 44] developed a model based on the idea of a tilted separation line, while Dumanov [78] considered oscillations of the separation line excited by random pressure pulsations in the separated flow region (see Fig. 1.22). These methods rely on many approximations and are primarily tailored to design purposes. However, after the Nave and Coffey [37] experimental study during which the RSS has been observed for the first time and the value of side loads that takes place during the transition from FSS to Restricted Shock Separation (RSS) was observed to be the highest value of side loads, research has been directed towards a more understanding of the physics phenomena involved in the flow separation inside the nozzle, i.e. the physics of the Shock-Wave/Boundary-Layer Interaction. Carrying out 2D Reynolds Average Navier-Stokes simulations, Nasuti and Onofri [39, 79, 80] tried to understand the reason for the formation of the trapped vortex behind the recompression shock and its role on the side-loads generation, then proven by experiments [81–87].

Although the first numerical simulations allowed to characterize the structure of the interaction properly, the experimental studies continued to highlight another fundamental topic: the unsteady behaviour of the side loads. The motion of the shock-system can be very important in the presence of separation zones. The frequencies of this motion are much lower than the characteristic frequencies of the incoming boundary layer, and this low-frequency unsteadiness generates large fluctuating forces that can be of severe magnitude. Thanks to his experimental study, Handa et al. [89] indicated two possible mechanisms for the shock oscillation. In one case, pressure disturbances, generated in the downstream turbulent separated region, force the shock to oscillate, resulting in a broad shape of the power spectral density. The other case foresees the reflection of a disturbance at the diffuser exit (**acoustic feedback**), resulting in a narrow-shaped power spectral density.

Baars et al. [42], Baars and Tinney [90], Baars et al. [91] experimentally investigated the pressure unsteadiness in TOP nozzle in both FSS and RSS regimes, using varying NPR conditions and a

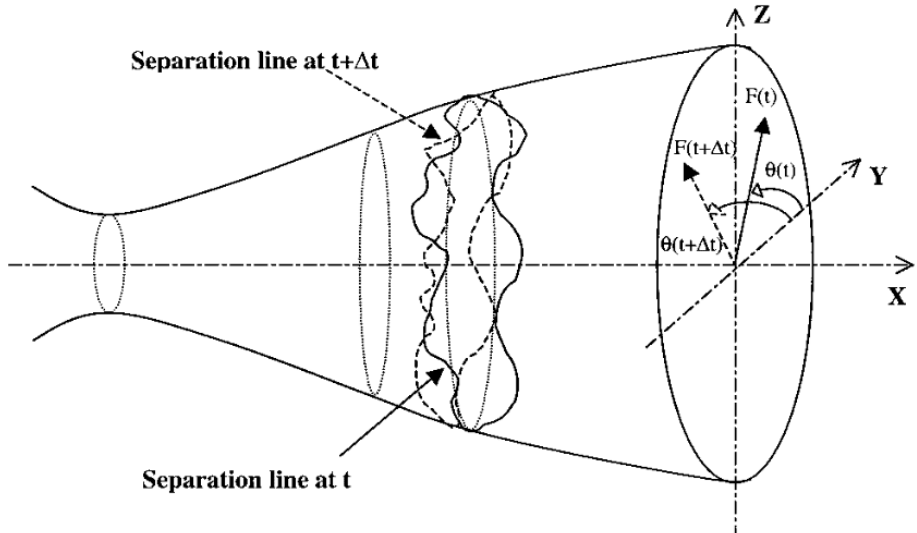


Figure 1.22: Schematic representation of the separation line unsteady movement in a generic nozzle [88].

time-frequency analysis. Scanning an entire range of NPR conditions, in a single run they found that the FSS state is dominated by low- and high-frequency humps associated to SWBLI and to the development of the turbulent shear layer. With such an approach it is difficult and costly to obtain converged statistics, but it is worth to mention that the sensors were placed in azimuthal arrays to isolate the anti-symmetric azimuthal mode, which is the only one responsible for side-loads creation.

Finally, based on the latter works, Jaunet et al. [92] carried out experiments on a Truncated Ideal Contoured (TIC) nozzle in FSS regime gradually varying the NPR to study the azimuthal Fourier modes associated to the pressure fluctuations, giving other information about the relation between this instability and the external jet flowfield. The analysis revealed a complex organization of the separated region pressure fluctuations. The low-frequency modes have been shown to be mostly axisymmetric and confined in the nozzle. The high-frequency signature of the developing mixing layer has been identified in the pressure signals and confirmed by its signature in the external velocity field. In addition, they also found highly organised pressure structures at an intermediate frequency range, mainly associated with the anti-symmetric pressure mode. They argued that these structures may be attributed to a screech-like mechanism [93] rather than to a transonic resonance. Moreover, the authors did not find any trace of the screech tone in the external ambient and speculated the existence of an aeroacoustic screech-like mechanism inside the nozzle, sustained by the presence of the internal subsonic flow region downstream of the Mach disk, which may provide a support for possibly upstream propagating waves. In this context, a more in-depth study was carried out recently by Bakulu et al. [94] and Martelli et al. [95].

Starting from all the suggestions about a correlation between the shock movement and the flow field downstream of the separation, it was argued that lateral forces are mainly due to oscillations of the internal shock system inside the nozzle. Only recently, research has been directed towards a more physical understanding of the origin of the aerodynamic loads and the consequent generation of lateral forces. The objective of the researcher community, actually, is to investigate the role of the pressure fluctuations in the fully separated region. The various frequency modes identified

are general features of the shock separation pattern and are confirmed by all the experimental and numerical work done so far. Nevertheless, the experimental campaigns of Ruf et al. [96] and of Baars et al. [42], Baars and Tinney [90], Baars et al. [91] on TIC and Thrust Optimized Parabolic (TOP) nozzles at several NPR have shown that, in addition to the wall-pressure spectra large bump in the low-frequency range associated to a breathing motion of the shock system and a broad and high amplitude peak at high frequencies generated by the turbulent activity of the detached shear layer, a distinct peak at an intermediate frequency (of the order 1000Hz) is observed to persist. Modal analysis has shown that this peak is clearly associated to the first non-symmetrical pressure modes and it is thus connected to the generation of side loads. These experimental campaigns opened the way for Computational Fluid Dynamics to the possibility of addressing important questions about the behavior of the wall-pressure signature and on the physical mechanisms leading to the generation of the aerodynamic loads. In addition, the numerical results can then be used to study the existence of the aeroacoustic screech-like mechanism inside the nozzle suggested by Jaunet et al. [92], as done by Bakulu et al. [94] and Martelli et al. [95].

1.4 High-Fidelity Numerical Simulations

As already discussed in Secs. 1.2 and 1.3, both SRMs and over-expanded nozzles in FSS are characterized by the presence of an aeroacoustic feedback loop that is able to induce pressure/thrust oscillations and lateral aerodynamic forces. It is evident that the experiments on both solid rocket motors and axi-symmetric nozzles suffer from the lack of flow measurements, due to the challenging flow conditions and absence of optical access. Therefore the physics of the separated flow inside SRMs and nozzles need to be investigated by numerical simulations. Due to the intrinsic limit of the Reynolds Average Navier-Stokes (RANS) methodology to capture the flow instabilities, other numerical methodologies had to be considered.

Unsteady Reynolds Average Navier-Stokes (URANS) simulations have been used in the past to evaluate the level of the side-loads in sub-scale models and rather good results were obtained by Deck and Guillen [88] and Deck and Nguyen [47]. Nevertheless, modelling the global effect of the turbulent scales as done in the URANS approach could hide the important flow processes leading to the formation of the aerodynamic unsteady loads. The same reasoning is valid for SRMs (see Sec. 1.2.2), in which URANS simulations are not able to capture the flow transition to turbulence, overpredicting the level of pressure oscillations inside the motor chamber [17, 31, 34]. This effect is of particular importance at burning times close to the ignition. For these reasons, high-fidelity numerical simulations are necessary to correctly capture the flow instabilities and the energy cascade process. For SRMs, a large-eddy simulation (LES) is a valid methodology that, given the flow Reynold number, is still affordable from a computational point of view. Moreover, it is worth to notice that, at the state of the art, most of the numerical studies on SRMs available in literature are based on quasi-1D models or 2D simulations, whereas 3D high-fidelity numerical simulations have appeared only recently [97, 98]. For realistic nozzles instead, performing a wall-resolved large eddy simulation LES of this kind of flows, characterised by Reynolds numbers of the order of 10^7 , requires impractically high computational expenses. Olson and Lele [99] performed LES at reduced Reynolds number, of the experiments of Johnson and Papamoschou [100], finding a certain level of agreement between the experimental data and the computed frequency of the shock displacement.

The origin of the unsteadiness was attributed to the confinement of the exit area by the separated flow. However, the point on the methodology still remains: the simulations were carried out at reduced Reynolds number.

In this context, a hybrid RANS-LES methodology as the Detached Eddy Simulation (DES) is a promising candidate to investigate the underlying physics. This methodology combines the efficiency of a Reynolds-averaged turbulence model in the attached boundary layer with the fidelity of the LES in separated regions (see Sec. 3.4 for further details). Nevertheless, very few DES simulations of separated nozzle flows can be found in literature. Deck [101] carried out a Delayed Detached Eddy Simulations (DDES) of the end-effect regime in an axisymmetric over-expanded rocket nozzle flow characterized by a RSS. Although the main properties of the flow motion were rather well reproduced experimentally, the computed main frequency resulted to be higher than in the experiment. Shams et al. [102] investigated the unsteady mechanisms that lead to the low-frequency peak of the side loads observed in this case and that is found to be characterized by an irregular azimuthal asymmetry of the reattached flow. Martelli et al. [103] carried out a DES of the transonic nozzle of Bogar et al. [104] at several nozzle pressure ratios. As the DES of Deck [101] the experimentally measured main properties of the flow motion were well reproduced but the computed main frequency resulted to be higher than in the experiment. However, they detected a low-frequency region associated with the shock movement and a higher-frequency region associated with the turbulent separated flow.

Regarding FSS, Larusson et al. [105] investigated the capability of a DDES employing the $k - \epsilon$ turbulence model to simulate the over-expanded supersonic nozzle flow with FSS, and the methodology was able to provide a satisfactory side-load estimate. Martelli et al. [95] performed a delayed detached eddy simulation on a overexpanded TIC nozzle in FSS and found a good agreement with the experimental results in terms of mean and fluctuating wall-pressure statistics. They also showed that, the unsteady Mach disk motion is characterized by an intense vortex shedding activity that, together with the vortical structures of the annular shear layer, contributes to the sustainment of an aeroacoustic feedback loop occurring within the nozzle, as speculated by Jaunet et al. [92] and further studied by Bakulu et al. [94]. The latter, performed an experimental test campaign and a DDES numerical simulation on the same TIC nozzle configuration. In this framework, few test cases of separated DB nozzle flows are reported in the literature [66, 72, 75]. However, these authors did not study the physics of the aeroacoustic feedback loop and the role of the inflection point on the side-loads generation.

1.5 Scope and outline of the thesis

The scope of the present dissertation is to study aeroacoustic resonance phenomena in space applications, characterized by compressible turbulent flows, by means of high-fidelity numerical simulations. To achieve this target, the equations of motion are first presented in Chapter 2, while the essential features of the most common numerical approaches that have been proposed so far to facilitate affordable numerical fluid dynamics simulations are described in Chapter 3: averaged, filtered and hybrid models to solve the equations of motion are discussed. The flow solver that has been used to perform all the subsequent numerical simulations is briefly discussed in Chapter 4.

After that, the results of a 3D Implicit Large-Eddy Simulation of the unsteady, single-phase,

compressible flow inside the ONERA C1xb SRM are presented in Chapter 5. The analysis focuses on the capability of the ILES approach to capture the aeroacoustic feedback loop, as well as the transition to turbulence of the coherent azimuthal rollers detached by the propellant corner and its influence on the generated acoustic feedback, measured by the pressure oscillation level.

Then, the aeroacoustic resonance developing inside a 3D rocket nozzle configuration has been studied, exploiting the delayed detached eddy simulation methodology. The nozzle geometry under investigation is a sub-scale Dual-Bell nozzle working in sea-level mode, for which experimental data are available. In this case, the analysis focuses on the DDES capability of capture the unsteady flow phenomena in order to assess the level of side loads suffered by the nozzle. The role of the dual-bell inflection point on the reduction of the aeroacoustic feedback loop is also investigated. The results are presented in Chapter 6.

Conclusions are finally discussed in Chapter 7, where some ideas for future works are also presented.

Chapter 2

Governing equations

In the present chapter, we briefly review the equations of the fluid mechanics, mainly for the purpose of completeness and to introduce the notation used in the rest of the work. We consider the motion of a Newtonian fluid, governed by the conservation principles of mass, momentum and energy. We assume that the conservation law for the angular momentum is identically satisfied, which implies symmetry of the stress tensor. In the following, we implicitly assume the continuum hypothesis to be valid. This is true when the Knudsen number ($Kn = \lambda/l$), i.e. the ratio of the mean free path λ to a typical flow dimension l , is small. Despite it seems difficult applying the continuum hypothesis within a shock wave, whose thickness is of the order of few mean free paths, the equations of motion predict shock structures that agree well with experiment [106].

2.1 Continuity

The conservation of mass density for a compressible fluid is expressed by the continuity equation

$$\frac{D\rho}{Dt} + \rho \nabla \cdot \mathbf{u} = 0. \quad (2.1)$$

Here $\mathbf{u} = u\mathbf{i} + v\mathbf{j} + w\mathbf{k}$ is the velocity vector and ρ is the density. The operator $D(\bullet)/Dt$ is the Lagrangian derivative, which expresses the variation of the fluid properties following the motion of the fluid particles, and that it is related to the local rate of change in an Eulerian frame $(\partial(\bullet)/\partial t)$ through

$$\frac{D(\bullet)}{Dt} = \frac{\partial(\bullet)}{\partial t} + \mathbf{u} \cdot \nabla(\bullet), \quad (2.2)$$

With eq. (2.2), the continuity equation can be cast in conservative form

$$\frac{\partial \rho}{\partial t} + \nabla \cdot (\rho \mathbf{u}) = 0, \quad (2.3)$$

or, in Cartesian components, assuming the Einstein convention for mute indices

$$\frac{\partial \rho}{\partial t} + \frac{\partial(\rho u_j)}{\partial x_j} = 0. \quad (2.4)$$

2.2 Momentum

The momentum equation stems from Newton's second law. Neglecting body forces, the momentum equation for a compressible flow is given by

$$\frac{\partial(\rho \mathbf{u})}{\partial t} + \nabla \cdot (\rho \mathbf{u} \otimes \mathbf{u} - \boldsymbol{\tau} + p \mathbf{I}) = 0, \quad (2.5)$$

where p is the pressure and $\boldsymbol{\tau}$ is the viscous stress tensor. The above equation is supplemented with the linear constitutive relation

$$\boldsymbol{\tau} = 2\mu \mathbf{S}^* = 2\mu \left[\mathbf{S} - \frac{1}{3} \text{tr}(\mathbf{S}) \mathbf{I} \right], \quad (2.6)$$

where

$$\mathbf{S} = \frac{1}{2} (\nabla \mathbf{u} + \nabla \mathbf{u}^T), \quad (2.7)$$

is the symmetric part of the velocity gradient tensor. The variation of the viscosity μ with temperature is assumed to be abide by Sutherland's law

$$\frac{\mu}{\mu_0} = \frac{T_0 + 110.3}{T + 110.3} \left(\frac{T}{T_0} \right)^{3/2}. \quad (2.8)$$

The momentum equation in Cartesian components takes the form

$$\frac{\partial(\rho u_i)}{\partial t} + \frac{\partial(\rho u_i u_j)}{\partial x_j} + \frac{\partial p}{\partial x_i} - \frac{\partial \tau_{ij}}{\partial x_j} = 0. \quad (2.9)$$

2.3 Energy

The energy equation states that the rate of change of the total energy is balanced by the rate of work done on the fluid element by the surface forces and the rate of heat added to the fluid by conduction. For a compressible fluid this can be written as

$$\frac{\partial(\rho E)}{\partial t} + \nabla \cdot (\rho \mathbf{u} H - \boldsymbol{\tau} \cdot \mathbf{u} + \mathbf{q}) = 0, \quad (2.10)$$

where E is the total energy per unit volume

$$E = \frac{p}{\rho(\gamma - 1)} + \frac{1}{2} \mathbf{u} \cdot \mathbf{u}, \quad (2.11)$$

where γ is the specific heat ratio and $H = E + p/\rho$ is the total enthalpy. The conductive heat flux \mathbf{q} in equation (2.10) is assumed positive by convention when it removes heat from the fluid element, and it is given by the Fourier law

$$\mathbf{q} = -\lambda \nabla T \quad (2.12)$$

where the coefficient λ is the heat conductivity of the fluid. For the sake of completeness, as made for the continuity and the momentum equation, we report the energy equation in Cartesian components

$$\frac{\partial(\rho E)}{\partial t} + \frac{\partial(\rho u_j H - \tau_{ij} u_i + q_j)}{\partial x_j} = 0. \quad (2.13)$$

The equations (2.1), (2.5) and (2.10), with the addition of the state equation

$$p = \rho R T \quad (2.14)$$

being R the gas constant ($R = 287.03 \text{ J/kg/K}$ for air), constitute a complete set describing compressible fluid flows.

The Navier-Stokes equations in conservative form can be written in compact form as

$$\frac{\partial \mathbf{u}}{\partial t} + \sum_{i=1}^3 \frac{\partial \mathbf{f}_i}{\partial x_i} + \sum_{i=1}^3 \frac{\partial \mathbf{g}_i}{\partial x_i} = 0 \quad (2.15)$$

where

$$\mathbf{u} = \begin{Bmatrix} \rho \\ \rho u_i \\ \rho E \end{Bmatrix}, \quad (i = 1, 2, 3), \quad (2.16)$$

is the vector of the conserved variables and

$$\mathbf{f}_j = \begin{Bmatrix} \rho u_j \\ \rho u_i u_j + p \delta_{ij} \\ \rho E u_j + p u_j \end{Bmatrix}, \quad \mathbf{g}_j = \begin{Bmatrix} 0 \\ \sigma_{ij} \\ \sigma_{ij} u_i + k \frac{\partial T}{\partial x_j} \end{Bmatrix} \quad (i = 1, 2, 3), \quad (2.17)$$

are the advective (Eulerian) and viscous fluxes in the j th coordinate direction, respectively.

Chapter 3

Methodology

In this chapter, the numerical methodologies adopted to solve the fluid dynamics equations are described and discussed.

Direct Numerical Simulations (DNS), consist in solving the NS equations with prescribed initial and boundary conditions, thus resolving all length and time scales to obtain a single realization of the three-dimensional and unsteady flow field. This method, however, appears to be unsuitable for the kind of flows proposed in this dissertation, which are characterized by high Reynolds numbers. Given the impractically high computational expenses of the DNS, this work will focus on other approaches that make such numerical simulations affordable.

At the beginning, the averaged equations of motion will be derived in Sec. 3.1. In this description, which allows an easier numerical solution, the system of the equations turns out to be unclosed and needs therefore a set of additional equations. The latter, must be suitable for application to general turbulent flows. Thus, turbulence modeling will be introduced.

A different approach consists in filtering the equations of the motion. Filtered equations will be then derived and the Large-Eddy Simulation (LES) will be described in Sec. 3.2.

The combination of the efficiency of a Reynolds-averaged turbulence model in the attached boundary layer with the high accuracy of the Large-Eddy Simulation in massively separated regions in hybrid methodologies represents a valid and promising approach. Hybrid models will be presented in Sec. 3.3 with particular attention to one of the most promising and cost-effective methodology, the Detached Eddy Simulation (DES) (see Sec. 3.4).

3.1 Reynolds Averaged Navier-Stokes Simulations

One of the most used approaches in solving the Navier-Stokes equations is the Reynolds-Averaged Navier-Stokes (RANS) simulation, in which only the mean flow field behavior is described by the averaged NS equations.

This method takes advantage of the overall averaging procedure to neglect most of the small turbulent scales and allow an easier numerical solution. The averaging operation on the non-linear equations leads to the formation of new unknowns in the problem, hence additional equations are required to close the system. Therefore, this approach foresees a statistical description of the turbulent phenomena through mathematical models. Fine turbulent scales are not resolved and a steady mean flow field that satisfies the averaged Navier-Stokes equations is obtained. This steady-

state solutions can be sought and highly anisotropic grids with high aspect and area ratio cells can be used near solid boundaries.

When the flow is strongly unsteady with non-turbulent origin (e.g. externally-enforced unsteadiness), the unsteady mean flow is resolved and the turbulent fluctuations are described by the turbulence model. This is possible because the time scale of the turbulence dynamics is smaller than the dynamics of the phenomenon that caused the unsteadiness¹. Such transient simulations are named Unsteady Reynolds Average Navier-Stokes (Unsteady Reynolds Average Navier-Stokes (URANS)) simulations. URANS simulations require a higher computational cost with respect to their steady-state version and show a stronger sensitivity to the model chosen.

3.1.1 Averaged Equations of Motion

In this section, the Reynolds averaging procedure to obtain the Reynolds Average Navier-Stokes (RANS) equations is presented. The classical procedure is based on Reynolds decomposition of the velocity and pressure fields to obtain the averaged equations of motion. Moreover, given the need to take into account compressibility effects (i.e. density and temperature fluctuations), the Favre averaging procedure is also presented.

Reynolds Averaged Navier–Stokes Equations

Reynolds averaging is commonly used, especially for incompressible, constant-property flows. According to this procedure the mean velocity field can be written as:

$$U_i(x_i, t) = \int u_i(x_i, t; \omega) \mu(d\omega) = \lim_{N \rightarrow +\infty} \frac{1}{N} \sum_{k=1}^N u_i(x_i, t; \omega_k) \quad (3.1)$$

that can be evaluated with time or space averaging, if the flow exhibits a stationary or homogeneous behaviour in some directions.

Given the definition of mean field, the Reynolds decomposition is such that

$$u_i(x_i, t; \omega) = U_i(x_i, t) + u'_i(x_i, t; \omega) \quad (3.2)$$

where $u'_i(x_i, t)$ is the instantaneous fluctuating component of the velocity field, for which, averaging eq. (3.2) gives

$$\overline{u'(x_i, t; \omega)} = 0 \quad (3.3)$$

For incompressible flows $\left(\frac{\partial u_i}{\partial x_i} = 0\right)$, the Reynolds decomposition allows to write the NS equations (eq. (2.3) and eq. (2.5)) for the mean field². These equations have a similar structure with respect to the original ones, and the only difference is the presence of a new term, the Reynolds stress tensor, which acts like an additional component of the molecular stress tensor.

Looking just to the continuity equation it can be seen how Reynolds averaging is quite demanding for cases like those taken into account in this work, in which significant density changes occur, even

¹Resolving motions larger than the simulation time step and modeling those smaller than these, requires a significant separation between the scales that is seldom present.

²For the incompressible case the energy eq. (2.10) is decoupled from the first two and so is not of direct interest.

when pressure changes are small.

Considering the Reynolds decomposition of velocity and density

$$\begin{aligned}\rho &= \bar{\rho} + \rho' \\ u &= U + u'\end{aligned}\tag{3.4}$$

substituting them into eq. 2.4 and considering eq. (3.3), it is possible to obtain that

$$\frac{\partial \bar{\rho}}{\partial t} = \frac{\partial}{\partial x_i} \left(\bar{\rho} U_i + \overline{\rho' u'_i} \right) \tag{3.5}$$

It is worthwhile to note that in order to achieve closure, an approximation for the correlation between ρ' and u' is needed.

The problem is even more complicated for the momentum equation where the Reynolds stress tensor originates from averaging the product $\rho u_i u_j$ that appears in the convective acceleration. Obviously, a triple correlation involving ρ' , u'_i and u'_j appears, thus increasing the complexity.

Favre Averaging

For flow configurations in which compressibility effects are important, an equation for the conservation of energy and an equation of state must be introduced. As the Reynolds averaging process gives rise to the Reynolds-stress tensor in the momentum equation, it is expected that similar averaging on the energy equation will lead to a turbulent heat-flux vector. It is also expected, as a consequence, that new compressibility-related correlations will appear throughout the equations of motion.

The problem of establishing an appropriate form of the averaged equations can be simplified by introducing the density-weighted averaging procedure suggested by Favre [107]. The new variables are commonly referred to as mass-averaged, even if density is strictly present in the definition. For example, for the velocity

$$\tilde{u}_i(x_i, t) = \frac{1}{\bar{\rho}(x_i, t)} \overline{\rho(x_i, t; \omega) u_i(x_i, t; \omega)} \tag{3.6}$$

where the overbar denotes the standard Reynolds-averaged quantity.

Once introduced the Reynolds decomposition into the definition in eq. (3.6), it follows that

$$\bar{\rho} \tilde{u}_i = \bar{\rho} U_i + \overline{\rho' u'_i} \tag{3.7}$$

Moreover, exploiting eq. (3.7), the mass conservation equation (3.5) can be rewritten as

$$\frac{\partial \bar{\rho}}{\partial t} + \frac{\partial}{\partial x_i} (\bar{\rho} \tilde{u}_i) = 0 \tag{3.8}$$

It is worth to notice that the form is identical to the laminar mass conservation equation. It is also important to note that the performed operation implies that the dependent variable is not the velocity anymore but the momentum per unit volume, ρu_i .

Similarly to what done before, the field is decomposed into a mass-averaged part and a fluctu-

ating part³. The Favre decomposition can be introduced as

$$u_i(x_i, t; \omega) = \tilde{u}_i(x_i, t) + u''_i(x_i, t; \omega) \quad (3.9)$$

In order to achieve the Favre average, eq. (3.9) is multiplied by ρ , and an ensamble average is performed, giving

$$\overline{\rho u_i} = \bar{\rho} \tilde{u}_i + \overline{\rho u''_i} \quad (3.10)$$

Comparing eq. (3.6) with eq. (3.10), the Favre average of the fluctuating velocity vanishes

$$\overline{\rho u''_i} = 0 \quad (3.11)$$

Viceversa, the standard Reynolds average of the mass-fluctuating part of the velocity is not zero. Using eq. (3.9)) and eq. (3.7) it is possible to obtain

$$u''_i = u_i - \tilde{u}_i = u_i - U_i - \frac{1}{\rho} \overline{\rho' u'_i} \quad (3.12)$$

and performing a Reynolds averaging

$$\overline{u''_i} = -\frac{1}{\rho} \overline{\rho' u'_i} \neq 0 \quad (3.13)$$

So as to mass-average the conservation equations, the following decomposition will be applied to the different flow variables:

$$\begin{aligned} u_i &= \tilde{u}_i + u''_i & \rho &= \bar{\rho} + \rho' & p &= \bar{p} + p' & h &= \tilde{h} + h'' \\ \mathcal{U} &= \tilde{\mathcal{U}} + \mathcal{U}'' & T &= \tilde{T} + T'' & q_j &= q_{Lj} + q'_j \end{aligned} \quad (3.14)$$

Note that the decomposition of p , ρ and q_j is written in terms of conventional averaged and fluctuating parts. Substituting eq. (3.14) into the Navier–Stokes equations and performing the mass-averaging operations, the result is the set of the Favre, mass-averaged mean conservation equations

$$\frac{\partial \bar{\rho}}{\partial t} + \frac{\partial (\bar{\rho} \tilde{u}_i)}{\partial x_i} = 0 \quad (3.15)$$

$$\frac{\partial (\bar{\rho} \tilde{u}_i)}{\partial t} + \frac{\partial (\bar{\rho} \tilde{u}_j \tilde{u}_i)}{\partial x_j} = -\frac{\partial P}{\partial x_i} + \frac{\partial}{\partial x_j} \left[\overline{\tau_{ji}} - \overline{\rho u''_j u''_i} \right] \quad (3.16)$$

$$\begin{aligned} \frac{\partial}{\partial t} \left[\bar{\rho} \left(\tilde{\mathcal{U}} + \frac{\overline{\rho u''_i u''_i}}{2} \right) \right] + \frac{\partial}{\partial x_j} \left[\bar{\rho} \tilde{u}_j \left(\tilde{h} + \frac{\tilde{u}_j \tilde{u}_i}{2} \right) + \tilde{u}_j \frac{\overline{\rho u''_i u''_i}}{2} \right] \\ = \frac{\partial}{\partial x_j} \left[-q_{Lj} - \overline{\rho u''_j h''} + \overline{\tau_{ji} u''_i} - \overline{\rho u''_j \frac{1}{2} u''_i u''_i} \right] + \frac{\partial}{\partial x_j} \left[\tilde{u}_i \left(\overline{\tau_{ij}} - \overline{\rho u''_i u''_j} \right) \right] \end{aligned} \quad (3.17)$$

with

$$P = \bar{\rho} R \tilde{T} \quad (3.18)$$

³ The mass-averaged part will be denoted with an over tilde, the fluctuating part with two apostrophes, similarly to a second derivative.

The first two equations are the same as the laminar case, except in eq. (3.16) for the presence of the Favre-averaged Reynolds Stress Tensor

$$\bar{\rho}\tau_{ij}^R = -\overline{\rho u_i'' u_j''} \quad (3.19)$$

which differs from the definition of the incompressible one, even if it is symmetrical too.

The third equation, eq. (3.17) is the Favre-averaged mean energy equation for total energy, since it includes several terms, each of which representative of a precise physical process or property.

On the left-hand side we can find:

- The internal energy, \tilde{U}
- The mean-flow kinetic energy per unit volume

$$\bar{\rho}\tilde{k} = \frac{1}{2}\bar{\rho}\tilde{u}_i\tilde{u}_i \quad (3.20)$$

- The turbulence kinetic energy per unit volume

$$\bar{\rho}k = \frac{1}{2}\bar{\rho}\overline{u_i'' u_i''} \quad (3.21)$$

On the right-hand side, other terms are identifiable:

- The turbulent transport of heat

$$qT_j = \overline{\rho u_j'' h''} \quad (3.22)$$

- The molecular diffusion

$$\overline{\tau_{ji}u_i''} \quad (3.23)$$

- The turbulent transport of turbulence kinetic energy

$$\overline{\rho u_j'' \frac{1}{2} u_i'' u_i''} \quad (3.24)$$

These two last terms, (3.23) and (3.24), arise because the mass-averaged total enthalpy appearing in the convective term of eq. (3.17) is

$$\tilde{H} = \tilde{h} + \tilde{k} + k \quad (3.25)$$

It is worth to notice that even if mass-averaging eliminate density fluctuations from the averaged equations, it does not remove their effects on the turbulence. Consequently, Favre averaging is just a mathematical simplification, not a physical one.

3.1.2 RANS Turbulence Modeling

The non-linearity of the NS equations leads to the appearance of momentum fluxes that act as apparent stresses throughout the flow. Since these momentum fluxes are unknown a priori, the system of the equations is no longer closed and additional equations have to be derived. Trying to find an equation for the evolution of the Favre-averaged Reynolds stress tensor, bring to new terms and, going further achieving a more complicated equation would bring to correlations of higher order and so on. This problem is known as closure problem. A closure approximation or a turbulence model

is needed to close the system.

Turbulence modeling consists in creating a mathematical model that approximates the physical behavior of turbulent flows. This has to be made by introducing the minimum amount of complexity while capturing the relevant flow physics. Most turbulence modeling focuses on the Reynolds stress terms. These are either solved directly, as in full second-moment Reynolds stress models, or defined via a constitutive relation for simpler models. Less attention is typically given to the other terms that need to be modeled. Particularly, sometimes the terms $\overline{\tau_{ji} u''_i}$ and $\rho u''_j \frac{1}{2} u''_i u''_i$ are even neglected [108].

For zero-, one- and two-equation models, the Boussinesq approximation with suitable generalization for compressible flows is the most used approach. Denoting the eddy viscosity by μ_T , the following form is assumed

$$\bar{\rho} \tau_{ij}^R = -\overline{\rho u''_i u''_j} = 2\mu_T \left(\widetilde{S}_{ij} - \frac{1}{3} \frac{\partial \widetilde{u}_k}{\partial x_k} \delta_{ij} \right) - \frac{2}{3} \bar{\rho} k \delta_{ij} \quad (3.26)$$

where now \widetilde{S}_{ij} is the mean strain rate tensor⁴.

The most important consideration in postulating eq. (3.26) is to guarantee that

$$\text{tr}(\tau_{ij}^R) = -2k \quad (3.27)$$

which means that the second eddy viscosity is identically $-\frac{2}{3}\mu_T$.

It is worth to notice that the Boussinesq hypothesis implies the anisotropy tensor \widetilde{a}_{ij} to be aligned with the deviatoric part of the Favre-mean strain rate tensor

$$\widetilde{a}_{ij} = \overline{\rho u''_i u''_j} - \frac{2}{3} \bar{\rho} k \delta_{ij} = -2\nu_T \widetilde{S}_{ij}^D \quad (3.28)$$

being symmetric and deviatoric, both \widetilde{a}_{ij} and \widetilde{S}_{ij}^D with five independent components. According to the turbulent viscosity hypothesis, these five components are related to each other through the scalar coefficient ν_T , but even in simple shear flow, it is found that this alignment does not occur. Specification by the turbulence model of $\nu_T(x_i, t)$ solves the problem of the Reynolds stress tensor closure.

In creating a mathematical model that approximates the physical behavior, the most used approach is applying the Boussinesq hypothesis (3.26), and trying to provide a scalar value of the eddy viscosity to close the RANS equations (Linear Eddy Viscosity Models (LEVM)). Since the beginning of the history of turbulence modeling, many researchers tried to provide equations for ν_T , developing n -equation models, which require the solution of n additional differential transport equations.

Zero-equation or algebraic models (mixing-length model), one-equation models (Spalart-Allmaras model) and two-equations (Menter SST, $k - \omega$ and $k - \epsilon$ models) all belong to this category of closure strategies.

⁴In the mean strain rate tensor, the Favre-averaged velocity is used instead of the Reynolds-averaged one.

Spalart-Allmaras Model (SA-RANS)

The model used in this dissertation is the one-equation model proposed by Spalart-Allmaras [109].

The reference source for the model is the Langley Research Center online page [110], in which all the model variants are presented, purged by all possible bugs present in the model literature. The model version used is the SA-noft2, because when using SA model as the basis for DES or derived methodologies, NASA reports that the f_{t2} term may cause an undesirable delay in transition to turbulence in the RANS region, and should be avoided.

The SA is a complete first-order closure in which a transport equation for a modified eddy viscosity is provided, which is in conservative form

$$\frac{\partial(\bar{\rho}\hat{\nu})}{\partial t} + \frac{\partial(\bar{\rho}\tilde{u}_j\hat{\nu})}{\partial x_j} = P_{\hat{\nu}} + D_{\hat{\nu}} - \epsilon_{\hat{\nu}} \quad (3.29)$$

where the production, diffusion and destruction terms are, respectively

$$P_{\hat{\nu}} = c_{b1}(1 - f_{t2})\hat{S}(\bar{\rho}\hat{\nu}) \quad (3.30)$$

$$D_{\hat{\nu}} = \frac{\bar{\rho}}{\sigma} \left[\frac{\partial}{\partial x_j} \left((\tilde{\nu} + \hat{\nu}) \frac{\partial \hat{\nu}}{\partial x_j} \right) + c_{b2} \frac{\partial \hat{\nu}}{\partial x_j} \frac{\partial \hat{\nu}}{\partial x_j} \right] \quad (3.31)$$

$$\epsilon_{\hat{\nu}} = \frac{1}{\rho} \left[\frac{c_{b1}}{K^2} - c_{w1}f_w \right] \left(\frac{\bar{\rho}\hat{\nu}}{d} \right)^2 \quad (3.32)$$

and $\hat{\nu}$ is the model working variable, related to the eddy viscosity by the equation

$$\widetilde{\mu_T} = \bar{\rho}\hat{\nu}f_{v1} \quad (3.33)$$

with the usual notation according to which, the tilde symbol means Favre-averaged quantity and where d is the distance from the nearest wall of the point in which the equation is considered, that is the turbulence characteristic length of the SA model.

Computing minimum distance by searching along grid lines or by finding the nearest wall grid point (or cell center) are incorrect operations and do not coincide in general with computing the actual minimum distance to the nearest wall. In fact, this distance is calculated solving a non-linear partial differential equation encountered in problems of wave propagation.

An improper calculation of d produces wrong results, for example, for such cases in which the grid lines are not perfectly normal to the body surface, or when the nearest body does not lie in the current grid zone. A practical example of the correct calculated wall distance is depicted in Fig. 3.1.

The other terms of the SA model are defined as:

$$f_{v1} = \frac{\chi^3}{\chi^3 + c_{v1}^3} \quad \text{with} \quad \chi = \frac{\hat{\nu}}{\tilde{\nu}} \quad (3.34)$$

$$\hat{S} = \max \left(\hat{\omega} + \frac{\hat{\nu}}{K^2 d^2} f_{v2}, 0.3\hat{\omega} \right) \quad \text{with} \quad \hat{\omega} = \sqrt{\tilde{\omega}_i \tilde{\omega}_i} \quad (3.35)$$

$$f_{v2} = 1 - \frac{\chi}{1 + \chi f_{v1}}, \quad f_w = g \left[\frac{1 + c_{w3}^6}{g^6 + c_{w3}^6} \right]^{1/6} \quad (3.36)$$

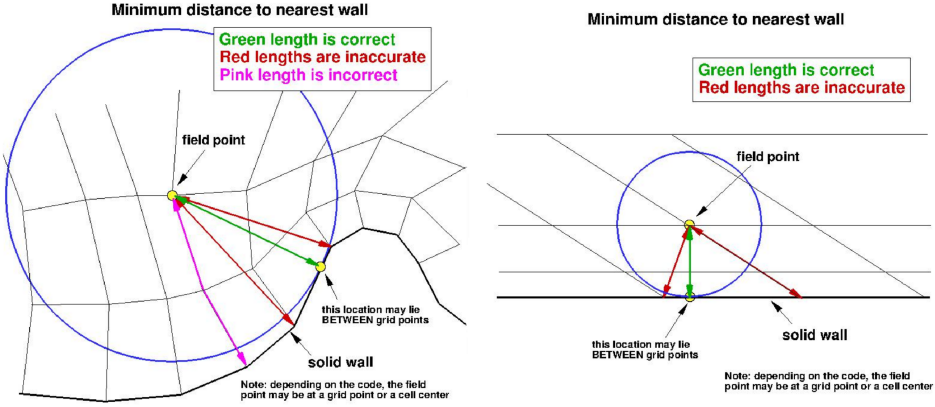


Figure 3.1: Minimum distance to nearest wall examples: correct, inaccurate and incorrect computations [110].

$$g = r + c_{w2}(r^6 - r), \quad r = \min \left[\frac{\hat{\nu}}{\hat{S}K^2 d^2}, 10 \right], \quad f_{t2} = c_{t3} \exp(-c_{t4}\chi^2) \quad (3.37)$$

The constant values are:

SA Constants			
c_{b1}	0.1335	c_{b2}	0.622
c_{w1}	$\frac{c_{b1}}{K^2} + \frac{1 + c_{b2}}{\sigma}$	c_{w2}	0.3
c_{w3}	2	c_{v1}	7.1
c_{t3}	0	c_{t4}	0.5
σ	2/3	K	0.41

Table 3.1: Spalart-Allmaras model constants [109].

3.2 Large-Eddy Simulations (LES)

The complexity and the computational effort of the numerical simulations can be reduced by removing from the resolved scales the smallest ones by means of a filtering operation.

Recalling the Kolmogorov hypothesis on isotropy of small scales and assuming a wide spectral separation (existence of a large enough inertial sub-range at high Reynolds number), the effect of the only excluded scales on the filtered variables can be taken into account through new modeled terms. Although LES inherits the requirements of three-dimensional spatial resolution and unsteady simulation from Direct Numerical Simulation (DNS), a reduction in computational cost is allowed by the empiricism introduced for the modeling of the new terms.

Pope [111] summarizes the conceptual points in LES development in:

1. Filtering operation⁵ in space, mathematically expressed in a convolution product, for a generic quantity $\phi(x_i, t)$

$$\bar{\phi}(x_i, t) = \int_V G_\Delta(r_i, x_i) \phi(x_i - r_i, t) dV \quad (3.38)$$

⁵Note that here the overbar symbol states a filtering operation and not an averaging procedure.

to decompose the field into the sum of a filtered (or resolved) component $\bar{\phi}(x_i, t)$ and a residual, or Sub-Grid Scale (SGS) component $\phi'(x_i, t)$

$$\phi(x_i, t) = \bar{\phi}(x_i, t) + \phi'(x_i, t) \quad (3.39)$$

Similarly to the procedure followed in Sec. 3.1.1, it is convenient to introduce a density-weighted filtering $\tilde{\phi} = \frac{\rho\bar{\phi}}{\rho}$. The filter width Δ has to be located at the beginning of the inertial sub-range to solve 80% of the energy [111], making LES less affordable at low Reynolds number where this range vanishes;

2. Derivation of the equations for the filtered variables from the Navier-Stokes equations that are of the same form of the RANS equation, with instead of the Reynolds stress tensor, a new unknown term describing the action of the unresolved scales on the resolved ones widely referred as *sub-grid stress tensor*;
3. Closure of the equations, obtained from the modeling of the sub-grid stress tensor, which depends on the filtering procedure adopted;
4. Numerical solution of the modeled filtered equations, which depends strictly on the filtering procedure, since the solved field does not have high frequency anymore and a numerical solution for frequency higher than the filtered cut-off does not provide additional information.

For the filtering operation it is possible to identify two different typologies:

- **Implicit filtering** in which Δ is less or equal to the grid spacing. No subgrid model is needed but a numerical method to provide the required dissipation is necessary (see Sec. 3.2.2);
- **Explicit filtering** in which Δ is greater than the grid spacing. The filter function is known a priori and the separation between solved and modeled scales is controllable, but it is wasteful in terms of the grid resolution, since turbulence is not resolved down to the smallest possible structure and no (or negligible) numerical dissipation is assumed.

From the point of view of the requirements in terms of grid matters, since in general the local structure of turbulence is unknown, an isotropic grid is suitable, and assuming isotropic large eddies, the coarsest grid direction dictates the resolution capability.

Owing to the fact that even at higher Reynolds number, a-priori grid design is difficult, some generic estimates have been accepted by the community for different kinds of flows. For example, for boundary layer flows the necessity of resolving the streak structures that develop around the buffer layer has brought to commonly-cited values for the resolution in terms of wall friction units ($\Delta x_{max}^+ \approx 40$, $\Delta z_{max}^+ \approx 20$, $\Delta y_{wall,max}^+ \approx 1$ and $\Delta y_{boundary,max}^+ \approx \max(\Delta x; \Delta z)$) and minimum domain size required ($6\ell_0$) to capture the scales in the energy-containing range [111]. In this way, the number of grid points estimated scales as $N_{xyz} \propto Re^{2.2}$ for structured grids.

The shrinkage of the large scales near the wall (near-wall damping effect on turbulence) dominates the computational cost of LES. This type of simulations for wall-bounded flows are also referred as quasi-DNS [112], since the advantage respect to direct numerical simulations is not as

much as expected⁶.

In the absence of a length-scale reducing effect due to the presence of wall boundary, as for the case of separated turbulent flows, the resolution restrictions are less severe, giving rise to the requirement of a fixed number of grid irrespective to the Reynolds number, that varies depending on the estimations (36^3 grid points for Pope [111] and 32^3 grid points for Spalart and Streett [113]). Furthermore, a sufficiently fine time step is required to properly capture the motion of the resolved turbulent structures since the LES methodology inherits from DNS not only the three-dimensionality but also the unsteadiness. Too large time steps that do not fulfill the CFL criterion cause a relaminarisation of the flow provoked by the time filtering effect.

3.2.1 The Smagorinsky Model

The first and simplest, but also the most widely-applied SGS model is that of Smagorinsky [114]. It is an algebraic eddy viscosity model, employing the Boussinesq hypothesis (in the form of eq. 3.26), to relate the sub-grid stress tensor to the local flow strain. It states that

$$\nu_{sgs} = (C_s \Delta)^2 S^* \quad \text{where} \quad S^* = \sqrt{2S_{ij}S_{ij}} \quad (3.40)$$

Under the assumption that the cut-off wave number lies in the inertial sub-range, it has been found that for isotropic turbulence $C_s = 0.1825$ [115], whereas for shear-driven flows is $C_s \in (0.08, 0.11)$ [116].

Even if it is the most widely-applied SGS model, it has some flaws, summarized below:

- The Smagorinsky parameter C_s should not be constant. A single global value, especially in mixed turbulence phenomena, is inappropriate.
- Given the constant and positive value of C_s , the model is incapable of predicting correct transition to turbulence, owing to the presence of non-zero eddy viscosity in sheared laminar flow.
- The model contribution does not vanish verging on DNS limit.
- The wall proximity in the viscous sublayer is not correctly represented.
- The model is purely dissipative, always extracting energy from the resolved scales. This prevents the modeling of reverse processes of back-scatter from small to large scales that happens locally in space inside the resolved field.

In order to solve these deficiencies, some dynamic SGS models have been conceived [117], in which C_s is computed dynamically and locally in space and time, although there are some problems with application for non-homogeneous flows.

3.2.2 Implicit LES (ILES)

The additional terms which account for turbulence in the LES model equations are in the order of $O(\Delta)$ (filter width), which in turn is in the order of the grid spacing, as discussed in Sec. 3.2. As such, the numerical truncation error interacts with the modelled terms. Implicit LES (ILES) is an

⁶The requested resolution according to [112] for capturing the near-wall layer is roughly ten times less expensive than for DNS.

approach in which the truncation error alone is taken as a closure model. In this dissertation, the numerical scheme we choose for ILES is the WENO scheme. This choice is dictated by convenience, since, as will be explained in Chapter 4, WENO is already implemented to deal with shock waves. Garnier et al. [118] find that WENO can be regarded as a very dissipative subgrid scale model. Grinstein et al. [119], on the other hand, identified the problem with WENO to be related to its formal high-order accuracy. The problem is expected to be mitigated when the high-order interpolation inherent to the scheme is applied to the reconstruction of variables rather than to the reconstruction of fluxes, as done in our implementation.

3.3 Hybrid Methods Simulations

As mentioned in the previous sections, the use of a Direct Numerical Simulation is far from being useful at industrial level, and the classical methods proposed for the resolution of practical turbulent flows may have some weaknesses:

- dissatisfaction with the RANS modelling paradigm. Despite the effort devoted and many models suggested, sources of uncertainty are significant, and the ideal model named by Wilcox [120] is far from being achieved, especially for separated flows;
- excessive cost for pure LES methods, mostly for flows involving wall boundaries albeit with a greater accuracy respect to RANS;
- computing demands gap between pure RANS and LES;
- need of unsteadiness description, with URANS not providing sufficient accuracy and with the increasing demands of field like aeroacoustics.

As a result, a series of techniques have been developed, trying to mix the benefits and features of both the RANS and the LES procedures. A comprehensive formulation-oriented review of *hybrid RANS-LES approaches* is present in Sagaut et al. [121], whereas in Fröhlich and von Terzi [122] the fundamental ambitions of these hybrid methodologies are exposed, subdivided in:

1. Very Large-Eddy Simulation (VLES): the possibility to use locally within the LES region a filter width at scales outside the inertial range, in order to use coarser grid;
2. WMLES: the use of RANS model as a sub-grid scale model, shifting the RANS/LES interface inside the boundary layer, hence reducing tangential grid requirements;
3. Regional and flow physics dependent RANS/LES activity: the application of different methodologies depending on the local flow features, like attached or separated.
4. Embedded LES: the user defines LES regions inside encircling RANS region.

3.4 Detached Eddy Simulations (DES)

In the context of the hybrid models, the Detached Eddy Simulation (DES) is certainly one of the most promising methodologies. It was introduced in 1997, when Spalart presented it to the scientific

community [112]. Since then, several research groups have been working on it all over the world (P.Spalart, M.Shur, M.Strelets and A.Travin are some of the major authors in the field).

A perfect definition of DES is given in Strelets [123], and its quote is mandatory since it describes all the principal characteristics of this hybrid methodology:

“[...] DES is a three-dimensional unsteady numerical solution using a single turbulence model, which functions as a subgrid-scale model in regions where the grid density is fine enough for an LES, and as a RANS model in regions where it is not.

The “fine enough” grid for an LES is that one whose maximum (over all three directions) spatial step Δ is much smaller than the flow turbulence length scale [...]. Thus in the LES regions little control is left to the model, and the larger, most geometry-sensitive, eddies are directly resolved. As a result, the range of scales in the solution and, therefore, the accuracy of the non-linear interactions available to the largest eddies are expanding when the grid spacing is decreasing. In other words, the model adjusts itself to a lower level of mixing, relative to RANS, in order to unlock the large-scale instabilities of the flow and to let the energy cascade to extend to length scales close to the grid spacing. In contrast in the RANS regions [...], the model has full control over the solution, which however remains unsteady and 3D even with a 2D geometry. Note that this situation is typical primarily for thin shear layers (either boundary layers or free mixing layers), which are precisely the flows where the RANS approach is known to be the most adequate in terms of computational cost, robustness, and credibility. An important feature of DES is that the approach is non-zonal and, as such, provides for a single velocity and eddy viscosity field, and there is no issue of smoothness between the RANS and LES regions.”

The industrial need of transient dynamics of separated flows as well as the control of noise and the capability to predict unsteady dynamic loads (as in the case of side loads for nozzle cases), meets perfectly the three-dimensionality and unsteadiness in the definition of this kind of simulation. Moreover, the expression “[...] using a single turbulence model” hides the non-trivial choice of a non-zonal approach, which brings the necessity of accurate and proper design of the grids used, but also the trust, for general applications, in the ability of an automatic method to simulate accurately wall turbulence also on coarse grids, which is a fact that has not been demonstrated [124].

An example of application is shown in Fig.3.2, in which the sharp geometry of a spoiler creates a region that is perfect for the use of LES, whereas the thin and extensive boundary layer is treated with RANS. The figure highlights also a zone of more sensitive separation and a reattachment region: in similar cases, this separation location is determined by the RANS model, and this could be a disadvantage considering the low performance of several turbulence models for flow separation.

Following the terminology defined by Spalart [125], used also by Mockett [126], the DES applications can be divided into:

Natural uses: only detached eddies are simulated and the procedure goes as described in the definition whereby RANS treats entirely the boundary layers, whereas LES works on massively separated flow: the third ambition named in Sec. 3.3 is satisfied until the RANS/LES interface breaks into the turbulent boundary layer.

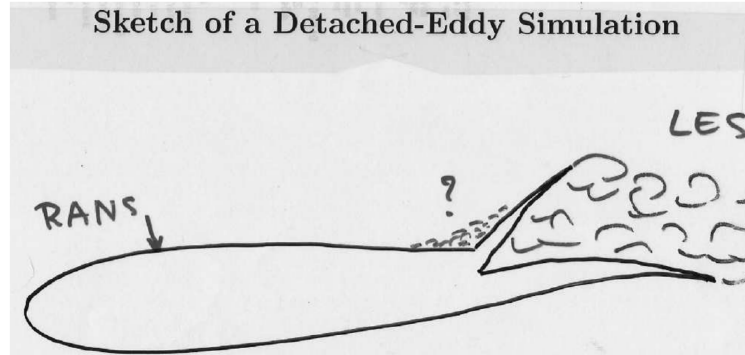


Figure 3.2: Original concept sketch of DES from the Spalart presentation of the 1997 [112].

Extended uses: even if not planned originally, recent application in Nikitin et al. [127] of DES tries to match the objectives of the second ambition of Sec. 3.3. It results to be successfull for certain aspects but with fundamental inaccuracy that will be described below.

Before entering into the practical implementations of the method, a first summary of the motivation of DES is illustrated Fig. 3.3.

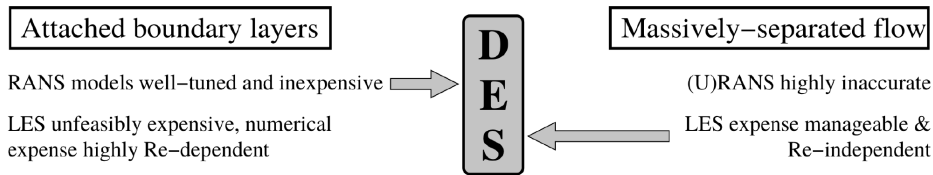


Figure 3.3: Summary of DES motivations. [126].

3.4.1 DES97

The original proposal of DES dates back to 1997 and goes by the name of DES97 [112]. It is based on the Spalart-Allmaras model [109] and exploits the presence of a defined length scale, since it is a complete turbulence model, that is the distance to the closest wall d in the destruction term (see Sec. 3.1.2).

Afterwards, a new DES length scale was introduced to substitute d everywhere in the equations that is

$$\tilde{d}_{DES97} = \min(d; C_{DES}\Delta) \quad \text{with} \quad \Delta = \max(\Delta x, \Delta y, \Delta z) \quad (3.41)$$

where Δ is the sub-grid length scale, which in the original version is such that if the grid is finer enough in a direction that has no influence on \tilde{d}_{DES97} , then the smallest resolved eddies scale with the coarsest grid cell dimension. Therefore, the eventual extra resolution would not be used.

Looking at the destruction term of the modified eddy viscosity transport equation of the SA model, in assumed conditions of local turbulence equilibrium ($P_{\tilde{\nu}} = D_{\tilde{\nu}}$), the eddy viscosity scales with the local flow strain rate S^* and $\tilde{\nu} \propto S^* d^2$, so that, substituting d with Δ , the Smagorinsky model for SGS eddy viscosity is recovered, and thanks to eq.(3.41), there is only a single model. It is worth to notice that the SGS model is dynamic but there is no reason to claim this as an advantage

over the Smagorinsky model, except maybe that it could be activated when transition occurs. Finally, eq.(3.41) is such that, if

- o $d < C_{DES}\Delta$, the model formulation is just the same as SA-RANS, due to the fact that the DES length scale is equal to the RANS one;
- o $d > C_{DES}\Delta$, which is in principle far from the wall, the LES filter width with the model constant C_{DES} is used, giving LES behavior.

It is important to know that the model constant C_{DES} was calibrated for SA-DES, comparing the results of Decaying Isotropic Turbulence (DIT) with experiments, and it is analogue to the Smagorinsky constant, with a numerical value of $C_{DES} = 0.65$. Moreover, the thickness of the boundary layer is not accounted in DES97, leading to a dangerous possible intrusion of LES inside RANS region, due to non appropriate grid design, as clarified in Sec. 3.4.2.

3.4.2 DES weaknesses

After the introduction of the DES technique by Spalart, some weaknesses have been identified by many authors and summarized in the review article of Spalart [128] and in Mockett [126].

Conceptual Issues

From the literature, it is evident that a more justified and better mathematically defined approach than DES is needed. Several hybrid methods have been proposed that split the turbulence energy in a specified ratio, but the actual strength of DES is that this division is local, depending on the condition of the flow, and if the non-zonal approach is used, does not imply an increase in user decision.

Another issue is the doubt about the order of accuracy of the method. The difficulty in demonstrating classical monotonic grid convergence and also the still missing establishment of a link between the DES flow field and the exact or DNS flow field, make the technique still immature from a theoretical point of view.

Modeled-Stress Depletion

Given the limited computational resources, the grid produced for the first DES simulations (see Fig.3.4 (a)) had a wall-parallel spacing considerably larger than the local boundary layer thickness ($\Delta_{||} \gg \delta$), allowing RANS to work without problems. However, this solution is not satisfactory in all situations and a grid refinement (with a grid convergence analysis) is needed. In this context, two types of grid can come out from mesh refinement. The first is a fine LES grid, shown in Fig. 3.4 (c), with the spacing greatly smaller than δ . This would allow the model to work as a SGS model over the bulk of the boundary layer, and as a RANS-like wall model close to the wall, with a grey layer in-between, resulting in a WMLES simulation that has, as pointed before, not perfect quantitative results.

The second possibility is to refine first in wall-parallel direction, obtaining the ambiguous grid in Fig.3.4 (b), in which the DES limiter is activated at approximately $2/3 \delta$. The encroachment of the RANS/LES interface inside the boundary layer can be unsafe for the numerical simulation. In fact,

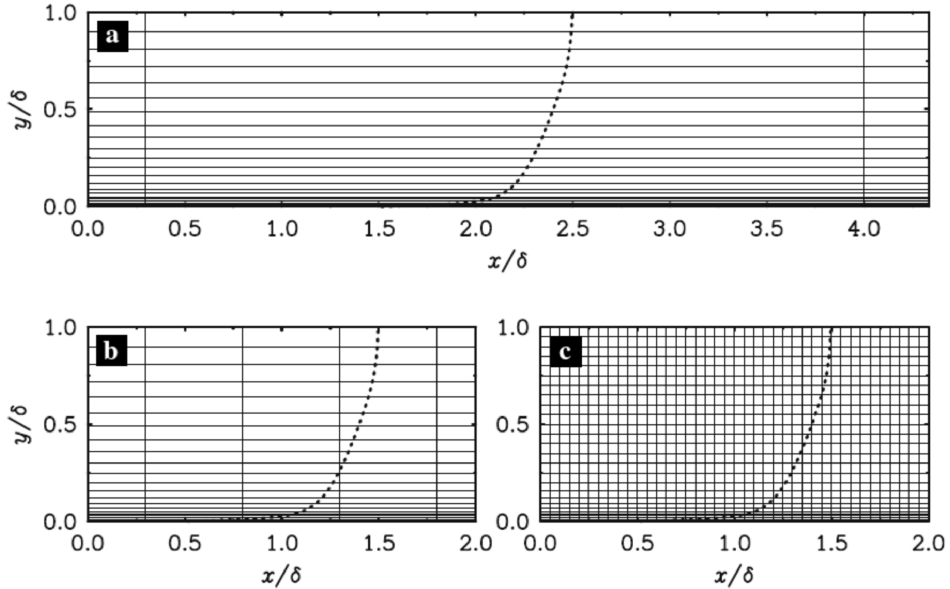


Figure 3.4: Grids typologies in boundary layers:(a) Natural DES grid; (b) grid with ambiguous spacing; (c) LES grid. In the z-direction, it is assumed that the spacing is similar to the wall-parallel one. The mean velocity profile is also reported (black dashed line) [129].

since the grid is not fine enough to support resolved velocity fluctuations inside the boundary layer (LES content), the switch to LES is anticipated. As result, the natural reduction of the modeled Reynolds stress is not balanced by the resolved stress, causing reduced levels of eddy viscosity, thus reducing the skin friction. This issue is known as Modeled Stress Depletion (MSD).

In some cases the reduction can be so severe that MSD can result in a Grid-Induced Separation (GIS) phenomenon [130], that is obviously a non-desired DES feature (see Fig.3.5)⁷. The solution proposed to this serious deficiency is to *shield* the boundary layer (see Sec. 3.4.3).

⁷It is worth to highlight that MSD can also occur when the boundary layer thickens and nearby separation (not only in response of a grid refinement).

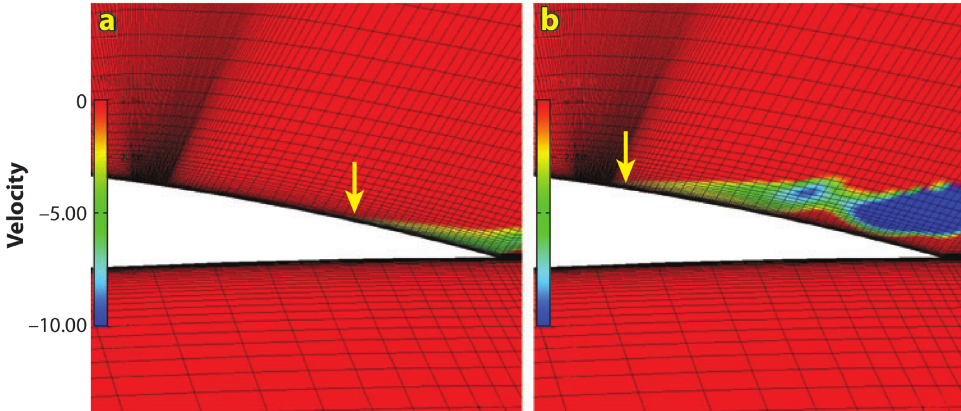


Figure 3.5: Velocity contour of an airfoil trailing edge that shows the GIS phenomenon:(a) RANS and (b) DES comparison. The arrows indicates the separation location [130].

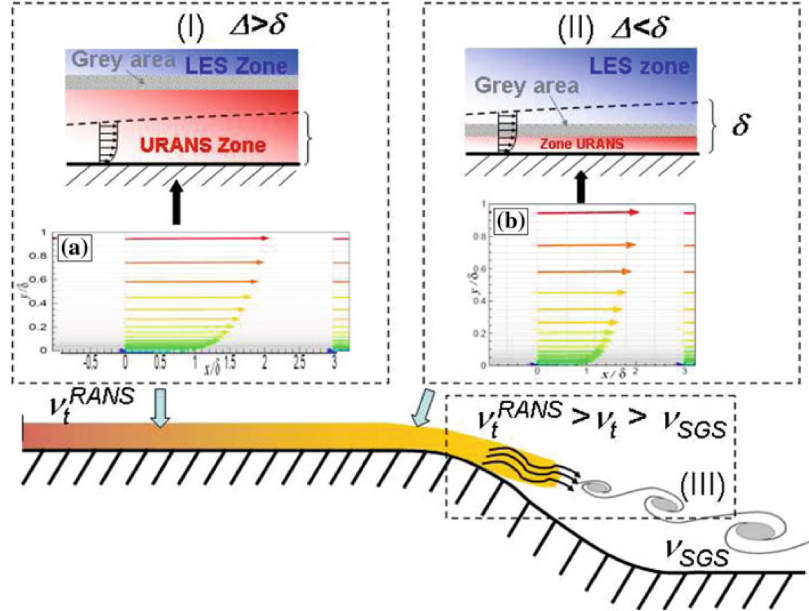


Figure 3.6: Possible situations for DES methodologies. Case (I): standard DES mode, case (II): possible MSD region and case (III): possible delay in the LES content formation [124].

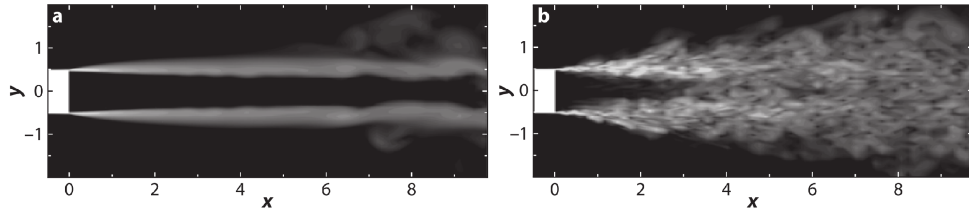


Figure 3.7: Vorticity contour in a jet: (a) standard DES and (b) implicit LES, with ν_T disabled. It is evident as standard DES on typical grids does not achieve a fast RANS/LES switch [128].

The Grey Area Problem and Slow LES Development in Mixing Layers

The DES methodologies, where the RANS branch models the attached boundary layers, can be considered as a weak RANS-LES coupling methods since any mechanism to transfer the modeled turbulence energy into resolved one is not provided.

Therefore, these kind of methods introduces a *grey area* between the two methodologies regions in which the solution is neither RANS nor LES. In fact, the switch is not instantaneous and a sudden change of resolution description does not appear. Essentially, across the interface between the two methodologies' regions, the eddy viscosity ν_T remains continuous but, in case of massively separated flows, characterized by a large-scale unsteadiness dominating the averaging process, the quick decrease of the level of modeled eddy viscosity enables strong instabilities. This results in fully-developed resolved turbulence immediately after the abrupt separation (e.g. the wakes of bluff bodies).

Moreover, first, the insufficient LES content after the switch can bring to unphysical results, like MSD or even GIS (see Fig.3.6 (II)), and second, a possible delay in the formation of instabilities in mixing layers due to the advection of the upstream RANS eddy viscosity can happen (see Fig.3.6 (III) and Fig.3.7), with disruptive departures from the physical solutions. The latter issue is fundamental in the aeroacoustics field.

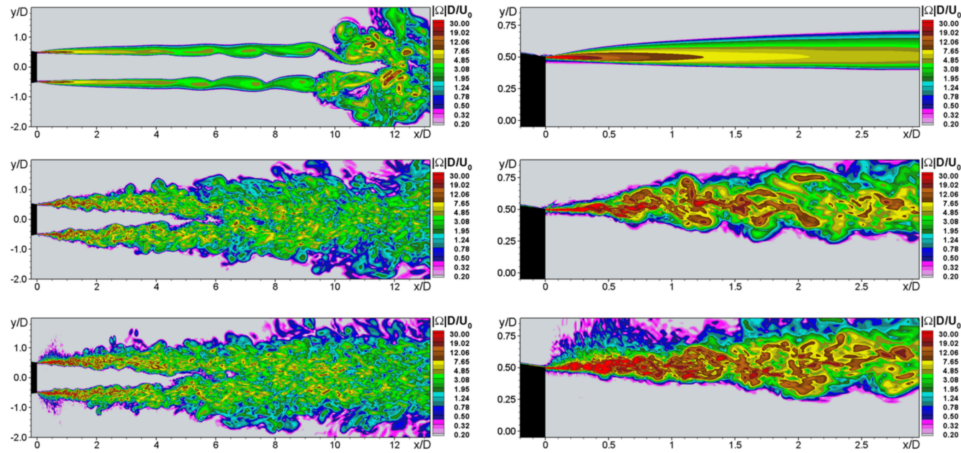


Figure 3.8: Vorticity magnitude of a jet flow in a meridian plane from SA-LES with: (first row) Δ_{max} and (second row) new Shear Layer Adapted subgrid length scale Δ_{SLA} . The figures on the right column are a zoomed visualization of the nozzle lip[131].

In order to try to solve the mentioned issue, modified techniques have been introduced (see Sec. 3.4.3), whereas to solve the switch failure of DES to in mixing layer, zonal approaches [124] and different Δ definitions have been proposed [124, 131]. The classical subgrid length used is Δ_{max} , which is totally independent from that of DES and is the safest possible definition.

Another possible choice is the cube root of the grid-cell volume, defined as

$$\Delta_{vol} = \sqrt[3]{\Delta x \Delta y \Delta z} \quad (3.42)$$

that is an ordinary choice with regular grids typical of LES regions, also if physically unjustified in a highly anisotropic grids. This is dictated by the fact that, even in favorable conditions, the smaller dimensions of a strongly anisotropic grid cell do not contribute to the grid resolution capability, and therefore have no place in the subgrid length scale, as instead do in Δ_{vol} . Nevertheless, given the fact that implicit LES often gives excellent results, it follows that small ν_T values are compensated by the numerical dissipation. This point is better exposed in Chapter 4.

Deck [124] and Shur et al. [131] proposed some different Δ formulations (e.g. the shear layer adapted Δ_{SLA}). These new definitions were found to depend on the grid spacing but also on the flow solution-dependent kinematic, leading to an important decrease of ν_{SGS} in regions of free and separated shear layers, unlocking Kelvin-Helmoltz instabilities and accelerating the transition to 3D flow structures. This is a key problem in the aeroacoustic field, especially in SRMs with facing steps and nozzles characterized by FSS or forced separation. An example of the aforementioned proposal is depicted in Fig. 3.8.

A full resolution of the grey area problem would involve the addition of more or less synthetic turbulent fluctuations at the onset of LES region that simulates the physical reality. This remains, at the state of the art, a demanding task to achieve.

Logarithmic-Layer Mismatch

In extended uses of DES [127], the RANS branch has been used to provide a wall model for LES. This was done combining grids similar to the case in Fig.3.4 (c), and enabling LES predictions at

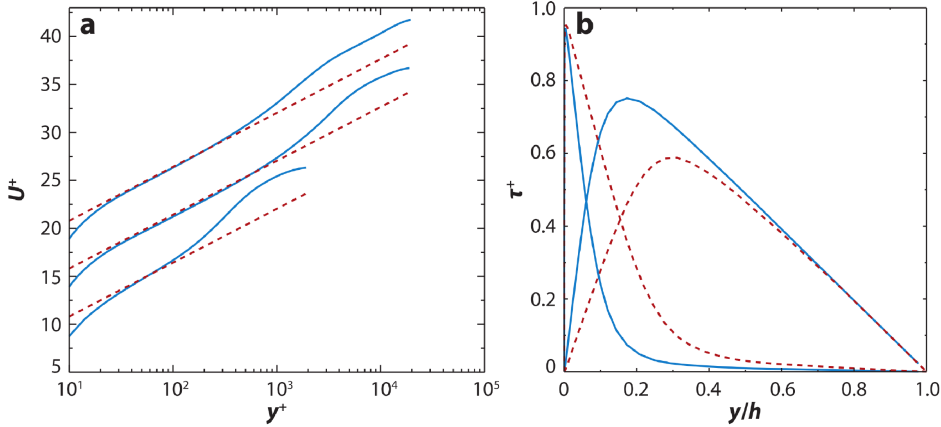


Figure 3.9: WMLES of the channel flow results: (a) velocity in wall units for different Reynolds numbers ($Re_\tau = 2000$ and 20000) and grid densities; the dashed line is the log-law. (b) modeled and resolved shear stress for the higher Reynolds number case for coarse (dashed) and fine (solid) grids [128].

unlimited values for the wall-parallel grid spacing in wall units ($\Delta_{||}^+$), resulting in a relevant cost advantage with respect to Quasi-DNS at Reynolds of realistic applications. In a channel flow, the described approach activates a WMLES in which the LES content is sustained near the center of the channel itself.

However, at sufficiently high Reynolds number, two different mean velocity profiles develop: one has a modeled log-layer and the other has a resolved log-layer. The slopes of these two layers are the same (i.e. same Kármán constant K), but their intercepts do not match as can be seen in Fig. 3.9. This problem is named as Logarithmic-Layer Mismatch (LLM) and causes an underestimation of the skin friction coefficient by about 15 %. Some studies reveal that this issue is the result of near-wall fluctuations being too weak and elongated.

Erroneous Activation of Near-Wall Damping Terms in LES Mode

In the SA model, there are low-Reynolds number terms designed to take into account for wall proximity (i.e. the ratio ν_T/ν). The problem arises in the LES branch of the DES after grid refinement and decrease in Reynolds number: the subgrid eddy viscosity is lowered and this is interpreted by the standard DES technique as the proximity to a wall, causing a strong fall of ν_T , due to terms as f_v .

The solution to this problem has been proposed by Spalart et al. [129], which introduces a correction factor (Ψ) to the LES length scale.

3.4.3 Delayed Detached Eddy Simulations (DDES)

For the purpose of resolving the problem of MSD explained in Sec. 3.4.2, the idea is to replace \tilde{d}_{DES97} with a new function $\tilde{d}(\ell_{RANS}, \ell_{LES})$. This function has the same limiting behavior, but depends on the physical solution through a sensor that detects the turbulent boundary layer, in order to keep $\ell_{RANS} = d_w$ when it is only somewhat larger than $\ell_{LES} = C_{DES}\Delta$. In this way, it is possible to override the DES97 limiter and to extend RANS modeling to a thicker layer.

Excluding zonal attempts, i.e. Zonal Detached Eddy Simulation (ZDES), the first proposed method for the resolution of the MSD problem was the GIS-shield proposed by Menter and Kuntz [130], which took advantage of the SST-based DES formulation. The F_2 blending function introduced in the model is used inside the DES length to extend the RANS region, thus mitigating the MSD problem.

The most famous shielding technique, and also the one used in the simulation of the Dual-Bell nozzle case analysed in this work (see Chapter 6), is the Delayed Detached Eddy Simulation (DDES) [129]. It is a proposal derived from GIS-shield method that is not limited to any turbulence model, as long as it involves an eddy viscosity. However, it is evident that the defined functions are strongly based on the Spalart-Allmaras model and also that a re-calibration of some parameters has to be done if turbulence is not treated with SA model. As mentioned, the new length scale \tilde{d} now depends on the eddy viscosity field, resulting in a time-dependency. The result is that the LES mode is denied if the new functions, presented below, indicate that the boundary layer is not ended. If massive separation takes place, the switch from RANS to LES occurs faster, resulting in a narrower grey area. This situation accelerates the growth of velocity fluctuations after natural instabilities in a region where the modeling of Reynolds stress is still legitimate.

The DDES length scale is defined as

$$\tilde{d} = d_w - f_d \max(0, d_w - C_{DES}\Delta) \quad (3.43)$$

where

$$f_d = 1 - \tanh[(8r_d)^3] \quad (3.44)$$

$$r_d = \frac{\nu_T + \nu}{\sqrt{U_{i,j}U_{i,j}}K^2d^2} \quad (3.45)$$

where ν_T is the kinematic eddy viscosity, ν is the molecular kinematic viscosity, $U_{i,j}$ is the velocity gradient⁸, K is the Kármán constant. Similarly to r in SA model:

- $r_d = 1$ in logarithmic layer;
- $r_d \rightarrow 0$ towards the edge of the boundary layer.

The very near-wall behavior integrity is ensured by the additional ν at the numerator, which guarantees that r_d is different from 0 very near to the wall.

The function f_d is such that:

- $f_d \approx 1$ in the LES region, where $r_d \ll 1$. In this way \tilde{d} is like in DES97;
- $f_d = 0$ in the boundary layer. In this way $\tilde{d} = d_w$ like in RANS;
- its value is insensitive to $r_d \gg 1$ very near the wall.

The value 8 and the exponent 3 are based on intuitive shape requirements for f_d and on tests of SA-based DDES on flat-plate boundary layer. In fact, a value larger than 8 for the factor constants

⁸ $\sqrt{U_{i,j}U_{i,j}}$ may also be written more explicitly as $\left[\sum_{i,j} \left(\frac{\partial u_i}{\partial x_j} \right)^2 \right]^{\frac{1}{2}}$.

would delay too much the LES region. It is reasonable that for different turbulence models these constants could be different. For example, after a re-calibration on Menter's SST-based DDES, in order to have approximately the same shielding of the boundary layer, i.e. the same trend in the boundary layer of the function f_d , the constants become 20 and 3 [132, 133]. A comparison of the two mentioned models is shown in Fig. 3.10 for the calibration case of a flat plate boundary layer under zero pressure gradient.

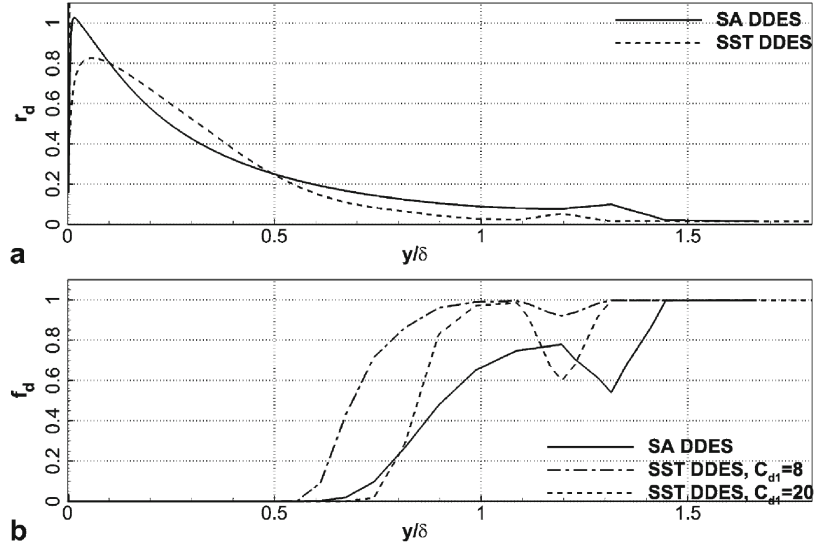


Figure 3.10: Comparison between SA- and SST-based DDES for the calibration case of a flat plate boundary layer under zero pressure gradient:(a) r_d parameter and (b) f_d function [132].

Chapter 4

Finite Volume Solver

In this chapter, the numerical and computational methodology adopted and the initial and boundary conditions implemented are addressed.

A Finite Volume (FV) solver is perhaps the most natural choice if one deals with compressible flows and with the integral form of the Navier–Stokes equations. Moreover, the latter is able to hold discontinuous solutions (e.g. shocks), and our direct discretization of them falls in the shock capturing scheme methodology. However, in this context, the FV method is not the exclusive technique one can use, as many different approaches have been successfully used, such as Finite Difference (FD) and Finite Elements (FEM) among others.

In this chapter, the discretization procedure for the Navier–Stokes equations is treated in Sec. 4.1 and Sec. 4.2, the WENO reconstruction and the viscous fluxes are discussed in Sec. 4.3, Sec. 4.4 and Sec. 4.6, the time integration procedure is described in Sec. 4.5 and the numerical boundary conditions in Sec. 4.7. Finally, a briefly description of the numerical implementation and the parallelization is given in Sec. 4.8.

4.1 Discretization procedure

The discretization procedure is based on the method of lines in decoupling the approximation of the spatial and temporal terms of the equations. The spatial domain is split into grid cells, and equation (2.15) is rewritten for the generic discrete volume $V_{i,j,k}$ composing the grid as

$$\frac{d\mathbf{U}_{i,j,k}}{dt} + \frac{1}{V_{i,j,k}} \sum_f [\mathbf{F}'_f S_f] = \frac{1}{V_{i,j,k}} \sum_f [\mathbf{G}'_f S_f] \quad (4.1)$$

where the summation has to be performed on all the faces delimiting the discrete volume, which are identified by the subscript f . Since the grid is structured, (i, j, k) is used to locate the discrete volume. $\mathbf{U}_{i,j,k}$ represents the integral mean of \mathbf{U} (see eq. 4.2), while \mathbf{F}'_f and \mathbf{G}'_f are approximations of the fluxes on the generic face f . The integral mean is defined as

$$\mathbf{U}_{i,j,k} = \frac{1}{V_{i,j,k}} \int_{V_{i,j,k}} \mathbf{U} dV \quad (4.2)$$

The resulting discrete quantity $\mathbf{U}_{i,j,k}$ is assumed to be concentrated in the cell centroid, defined as

$$\mathbf{x}_{i,j,k}^c = \frac{1}{V_{i,j,k}} \int_{V_{i,j,k}} \mathbf{x} \, dV \quad (4.3)$$

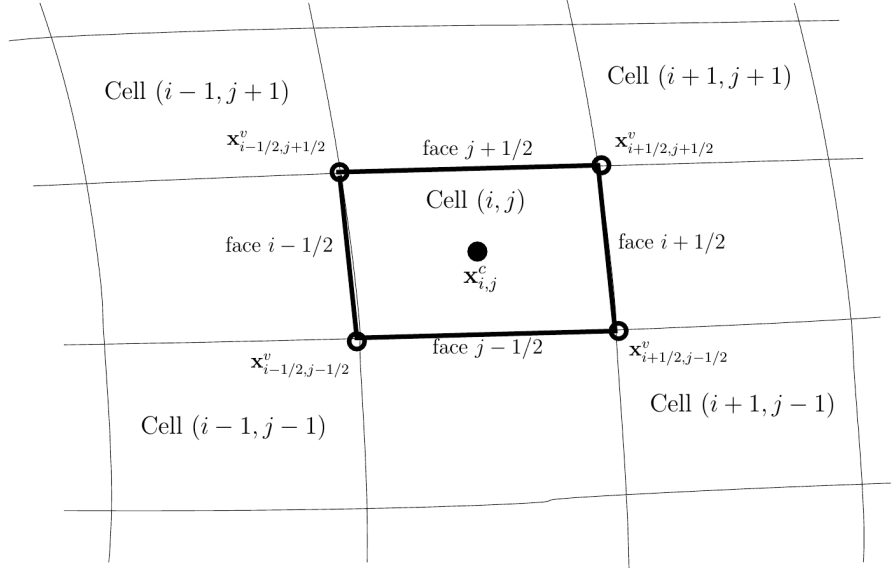


Figure 4.1: Notation used for the grid cells. Grid sketch is in the $x - y$ plane. The grid is uniformly extruded in the third dimension.

Fig. 4.1 shows the used terminology, where face f for cell (i, j) cycles through faces $i + 1/2, j + 1/2, i - 1/2, j - 1/2$. For the sake of clarity, we assume always to have a two-dimensional grid in the (x, y) plane, as the third dimension can be easily extrapolated. In fact, most of the grid quantities can be obtained in two dimensions. Assuming that each face with normal lying in the $x - y$ plane is also a plane surface, it can be shown that the (x, y) components of the centroid $\mathbf{x}_{i,j,k}^c$ can be exactly computed with the formula

$$\mathbf{x}_{i,j,k}^c = \frac{1}{3} \sum_{v=1}^4 \bar{\mathbf{x}}_{v+1/2} [(\mathbf{x}_v \wedge \mathbf{x}_{v+1}) \cdot \hat{\mathbf{z}}] \quad (4.4)$$

where the fractional subscript $v + 1/2$ will be widely used to denote quantities at the cell interfaces. The overline above the half-indexed symbols denotes the arithmetic mean

$$\bar{\varphi}_{l+1/2} = \frac{1}{2} (\varphi_l + \varphi_{l+1}) \quad (4.5)$$

and \mathbf{x}_v is a redefinition of $\mathbf{x}_{i+1/2,j+1/2,k+1/2}^v$ (coordinate of the grid vertices, also called nodes) used for compactness of the formula, such that

$$\begin{aligned} \mathbf{x}_{v=1} &= \mathbf{x}_{i-1/2,j-1/2,k-1/2}^v & \mathbf{x}_{v=2} &= \mathbf{x}_{i+1/2,j-1/2,k-1/2}^v \\ \mathbf{x}_{v=3} &= \mathbf{x}_{i+1/2,j+1/2,k-1/2}^v & \mathbf{x}_{v=4} &= \mathbf{x}_{i-1/2,j+1/2,k-1/2}^v \\ \mathbf{x}_{v=5} &= \mathbf{x}_{v=1} \end{aligned}$$

In the $\hat{\mathbf{z}}$ direction an equispaced extrapolation is considered. Therefore, the centroid third component can be computed as the mean of the third component of vertices.

4.2 Discretization of convective terms

The convective or Eulerian fluxes on the cell faces can be straightforwardly approximated as performed by Hirsch [134] in eq. (6.2.8). Considering the generic face $i + 1/2$, the flux can be written as

$$\mathbf{F}'_{i+1/2,j} = \frac{1}{2} (\mathbf{F}'_{i,j} + \mathbf{F}'_{i+1,j}) \quad (4.6)$$

Once the flux is expressed on each face, the resulting scheme is conservative. As result, the discrete conservation of conserved quantities is guaranteed also at a discrete level, that is, no artificial source terms is introduced numerically, and the temporal variation of the discrete \mathbf{U} is only due to the fluxes across the boundary of the considered volume. Referring to Fig. 4.2, if we consider a volume

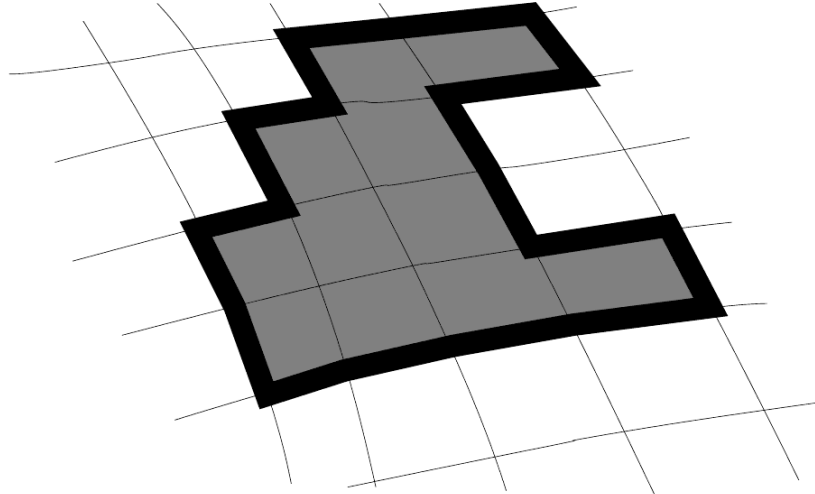


Figure 4.2: Two-dimensional schematic representation of the compound volume used to illustrate the discrete conservation property. The grey filled area is $\bigcup V_{i,j,k}$. The thick black solid line is the border $\partial(\bigcup V_{i,j,k})$.

composed by the union of different discrete cells, the definition of the integral mean on that volume is the volume-weighted average of the discrete $\mathbf{U}_{i,j,k}$ on the cell composing the new control volume, that is

$$\int_{\bigcup V_{i,j,k}} \mathbf{U} dV = \sum_{cells} \int_{V_{i,j,k}} \mathbf{U} dV = \sum_{cells} V_{i,j,k} \mathbf{U}_{i,j,k} \quad (4.7)$$

and from eq. (4.1)

$$\frac{d}{dt} \int_{\bigcup V_{i,j,k}} \mathbf{U} dV + \sum_{cells} \sum_{faces} [\mathbf{F}'_f S_f] = \sum_{cells} \sum_{faces} [\mathbf{G}'_f S_f] \quad (4.8)$$

In this way, each face belongs to two adjacent cells. Moreover, a flux contributing in a negative way in a cell, contribute in a positive way in the other cell, so that the sums $\sum_{cells} \sum_{faces}$ cancel out to be

$$\sum_{\partial(\bigcup V_{i,j,k})} .$$

Since the integral¹ formulation is able to handle discontinuities, the conservative formulation, which resemble the integral formulation at a discrete level, is also able to handle them. In this respect, the Lax-Wendroff theorem holds [134]:

Theorem 1 (Lax-Wendroff): If the solution of the discretized system (4.1) converges boundedly almost everywhere to some function $\mathbf{u}(\mathbf{x}, t)$ when $\Delta\mathbf{x}$, Δt tend to zero, then $\mathbf{u}(\mathbf{x}, t)$ is a weak solution of the equations.

This property is related to the conservation of the first integrals at a discrete level. One can expect that the conservation of also higher order integrals at a discrete level could be beneficial for the numerical solution. Indeed, Pirozzoli [135, 136] shows that the discretization of a particular form of the equations brings a conservative scheme, which also conserves a quadratic integral, the kinetic energy, in the limit of inviscid, incompressible fluid. Codes fulfilling these conservation properties also at a discrete level gain a non-linear stability which enables them to run without the addition of artificial, numerical viscosity. These works justify the choice of an approximation for convective fluxes slightly different than eq. (4.6)

$$\mathbf{F}'_{i+1/2,j} = \bar{u}'_{i+1/2,j} \begin{Bmatrix} \bar{\rho}_{i+1/2,j} \\ (\bar{\rho}\bar{\mathbf{u}})_{i+1/2,j} \\ (\bar{\rho}\bar{H})_{i+1/2,j} \end{Bmatrix} + \bar{p}_{i+1/2,j} \begin{Bmatrix} 0 \\ \hat{\mathbf{n}}_{i+1/2,j} \\ 0 \end{Bmatrix} \quad (4.9)$$

$$\mathbf{F}'_{i,j+1/2} = \bar{u}'_{i,j+1/2} \begin{Bmatrix} \bar{\rho}_{i,j+1/2} \\ (\bar{\rho}\bar{\mathbf{u}})_{i,j+1/2} \\ (\bar{\rho}\bar{H})_{i,j+1/2} \end{Bmatrix} + \bar{p}_{i,j+1/2} \begin{Bmatrix} 0 \\ \hat{\mathbf{n}}_{i,j+1/2} \\ 0 \end{Bmatrix} \quad (4.10)$$

where $\bar{u}'_{i+1/2,j} = \bar{\mathbf{u}}_{i+1/2,j} \cdot \hat{\mathbf{n}}_{i+1/2,j}$, and $\hat{\mathbf{n}}_{i+1/2,j}$ is computed exactly on each face, and the normal $\hat{\mathbf{n}}_{i+1/2,j}$ is always assumed to point towards greater i , so that for cell i the external normal on face $i+1/2$ is $\hat{\mathbf{n}}_{i+1/2,j}$, and on face $i-1/2$ is $-\hat{\mathbf{n}}_{i-1/2,j}$ (see Fig. 4.3). In this way, it is possible to rewrite eq. (4.1) as

$$\begin{aligned} \frac{d\mathbf{U}_{i,j,k}}{dt} &+ \frac{1}{V_{i,j,k}} \left(\mathbf{F}'_{i+1/2,j} S_{i+1/2,j} - \mathbf{F}'_{i-1/2,j} S_{i-1/2,j} \right) + \\ &+ \frac{1}{V_{i,j,k}} \left(\mathbf{F}'_{i,j+1/2} S_{i,j+1/2} - \mathbf{F}'_{i,j-1/2} S_{i,j-1/2} \right) = \\ &= \frac{1}{V_{i,j,k}} \left(\mathbf{G}'_{i+1/2,j} S_{i+1/2,j} - \mathbf{G}'_{i-1/2,j} S_{i-1/2,j} \right) + \\ &+ \frac{1}{V_{i,j,k}} \left(\mathbf{G}'_{i,j+1/2} S_{i,j+1/2} - \mathbf{G}'_{i,j-1/2} S_{i,j-1/2} \right) \end{aligned} \quad (4.11)$$

The choice of the form of eq. (4.9) for the fluxes is the analogous of the Blaisdell et al. [137]

¹The time variation of the integral mean quantities over the compound volume depends just on the fluxes on the edge faces of the compound volume itself, without the appearance of artificial internal sources.

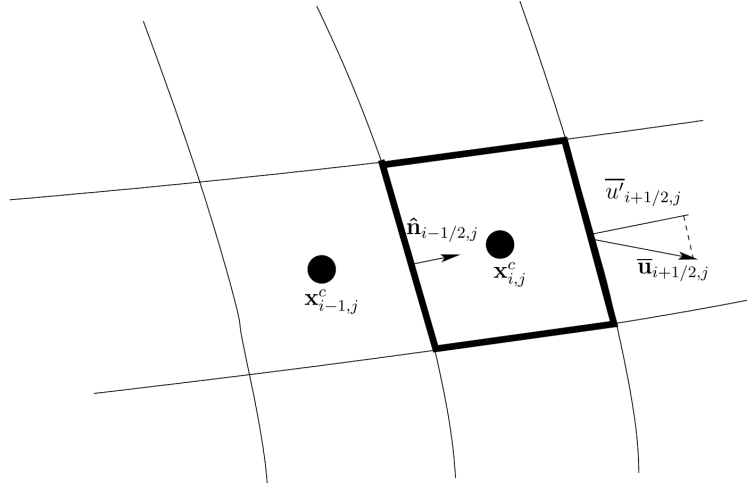


Figure 4.3: Schematic of the face normal convention adopted. Grid sketch is in the $x - y$ plane.

splitting in the Finite Difference framework, and the same advantages may be expected when used in the Finite Volume approach. Indeed, if we consider the second order expansion in a periodic domain for the flux of the continuity equation, we have

$$h_{i+1/2} = 2 \sum_{k=1}^r \sum_{l=1}^k A_{i-k+l, i+l} \frac{\rho_{i+l} + \rho_{i-k+l}}{2} \frac{u'_{i+l} + u'_{i-k+l}}{2} \quad (4.12)$$

and for second order we have $r = 1$ and $A_{i,i+1} = 1/2$, thus yielding

$$h_{i+1/2} = \frac{\rho_{i+1} + \rho_i}{2} \frac{u'_{i+1} + u'_i}{2} \quad (4.13)$$

The choice of using the Blaisdell et al. [137] splitting is due to the fact that, in this work, the results were almost coincident with the ones obtained with the Kennedy and Gruber [138] splitting, but at a lower computational cost. It is worth to note that, as reported also by Pirozzoli [136] and Blaisdell et al. [137], the splitting does not increase the stability through the conservation of the kinetic energy, but through the minimization of the aliasing error.

The use of centered stencils leads to a second-order accurate, non-dissipative scheme on Cartesian meshes. These properties are maintained for sufficiently smooth varying mesh sizes [134]. However, flow traveling through a discontinuity, such as a shock, must encounter some dissipation, also in the limit of vanishing viscosity. Therefore, the use of the formula of eq. (4.9) alone is conceptually wrong in the presence of a shock, since no dissipation is added through the shock itself. We overcome this problem by using formula (4.9) alone in regions of the flow where there are no shocks, and by correcting this flux by adding an artificial diffusion derived by the WENO (Weighted-Essentially Non-Oscillatory) scheme [139] only in regions with shocks. The shocks are located through a modified Ducros sensor [140]

$$\Theta = \max \left(-\frac{\nabla \cdot \mathbf{u}}{\sqrt{(\nabla \cdot \mathbf{u})^2 + (\nabla \times \mathbf{u})^2 + \varepsilon}}, 0 \right) \quad (4.14)$$

$$\varepsilon = \left(\frac{u_\infty}{c} \right)^2 \quad (4.15)$$

which is defined on each computational cell. On the faces, the value representing the sensor is chosen to be

$$\Theta_{i+1/2,j} := \max(\Theta_{i,j}, \Theta_{i+1,j}) \quad (4.16)$$

$$\Theta_{i,j+1/2} := \max(\Theta_{i,j}, \Theta_{i,j+1}) \quad (4.17)$$

and the discontinuity is located assuming a threshold value for Θ . The one used throughout this work is $\Theta = 0.05$, unless otherwise stated. When the value across a face is greater than the threshold Θ , a dissipative flux is added.

4.3 WENO Reconstruction

The dissipative artificial fluxes are obtained following the approach of Shu [141], where the WENO reconstruction is applied to the conserved variables, and the reconstructed values are inserted in the Lax-Friedrichs flux, whose expression for the one-dimensional model problem can be expressed as

$$F(U(x_{i+1/2}, t)) \simeq \frac{F(U_{i+1/2}^-, t) + F(U_{i+1/2}^+, t)}{2} - \frac{\alpha}{2}(U_{i+1/2}^+ - U_{i+1/2}^-) \quad (4.18)$$

$$\alpha = \max_U \frac{\partial F}{\partial U} \quad (4.19)$$

In this expression, the right-hand-side is an approximation for flux on the face $i + 1/2$, while $U_{i+1/2}^-$ and $U_{i+1/2}^+$ are the WENO reconstructed variables on each side of the face $i + 1/2$ (see Appendix B for further details). The first term on the RHS is an approximation for $F_{i+1/2}$, while the second term represents the artificial diffusion. In the proposed code implementation, eq. (4.9) is retained for the approximation of $F_{i+1/2}$ in all the domain, while only taking into account the dissipative term of eq. (4.18), where instead of taking the maximum overall U_i , the maximum between cells $(i, i + 1)$ is used to decrease artificial dissipation (local Lax-Friedrichs Scheme). In regions that exhibits shocks, the following expression is used:

$$F(U(x_{i+1/2}, t)) \simeq \frac{F(U_i, t) + F(U_{i+1}, t)}{2} + F_{i+1/2}^{d,WENO} \quad (4.20)$$

$$F_{i+1/2}^{d,WENO} = -\frac{\alpha}{2}(U_{i+1/2}^+ - U_{i+1/2}^-), \quad \alpha = \max_{(U_i, U_{i+1})} \frac{\partial F}{\partial U} \quad (4.21)$$

The order of the Weighted-Essentially Non Oscillatory (WENO) reconstruction may be decided as input parameter. The treatment of the artificial diffusion term on the one-dimensional model problem equation is exported in the one-dimensional equations system by diagonalizing the problem. To achieve the diagonal form of the system, we use a property of the Eulerian flux to be a homogeneous function of degree one in \mathbf{U} , as such, we can express $\mathbf{F}' = \mathbf{A}'\mathbf{U}$ [142, 143], where $\mathbf{A}' = \partial\mathbf{F}'/\partial\mathbf{U}$. In particular, to retrieve the numerical diffusion term, the problem is linearized around face $i + 1/2$, obtaining the linear flux

$$\mathbf{F}' \simeq \mathbf{A}'_{i+1/2}\mathbf{U} \quad (4.22)$$

which can be diagonalized² introducing the matrix $\mathbf{L}'_{i+1/2}$ of the normalized left eigenvectors of \mathbf{A}' and the matrix $\mathbf{R}'_{i+1/2} = \mathbf{L}'_{i+1/2}^{-1}$ of the normalized right eigenvectors

$$\mathbf{F}' \simeq \mathbf{R}'_{i+1/2} \Lambda'_{i+1/2} \mathbf{L}'_{i+1/2} \mathbf{U} \quad (4.23)$$

where $\Lambda'_{i+1/2}$ is the diagonal matrix of the eigenvalues. By pre-multiplying for $\mathbf{L}'_{i+1/2}$ it is possible to obtain

$$(\mathbf{L}'_{i+1/2} \mathbf{F}') \simeq \Lambda'_{i+1/2} (\mathbf{L}'_{i+1/2} \mathbf{U}) \quad (4.24)$$

It is easy to apply the flux (4.21) to this form

$$(\mathbf{L}'_{i+1/2} \mathbf{F}'^{d,WENO}) = -\frac{1}{2} \Lambda'_{max} (\mathbf{L}'_{i+1/2} \mathbf{U}_{i+1/2}^+ - \mathbf{L}'_{i+1/2} \mathbf{U}_{i+1/2}^-) \quad (4.25)$$

and finally, by pre-multiplying for $\mathbf{R}'_{i+1/2}$ we have

$$\mathbf{F}'^{d,WENO}_{i+1/2} = -\frac{1}{2} \mathbf{R}'_{i+1/2} \Lambda'_{max} \mathbf{L}'_{i+1/2} (\mathbf{U}_{i+1/2}^+ - \mathbf{U}_{i+1/2}^-) \quad (4.26)$$

In this procedure, the symmetry with respect the face $i + 1/2$ has not been broken, thus, the overall second order accuracy for the approximation of the convective fluxes is maintained.

Finally, a proper definition of an intermediate state for matrices in $i + 1/2$ is needed. Common choices are the Roe's state [144] between $(i, i+1)$, or, for a less diffusive scheme, Roe's state between $(i + 1/2^-, i + 1/2^+)$, such that the final form of the WENO dissipative fluxes is

$$\mathbf{F}'^{d,WENO}_{i+1/2} = -\frac{1}{2} \mathbf{R}'_{i+1/2} \Lambda'_{max} \mathbf{L}'_{i+1/2} (\mathbf{U}_{i+1/2}^+ - \mathbf{U}_{i+1/2}^-) \quad (4.27)$$

$$\mathbf{R}'_{i+1/2}, \mathbf{L}'_{i+1/2} \text{ evaluated in Roe's state between } (i, i+1) \text{ or } (i + 1/2^\pm) \quad (4.28)$$

$$\Lambda'_{max} = \text{diag}(\Lambda'_l), \quad \Lambda'_l = \max_{i,i+1} \lambda'_l, \quad \lambda'_l \text{ eigenvalue of } \frac{\partial \mathbf{F}'}{\partial \mathbf{U}} \quad (4.29)$$

$$\mathbf{U}_{i-1/2}^+, \mathbf{U}_{i-1/2}^- \text{ right and left WENO reconstructed variables} \quad (4.30)$$

²It can be diagonalized since the Euler system of equations is an hyperbolic system.

4.4 Viscous fluxes

In Sec. 4.3 an expression for the artificial diffusion term was derived. Here, the discretization procedure for the physical ones is provided. Recalling eq. (2.15), \mathbf{G}'_f is an approximation for

$$\begin{aligned} \mathbf{G}_j n_j &= \sqrt{\gamma} \frac{M_\infty}{Re_c} \left\{ \begin{array}{l} 0 \\ \mu \frac{\partial u_i}{\partial n} \\ \frac{1}{Pr} \frac{\gamma}{\gamma - 1} K \frac{\partial T}{\partial n} \end{array} \right\} + \\ &+ \sqrt{\gamma} \frac{M_\infty}{Re_c} \left\{ \begin{array}{l} 0 \\ \mu \frac{\partial u_j}{\partial x_i} n_j - \frac{2}{3} \mu \frac{\partial u_k}{\partial x_k} n_i \\ \mu u_i \frac{\partial u_i}{\partial n} + \mu u_i \frac{\partial u_j}{\partial x_i} n_j - \frac{2}{3} \mu \frac{\partial u_k}{\partial x_k} u_n \end{array} \right\} \end{aligned} \quad (4.31)$$

The normal derivatives in eq. (4.31) are computed applying second order accurate Finite Differ-

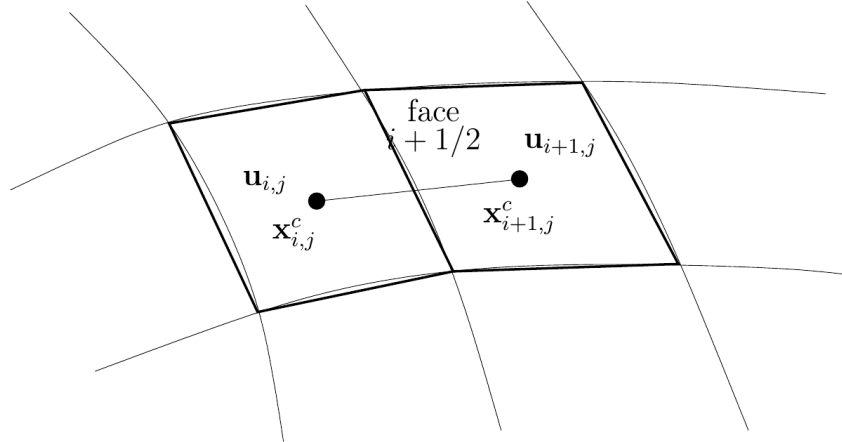


Figure 4.4: Schematic of the grid cells involved in the evaluation of $\partial\varphi/\partial n$ appearing in the viscous fluxes on face $i + 1/2$.

ences. For example, referring to Fig. 4.4, the term contributing to the momentum equations can be expresses as

$$\mu \frac{\partial u_i}{\partial n} \Big|_f \simeq \bar{\mu}_{i+1/2,j,k} \frac{u_{i+1,j,k} - u_{i,j,k}}{|\mathbf{x}_{i+1,j,k}^c - \mathbf{x}_{i,j,k}^c|} \quad (4.32)$$

The other derivatives appearing in the second row of eq. (4.31) are first computed at each cell center by the gradient theorem

$$\frac{\partial \varphi}{\partial x_i} := \frac{1}{V} \int_V \frac{\partial \varphi}{\partial x_i} dV = \frac{1}{V} \oint_{\partial V} \varphi n_i dS \quad (4.33)$$

where the value of φ on faces is taken as the average between adjacent cells in order to maintain second order accuracy. The obtained gradients refers to the cell-centroids. The values on the faces needed in eq.(4.31), are again calculated by considering the average values between adjacent cells.

4.5 Runge-Kutta time-integration

With the previous steps, we defined a set of Ordinary Differential Equations (ODE) of the kind $d\mathbf{U}_{i,j,k}/dt = \mathbf{RHS}$, which can be efficiently solved with a Runge-Kutta time-integration algorithm. In this dissertation, unless otherwise stated, a three stages Runge-Kutta algorithm will be used (see Appendix B). Referring to Orlandi [145], the algorithm can be explained by considering separately linear and non-linear terms that appear in the semi-discrete system of equations

$$\frac{\partial \mathbf{U}_i}{\partial t} = [\mathbf{N}(\mathbf{U})]_i + (\mathbf{L}\mathbf{U})_i \quad (4.34)$$

In this expression, \mathbf{N} refers to the non-linear terms, while \mathbf{L} contains the linear terms that are treated with an implicit approach, which is used to increase the stability of the scheme. Denoting with superscripts n and $n+1$ the discretized times, and with superscripts L_1 , L_2 the intermediate Runge-Kutta stages, we have

$$\mathbf{U}_i^{L_1} = \mathbf{U}_i^n + \gamma_1 \Delta t \mathbf{N}_i^n + \rho_1 \Delta t \mathbf{N}_i^{-L_2} + \alpha_1 \Delta t [\theta(\mathbf{L}\mathbf{U})_i^{L_1} + (1-\theta)(\mathbf{L}\mathbf{U})_i^n] \quad (4.35a)$$

$$\mathbf{U}_i^{L_2} = \mathbf{U}_i^{L_1} + \gamma_2 \Delta t \mathbf{N}_i^{L_1} + \rho_2 \Delta t \mathbf{N}_i^n + \alpha_2 \Delta t [\theta(\mathbf{L}\mathbf{U})_i^{L_2} + (1-\theta)(\mathbf{L}\mathbf{U})_i^{L_1}] \quad (4.35b)$$

$$\mathbf{U}_i^{n+1} = \mathbf{U}_i^{L_2} + \gamma_3 \Delta t \mathbf{N}_i^{L_2} + \rho_3 \Delta t \mathbf{N}_i^{L_1} + \alpha_3 \Delta t [\theta(\mathbf{L}\mathbf{U})_i^{n+1} + (1-\theta)(\mathbf{L}\mathbf{U})_i^{L_2}] \quad (4.35c)$$

where Δt is the discretized time interval $\Delta t = t^{n+1} - t^n$, the superscript $-L_2$ denotes the equivalent of L_2 but at time level $n-1$ and

$$\begin{aligned} \gamma_1 &= 8/15, & \gamma_2 &= 5/12, & \gamma_3 &= 3/4, \\ \rho_1 &= 0, & \rho_2 &= -17/60, & \rho_3 &= -5/12, \\ \alpha_i &= \rho_i + \gamma_i, & \theta &= \begin{cases} 1 & \text{Implicit Euler} \\ 1/2 & \text{Crank-Nicolson} \end{cases} \end{aligned} \quad (4.36)$$

Each sub-equation of eq. (4.35) is a time integration on a fractional step $\alpha_i \Delta t$, as can be easily seen by expanding in Taylor series for example the terms of (4.35a) around time level n . As already pointed out, the \mathbf{L} terms are treated implicitly by using an Implicit Euler integration ($\theta = 1$, first order) or a Crank-Nicolson one ($\theta = 1/2$, second order). Each sub-equation of eq. (4.35) may be also recast in the so-called *delta form*, as

$$(\mathbf{U}_i^{L_1} - \mathbf{U}_i^n) = \gamma_1 \Delta t \mathbf{N}_i^n + \rho_1 \Delta t \mathbf{N}_i^{-L_2} + \alpha_1 \Delta t (\mathbf{L}\mathbf{U})_i^n + \alpha_1 \theta \Delta t [(\mathbf{L}\mathbf{U})_i^{L_1} - (\mathbf{L}\mathbf{U})_i^n] \quad (4.37a)$$

$$(\mathbf{U}_i^{L_2} - \mathbf{U}_i^{L_1}) = \gamma_2 \Delta t \mathbf{N}_i^{L_1} + \rho_2 \Delta t \mathbf{N}_i^n + \alpha_2 \Delta t (\mathbf{L}\mathbf{U})_i^{L_1} + \alpha_2 \theta \Delta t [(\mathbf{L}\mathbf{U})_i^{L_2} - (\mathbf{L}\mathbf{U})_i^{L_1}] \quad (4.37b)$$

$$(\mathbf{U}_i^{n+1} - \mathbf{U}_i^{L_2}) = \gamma_3 \Delta t \mathbf{N}_i^{L_2} + \rho_3 \Delta t \mathbf{N}_i^{L_1} + \alpha_3 \Delta t (\mathbf{L}\mathbf{U})_i^{L_2} + \alpha_3 \theta \Delta t [(\mathbf{L}\mathbf{U})_i^{n+1} - (\mathbf{L}\mathbf{U})_i^{L_2}] \quad (4.37c)$$

so that the choice of the implicit integration method between Implicit Euler and Crank-Nicolson only affects a coefficient of the terms that remain on the left-hand side during the solving procedure. However, it is worth to remark that when the computations are not fully explicit, the order of the time integration is the same of the implicit scheme, and the Runge-Kutta third order is used only for fully explicit computations. Nevertheless, the latter remains a convenient approach for the enhanced stability that is achieved. Another advantage of this approach is that the coefficient $\rho_1 = 0$, since in this way no information from previous steps is required for the time integration from time level n to time level $n+1$.

4.6 Implicit treatment of j fluxes

In the description of the Runge-Kutta algorithm the terms \mathbf{N} and \mathbf{L} were not properly defined. For reference purposes, lets recall for example eq. (4.37c)

$$(\mathbf{U}_i^{n+1} - \mathbf{U}_i^{L_2}) = \gamma_3 \Delta t \mathbf{N}_i^{L_2} + \rho_3 \Delta t \mathbf{N}_i^{L_1} + \alpha_3 \Delta t (\mathbf{L}\mathbf{U})_i^{L_2} + \alpha_3 \theta \Delta t [(\mathbf{L}\mathbf{U})_i^{n+1} - (\mathbf{L}\mathbf{U})_i^{L_2}]$$

When run in fully-explicit mode, then $\mathbf{L} = 0$ (representative of the linear terms to be treated implicitly) and \mathbf{N} is given by taking into account all the previous spatial discretized terms. It is useful to rewrite the expression with all the previous discretized terms, remembering that overbars denote arithmetic averages and the prime retains information about the orientation of the surface

$$\frac{d\mathbf{U}_{i,j}}{dt} = \mathbf{RHS}_{i,j} = \mathbf{N}_{i,j} \Rightarrow \quad (4.38)$$

$$\begin{aligned} \Rightarrow \quad \mathbf{N}_{i,j} = & -\frac{1}{V_{i,j}} \left(\mathbf{F}'_{i+1/2,j} S_{i+1/2,j} - \mathbf{F}'_{i-1/2,j} S_{i-1/2,j} \right) + \\ & -\frac{1}{V_{i,j}} \left(\mathbf{F}'_{i,j+1/2} S_{i,j+1/2} - \mathbf{F}'_{i,j-1/2} S_{i,j-1/2} \right) + \\ & + \frac{1}{V_{i,j}} \left(\mathbf{G}'_{i+1/2,j} S_{i+1/2,j} - \mathbf{G}'_{i-1/2,j} S_{i-1/2,j} \right) + \\ & + \frac{1}{V_{i,j}} \left(\mathbf{G}'_{i,j+1/2} S_{i,j+1/2} - \mathbf{G}'_{i,j-1/2} S_{i,j-1/2} \right) \end{aligned} \quad (4.39)$$

$$\begin{aligned} \mathbf{F}'_{i+1/2,j} = & \overline{\mathbf{u}'}_{i+1/2,j} \begin{Bmatrix} \bar{\rho}_{i+1/2,j} \\ (\bar{\rho}\mathbf{u})_{i+1/2,j} \\ (\bar{\rho}H)_{i+1/2,j} \end{Bmatrix} + \bar{p}_{i+1/2,j} \begin{Bmatrix} 0 \\ \hat{\mathbf{n}}_{i+1/2,j} \\ 0 \end{Bmatrix} + \\ & + f(\Theta_{i+1/2,j}) \mathbf{F}'^{d,WENO}_{i+1/2,j} \\ f(\Theta_{i+1/2,j}) = & \begin{cases} 0 & \text{for } \Theta_{i+1/2,j} < \bar{\Theta} \\ 1 & \text{for } \Theta_{i+1/2,j} \geq \bar{\Theta} \end{cases} \quad (4.40) \\ \mathbf{F}'^{d,WENO}_{i+1/2} = & -\frac{1}{2} \mathbf{R}'_{i+1/2} \Lambda'_{i,i+1} \mathbf{L}'_{i+1/2} \left(\mathbf{U}_{i+1/2}^+ - \mathbf{U}_{i+1/2}^- \right) \end{aligned}$$

$\mathbf{F}'_{i,j+1/2}$ obtained by considering increments on j rather than i

$$\begin{aligned}
 \mathbf{G}'_{i+1/2,j} &= \mathbf{G}'^1_{i+1/2,j} + \mathbf{G}'^2_{i+1/2,j} + \mathbf{G}'^3_{i+1/2,j} \\
 \mathbf{G}'^1_{i+1/2,j} &= \sqrt{\gamma} \frac{M_\infty}{Re_c} \left\{ \begin{array}{l} 0 \\ \bar{\mu}_{i+1/2,j} \frac{\mathbf{u}_{i+1,j} - \mathbf{u}_{i,j}}{|\mathbf{x}_{i+1,j}^c - \mathbf{x}_{i,j}^c|} \\ \frac{1}{Pr} \frac{\gamma}{\gamma-1} \bar{K}_{i+1/2,j} \frac{T_{i+1,j} - T_{i+1,j}}{|\mathbf{x}_{i+1,j}^c - \mathbf{x}_{i,j}^c|} \end{array} \right\} \\
 \mathbf{G}'^2_{i+1/2,j} &= \sqrt{\gamma} \frac{M_\infty}{Re_c} \left\{ \begin{array}{l} 0 \\ \bar{\mu}_{i+1/2,j} \overline{\left(\frac{\partial \mathbf{u}}{\partial x_i} \right)}_{i+1/2,j} \cdot \hat{\mathbf{n}}_{i+1/2,j} \\ \bar{\mu}_{i+1/2,j} \mathbf{u} \cdot \frac{\mathbf{u}_{i+1} - \mathbf{u}_i}{|\mathbf{x}_{i+1,j}^c - \mathbf{x}_{i,j}^c|} + \bar{\mu}_{i+1/2,j} \overline{(u_i)}_{i+1/2,j} \overline{\left(\frac{\partial \mathbf{u}}{\partial x_i} \right)}_{i+1/2,j} \cdot \hat{\mathbf{n}}_{i+1/2,j} \end{array} \right\} \\
 \mathbf{G}'^3_{i+1/2,j} &= \sqrt{\gamma} \frac{M_\infty}{Re_c} \left\{ \begin{array}{l} 0 \\ -\frac{2}{3} \bar{\mu}_{i+1/2,j} \overline{\left(\frac{\partial u_k}{\partial x_k} \right)}_{i+1/2,j} \hat{\mathbf{n}}_{i+1/2,j} \\ -\frac{2}{3} \bar{\mu}_{i+1/2,j} \overline{\left(\frac{\partial u_k}{\partial x_k} \right)}_{i+1/2,j} \overline{u'}_{i+1/2,j} \end{array} \right\}
 \end{aligned} \tag{4.41}$$

$\mathbf{G}'_{i,j+1/2}$ obtained by considering increments on j rather than i

Further definitions can be found in the previous subsections. For fully-explicit computations, \mathbf{N} and \mathbf{L} are well defined, and second order in space and third order in time are achieved. When run in semi-implicit mode, some of the terms including fluxes in the j direction are treated implicitly, both for the convective and the viscous parts. As such, terms that in the explicit part go forming \mathbf{N} , now go form \mathbf{L} , such that

$$\mathbf{N}_{expl}^L = \mathbf{N}_{impl}^L + (\mathbf{L}\mathbf{U})^L \tag{4.42}$$

For what concerns the viscous part, it is already an almost-linear term, thus reducing the complexity of its description.

4.6.1 Semi-implicit treatment of viscous terms

As already stated, the time integration of some of the fluxes in the j direction is treated implicitly. We start by the viscous fluxes, so that from eq. (4.39) and eq. (4.41) we have, in matrix form and only considering \mathbf{G}'^1 ,

$$(\mathbf{L}^\mathbf{v} \mathbf{U})_{i,j} = \frac{1}{V_{i,j}} \left(\mathbf{G}'^1_{i,j+1/2} S_{i,j+1/2} - \mathbf{G}'^1_{i,j-1/2} S_{i,j-1/2} \right) \tag{4.43}$$

$$\mathbf{G}'^1_{i,j+1/2} = \mathbf{A}^\mathbf{v}_{i,j+1/2} (\mathbf{V}_{\mathbf{T},i,j+1} - \mathbf{V}_{\mathbf{T},i,j}), \quad \mathbf{V}_{\mathbf{T},i,j} = \begin{Bmatrix} \rho_{i,j} \\ \mathbf{u}_{i,j} \\ T_{i,j} \end{Bmatrix} \tag{4.44}$$

$$\mathbf{A}^\mathbf{v}_{i,j+1/2} = \sqrt{\gamma} \frac{M_\infty}{Re_c} \begin{bmatrix} 0 & 0 & 0 \\ 0 & \frac{\bar{\mu}_{i,j+1/2}}{|\mathbf{x}_{i+1,j}^c - \mathbf{x}_{i,j}^c|} \mathbf{I} & 0 \\ 0 & 0 & \frac{1}{Pr} \frac{\gamma}{\gamma-1} \frac{\bar{K}_{i,j+1/2}}{|\mathbf{x}_{i+1,j}^c - \mathbf{x}_{i,j}^c|} \end{bmatrix} \tag{4.45}$$

It is worth to notice that we want to obtain the implicit part by solving for the conservative variables \mathbf{U} , while in this formula the primitive variables \mathbf{V}_T are used. In the continuous case, they are linked by the Jacobian matrix $\mathbf{P}_T = (\partial \mathbf{U}) / (\partial \mathbf{V}_T)$. Here the subscript T stands for the fifth component of \mathbf{V}_T being the temperature, to distinguish them from \mathbf{V}_p , \mathbf{P}_p where instead pressure is considered. Considering a similar relation for the discrete case, we have

$$\Delta \mathbf{V}_{T,i,j} = \mathbf{P}_{T,i,j} \Delta \mathbf{U}_{i,j} \quad (4.46)$$

where the Δ refers to temporal variations, for example $\Delta U_{i,j}^{L_2} = (U_{i,j}^{n+1} - U_{i,j}^{L_2})$. Therefore, it is possible to rewrite eq. (4.43) for a $\Delta \mathbf{V}$ as

$$(\mathbf{L}^v \Delta \mathbf{U})_{i,j} = \frac{1}{V_{i,j}} [S_{i,j+1/2} \mathbf{A}^v_{i,j+1/2} (\mathbf{P}_{T,i,j+1} \Delta \mathbf{U}_{i,j+1} - \mathbf{P}_{T,i,j} \Delta \mathbf{U}_{i,j}) + \dots] \quad (4.47)$$

$$- S_{i,j-1/2} \mathbf{A}^v_{i,j-1/2} (\mathbf{P}_{T,i,j} \Delta \mathbf{U}_{i,j} - \mathbf{P}_{T,i,j-1} \Delta \mathbf{U}_{i,j-1}) \quad (4.48)$$

and defining the matrices \mathbf{L}^A , \mathbf{L}^B , \mathbf{L}^C as

$$\mathbf{L}^A_{i,j} = \frac{S_{i,j-1/2}}{V_{i,j}} \mathbf{A}^v_{i,j-1/2} \mathbf{P}_{T,i,j-1}, \quad \mathbf{L}^C_{i,j} = \frac{S_{i,j+1/2}}{V_{i,j}} \mathbf{A}^v_{i,j+1/2} \mathbf{P}_{T,i,j+1} \quad (4.49)$$

$$\mathbf{L}^B_{i,j} = -\frac{1}{V_{i,j}} [S_{i,j+1/2} \mathbf{A}^v_{i,j+1/2} + S_{i,j-1/2} \mathbf{A}^v_{i,j-1/2}] \mathbf{P}_{T,i,j} \quad (4.50)$$

it is possible to obtain

$$(\mathbf{L}^v \mathbf{U})_{i,j} = \mathbf{L}^A_{i,j} \mathbf{U}_{i,j-1} + \mathbf{L}^B_{i,j} \mathbf{U}_{i,j} + \mathbf{L}^C_{i,j} \mathbf{U}_{i,j+1} \quad (4.51)$$

To fix the ideas, let us consider how the equations for the Runge-Kutta time-integration reads when only the viscous j fluxes are to be implicit. We have:

$$\begin{aligned} \mathbf{N}^v_{i,j} = & -\frac{1}{V_{i,j}} \left(\mathbf{F}'_{i+1/2,j} S_{i+1/2,j} - \mathbf{F}'_{i-1/2,j} S_{i-1/2,j} \right) + \\ & -\frac{1}{V_{i,j}} \left(\mathbf{F}'_{i,j+1/2} S_{i,j+1/2} - \mathbf{F}'_{i,j-1/2} S_{i,j-1/2} \right) + \\ & +\frac{1}{V_{i,j}} \left(\mathbf{G}'_{i+1/2,j} S_{i+1/2,j} - \mathbf{G}'_{i-1/2,j} S_{i-1/2,j} \right) + \\ & +\frac{1}{V_{i,j}} \left(\mathbf{G}'^2_{i,j+1/2} S_{i,j+1/2} - \mathbf{G}'^2_{i,j-1/2} S_{i,j-1/2} \right) + \\ & +\frac{1}{V_{i,j}} \left(\mathbf{G}'^3_{i,j+1/2} S_{i,j+1/2} - \mathbf{G}'^3_{i,j-1/2} S_{i,j-1/2} \right) \end{aligned} \quad (4.52)$$

which differs from eq. (4.39) for the absence of the viscous j fluxes \mathbf{G}'^1 . Then we have eq. (4.51), and inserting both in eq. (4.37c) yields, conveniently setting $(\mathbf{U}_{i,j}^{n+1} - \mathbf{U}_{i,j}^{L_2}) =: \Delta \mathbf{U}_{i,j}^{L_2}$

$$\begin{aligned} \Delta \mathbf{U}_{i,j}^{L_2} = & \gamma_3 \Delta t \mathbf{N}^v_{i,j}^{L_2} + \rho_3 \Delta t \mathbf{N}^v_{i,j}^{L_1} + \\ & + \alpha_3 \Delta t \left(\mathbf{L}^A_{i,j} \mathbf{U}_{i,j-1}^{L_2} + \mathbf{L}^B_{i,j} \mathbf{U}_{i,j}^{L_2} + \mathbf{L}^C_{i,j} \mathbf{U}_{i,j+1}^{L_2} \right) + \\ & + \alpha_3 \theta \Delta t \left(\mathbf{L}^A_{i,j} \Delta \mathbf{U}_{i,j-1}^{L_2} + \mathbf{L}^B_{i,j} \Delta \mathbf{U}_{i,j}^{L_2} + \mathbf{L}^C_{i,j} \Delta \mathbf{U}_{i,j+1}^{L_2} \right) \end{aligned} \quad (4.53)$$

The unknowns we have to solve for are the vectors $\Delta \mathbf{U}^{L_2}$, so we can rewrite, in block-matrix form

$$\begin{bmatrix} \ddots & \ddots & \ddots & \ddots & \ddots \\ 0 & -\alpha_3 \theta \Delta t \mathbf{L}^{\mathbf{A}^{L_2}}_{i,j} & \mathbf{I} - \alpha_3 \theta \Delta t \mathbf{L}^{\mathbf{B}^{L_2}}_{i,j} & -\alpha_3 \theta \Delta t \mathbf{L}^{\mathbf{C}^{L_2}}_{i,j} & 0 \\ \ddots & \ddots & \ddots & \ddots & \ddots \end{bmatrix} \begin{Bmatrix} \Delta \mathbf{U}_{i,j-1}^{L_2} \\ \Delta \mathbf{U}_{i,j}^{L_2} \\ \Delta \mathbf{U}_{i,j+1}^{L_2} \\ \vdots \end{Bmatrix} = \begin{Bmatrix} \vdots \\ \mathbf{RHS}_{i,j-1} \\ \mathbf{RHS}_{i,j} \\ \mathbf{RHS}_{i,j+1} \\ \vdots \end{Bmatrix}$$

where at the left-hand-side we have a block-tridiagonal matrix, and $\mathbf{RHS}_{i,j}$ is given by the first two rows at the right-hand-side of eq. (4.53), so the system may be efficiently solved to get the increments $\Delta \mathbf{U}$.

About the linearization procedure, it is important to highlight that the relation of eq. (4.46) introduces an approximation, so that the implicit viscous j fluxes are not exactly equal to the explicit viscous j fluxes. Nevertheless, the use of both does not introduce any inconsistency inside the equations. For convenience we compute the implicit fluxes that appear in \mathbf{RHS}_j in an explicit way. Therefore, we compute at the right-hand side the flux using the primitive variables rather than the conservative ones, which, however, must be used at the left-hand side. It is also important to highlight that, the intrinsic approximation in eq. (4.37), which has been used in eq. (4.53), is that the \mathbf{L} linear terms must be known. In this way, they can only be evaluated at previous times. These aspects do not affect the order of accuracy of the semi-implicit scheme, which remains one for Implicit Euler ($\theta = 1$) and two for Crank-Nicolson ($\theta = 1/2$).

4.6.2 Semi-implicit treatment of convective terms

As done with the viscous j fluxes, also the convective j fluxes are treated implicitly. Since the convective part is non-linear, before proceeding we need to linearize them. From eq. (4.39) and eq. (4.40), we have

$$(\mathbf{L}^c \mathbf{U})_{i,j} = -\frac{1}{V_{i,j}} (\mathbf{F}'_{i,j+1/2} S_{i,j+1/2} - \mathbf{F}'_{i,j-1/2} S_{i,j-1/2}) \quad (4.54)$$

$$\mathbf{F}'_{i,j+1/2} \simeq \mathbf{F}(\mathbf{U}_{i,j+1/2}) + f(\Theta_{i,j+1/2}) \mathbf{F}'^{d,WENO}_{i,j+1/2} \quad (4.55)$$

where the approximation symbol in eq. (4.55) is due to the fact that the operator is not splitted, as instead done in the explicit part. This is a crucial assumption, since the kinetic energy is no more conserved in the implicit integration. This is not the only approximation, since the main aim is to linearize the equations to solve a block-tridiagonal linear system. Exploiting a property of the Eulerian flux to be a homogeneous function of degree one in \mathbf{U} , as such, we can express $\mathbf{F}' = \mathbf{A}' \mathbf{U}$, i.e. it is possible to move the Jacobian $\mathbf{A}' = (\partial \mathbf{F}' / (\partial \mathbf{U}))$ inside or outside the derivative operator [142, 143]. In particular, it is possible to write

$$\mathbf{F}'_{i,j+1/2} \simeq \mathbf{A}'_{i,j+1/2} \mathbf{U}_{i,j+1/2} + f(\Theta_{i,j+1/2}) \mathbf{F}'^{d,WENO}_{i,j+1/2} \quad (4.56)$$

The artificial diffusion term is complex to linearize. Furthermore, the WENO reconstruction involves a large stencil, so that the resulting system would involve no more the inversion of a block-tridiagonal matrix. As such, the WENO diffusion is replaced with the Lax-Friedrichs one, which is more

dissipative. The local Lax-Friedrichs numerical flux is applied to $\mathbf{A}'\mathbf{U}$ to have only the artificial diffusion fluxes. Matrix $\mathbf{A}'_{i,j+1/2}$ contains information about the wave system on face $j + 1/2$, with waves propagating both on positive and negative direction. The Lax-Friedrichs method consists in splitting the flux to deal separately with waves propagating in positive or in negative direction. First, we deal with the classical scheme applied to the linearized system $\mathbf{F} = \mathbf{A}_{j+1/2}\mathbf{U}$. It is possible to split the flux function as the sum of positive and negative fluxes, defined as follows

$$\begin{aligned}\mathbf{A}_{j+1/2}\mathbf{U} &= \mathbf{A}_{j+1/2}^+\mathbf{U} + \mathbf{A}_{j+1/2}^-\mathbf{U} \\ \mathbf{A}_{j+1/2}^\pm &= \frac{1}{2} \left(\mathbf{A}_{j+1/2} \pm \mathbf{A}_{j,j+1} \right) \\ \mathbf{A}_{j,j+1} &= \mathbf{R}_{j+1/2} \mathbf{\Lambda}_{j,j+1} \mathbf{L}_{j+1/2}\end{aligned}\quad (4.57)$$

With the above splitting, matrix $\mathbf{A}_{j+1/2}^+$ describes waves on face $j + 1/2$ propagating only in the positive direction, while matrix $\mathbf{A}_{j+1/2}^-$ describes waves on face $j + 1/2$ propagating only in the negative direction. In this way, it is possible to find the exact solution of the linearized problem, since positive waves will convect unchanged \mathbf{U}_j in $j + 1/2$, while negative waves will convect unchanged \mathbf{U}_{j+1} in $j + 1/2$. Therefore,

$$\begin{aligned}\mathbf{F}_{j+1/2} &= \mathbf{A}_{j+1/2}^+\mathbf{U}_j + \mathbf{A}_{j+1/2}^-\mathbf{U}_{j+1} = \\ &= \frac{1}{2} \left(\mathbf{A}_{j+1/2} + \mathbf{A}_{j,j+1} \right) \mathbf{U}_j + \frac{1}{2} \left(\mathbf{A}_{j+1/2} - \mathbf{A}_{j,j+1} \right) \mathbf{U}_{j+1} = \\ &= \mathbf{A}_{j+1/2} \bar{\mathbf{U}}_{j+1/2} - \frac{1}{2} \mathbf{A}_{j,j+1} (\mathbf{U}_{j+1} - \mathbf{U}_j)\end{aligned}\quad (4.58)$$

that can be written as

$$\mathbf{F}_{j+1/2} = \mathbf{A}_{j+1/2} \bar{\mathbf{U}}_{j+1/2} + \mathbf{F}_{j+1/2}^{d,LF}, \quad \mathbf{F}_{j+1/2}^{d,LF} = -\frac{1}{2} \mathbf{A}_{j,j+1} (\mathbf{U}_{j+1} - \mathbf{U}_j) \quad (4.59)$$

A common choice is to define the matrix $\mathbf{A}_{j+1/2}$ in Roe's intermediate state between j and $j + 1$. Substituting the Lax-Friedrichs dissipation (right equation of eq. (4.59)) to the WENO one in eq. (4.56), and identifying also $\mathbf{U}_{i,j+1/2}$ as $\bar{\mathbf{U}}_{i,j+1/2}$ (left equation of eq. (4.59)), one can obtain

$$\mathbf{F}_{i,j+1/2}^{impl} = \frac{1}{2} \mathbf{A}'_{i,j+1/2} (\mathbf{U}_{i,j+1} + \mathbf{U}_{i,j}) - f(\Theta_{i,j+1/2}) \frac{1}{2} \mathbf{A}'_{j,j+1} (\mathbf{U}_{i,j+1} - \mathbf{U}_{i,j}) \quad (4.60)$$

so defining

$$\mathbf{A}'_{i,j+1/2}^\pm := \frac{1}{2} \left(\mathbf{A}'_{i,j+1/2} \pm f(\Theta_{i,j+1/2}) \mathbf{A}'_{j,j+1} \right) \quad (4.61)$$

it is possible to obtain

$$\mathbf{F}_{i,j+1/2}^{impl} = \mathbf{A}'_{i,j+1/2}^+ \mathbf{U}_{i,j} + \mathbf{A}'_{i,j+1/2}^- \mathbf{U}_{i,j+1} \quad (4.62)$$

and substituting in eq. (4.54)

$$(\mathbf{L}^c \mathbf{U})_{i,j} = -\frac{1}{V_{i,j}} \left[S_{i,j+1/2} \left(\mathbf{A}'^+_{i,j+1/2} \mathbf{U}_{i,j} + \mathbf{A}'^-_{i,j+1/2} \mathbf{U}_{i,j+1} \right) + S_{i,j-1/2} \left(\mathbf{A}'^+_{i,j-1/2} \mathbf{U}_{i,j-1} + \mathbf{A}'^-_{i,j-1/2} \mathbf{U}_{i,j} \right) \right] \quad (4.63)$$

As done when dealing with the viscous fluxes, also here the matrices \mathbf{L}^D , \mathbf{L}^E and \mathbf{L}^F are defined as

$$\mathbf{L}^D_{i,j} = \frac{S_{i,j-1/2}}{V_{i,j}} \mathbf{A}'^+_{i,j-1/2}, \quad \mathbf{L}^F_{i,j} = -\frac{S_{i,j+1/2}}{V_{i,j}} \mathbf{A}'^-_{i,j+1/2} \quad (4.64)$$

$$\mathbf{L}^E_{i,j} = -\frac{1}{V_{i,j}} \left[S_{i,j+1/2} \mathbf{A}'^+_{i,j+1/2} - S_{i,j-1/2} \mathbf{A}'^-_{i,j-1/2} \right] \quad (4.65)$$

The matrices \mathbf{L}^D , \mathbf{L}^E , \mathbf{L}^F , are the analogous of, respectively, \mathbf{L}^A , \mathbf{L}^B , \mathbf{L}^C for the viscous fluxes, so that an analogous block-tridiagonal system can be defined. As stressed out at the end of the previous subsection, all the manipulations to fluxes, for convenience, are used just on terms that go at the left-hand side of the system, while terms appearing at the right-hand side are treated as in the explicit part of the code. For the sake of clarity, at the right-hand side, the WENO dissipative fluxes is used also in the j direction, while on the left-hand side the Lax-Friedrichs one is used instead.

4.6.3 Final semi-implicit scheme

The union of the two previous results gives the time increment at each l -th stage of the Runge-Kutta algorithm by solving the block-tridiagonal system:

$$\begin{bmatrix} & & \\ & \ddots & & \\ & & \ddots & & \\ -\alpha_l \theta \Delta t (\mathbf{L}^A_{i,j} + \mathbf{L}^D_{i,j}) & \mathbf{I} - \alpha_l \theta \Delta t (\mathbf{L}^B_{i,j} + \mathbf{L}^E_{i,j}) & -\alpha_l \theta \Delta t (\mathbf{L}^C_{i,j} + \mathbf{L}^F_{i,j}) & & \\ & & & \ddots & \\ & & & & \ddots \end{bmatrix} \begin{pmatrix} \Delta \mathbf{U}_{i,j-1}^l \\ \Delta \mathbf{U}_{i,j}^l \\ \Delta \mathbf{U}_{i,j+1}^l \\ \vdots \end{pmatrix} = \begin{pmatrix} \mathbf{RHS}_{i,j-1}^l \\ \mathbf{RHS}_{i,j}^l \\ \mathbf{RHS}_{i,j+1}^l \\ \vdots \end{pmatrix}$$

with matrices \mathbf{L}^A , \mathbf{L}^B , \mathbf{L}^C , \mathbf{L}^D , \mathbf{L}^E , \mathbf{L}^F defined in eq. (4.49), eq. (4.50), eq. (4.64), eq. (4.65),

$$\begin{aligned} \mathbf{RHS}_{i,j}^l &= \gamma_l \Delta t \mathbf{N}_{i,j}^l + \rho_l \Delta t \mathbf{N}_{i,j}^{l-1} + \alpha_l \Delta t \mathbf{L}^E_{i,j} \\ \mathbf{N}_{i,j} &= -\frac{1}{V_{i,j}} \left(\mathbf{F}'_{i+1/2,j} S_{i+1/2,j} - \mathbf{F}'_{i-1/2,j} S_{i-1/2,j} \right) + \\ &\quad + \frac{1}{V_{i,j}} \left(\mathbf{G}'_{i+1/2,j} S_{i+1/2,j} - \mathbf{G}'_{i-1/2,j} S_{i-1/2,j} \right) + \\ &\quad + \frac{1}{V_{i,j}} \left(\mathbf{G}'^2_{i,j+1/2} S_{i,j+1/2} - \mathbf{G}'^2_{i,j-1/2} S_{i,j-1/2} \right) + \\ &\quad + \frac{1}{V_{i,j}} \left(\mathbf{G}'^3_{i,j+1/2} S_{i,j+1/2} - \mathbf{G}'^3_{i,j-1/2} S_{i,j-1/2} \right) \\ \mathbf{L}^E_{i,j} &= -\frac{1}{V_{i,j}} \left(\mathbf{F}'_{i,j+1/2} S_{i,j+1/2} - \mathbf{F}'_{i,j-1/2} S_{i,j-1/2} \right) + \\ &\quad + \frac{1}{V_{i,j}} \left(\mathbf{G}'^1_{i,j+1/2} S_{i,j+1/2} - \mathbf{G}'^1_{i,j-1/2} S_{i,j-1/2} \right) \end{aligned}$$

and

$$\begin{aligned}\mathbf{F}'_{i+1/2,j} &= \bar{u}'_{i+1/2,j} \begin{Bmatrix} \bar{\rho}_{i+1/2,j} \\ \frac{(\bar{\rho}\mathbf{u})_{i+1/2,j}}{(\bar{\rho}H)_{i+1/2,j}} \end{Bmatrix} + \bar{p}_{i+1/2,j} \begin{Bmatrix} 0 \\ \hat{\mathbf{n}}_{i+1/2,j} \end{Bmatrix} + \\ &\quad + f(\Theta_{i+1/2,j}) \mathbf{F}'^{d,WENO}_{i+1/2,j} \\ f(\Theta_{i+1/2,j}) &= \begin{cases} 0 & \text{for } \Theta_{i+1/2,j} < \bar{\Theta} \\ 1 & \text{for } \Theta_{i+1/2,j} \geq \bar{\Theta} \end{cases} \\ \mathbf{F}'^{d,WENO}_{i+1/2} &= -\frac{1}{2} \mathbf{R}'_{i+1/2} \Lambda'_{i,i+1} \mathbf{L}'_{i+1/2} \left(\mathbf{U}_{i+1/2}^+ - \mathbf{U}_{i+1/2}^- \right) \\ \mathbf{F}'_{i,j+1/2} & \text{ obtained by considering increments on } j \text{ rather than } i\end{aligned}$$

$$\begin{aligned}\mathbf{G}'_{i+1/2,j} &= \mathbf{G}'^1_{i+1/2,j} + \mathbf{G}'^2_{i+1/2,j} + \mathbf{G}'^3_{i+1/2,j} \\ \mathbf{G}'^1_{i+1/2,j} &= \sqrt{\gamma} \frac{M_\infty}{Re_c} \begin{Bmatrix} 0 \\ \bar{\mu}_{i+1/2,j} \frac{\mathbf{u}_{i+1,j} - \mathbf{u}_{i,j}}{|\mathbf{x}_{i+1,j}^c - \mathbf{x}_{i,j}^c|} \\ \frac{1}{Pr} \frac{\gamma}{\gamma - 1} \bar{K}_{i+1/2,j} \frac{T_{i+1,j} - T_{i+1,j}}{|\mathbf{x}_{i+1,j}^c - \mathbf{x}_{i,j}^c|} \end{Bmatrix} \\ \mathbf{G}'^2_{i+1/2,j} &= \sqrt{\gamma} \frac{M_\infty}{Re_c} \begin{Bmatrix} 0 \\ \bar{\mu}_{i+1/2,j} \left(\frac{\partial \mathbf{u}}{\partial x_i} \right)_{i+1/2,j} \cdot \hat{\mathbf{n}}_{i+1/2,j} \\ \bar{\mu}_{i+1/2,j} \mathbf{u} \cdot \frac{\mathbf{u}_{i+1} - \mathbf{u}_i}{|\mathbf{x}_{i+1,j}^c - \mathbf{x}_{i,j}^c|} + \bar{\mu}_{i+1/2,j} \overline{(u_i)}_{i+1/2,j} \left(\frac{\partial \mathbf{u}}{\partial x_i} \right)_{i+1/2,j} \cdot \hat{\mathbf{n}}_{i+1/2,j} \end{Bmatrix} \\ \mathbf{G}'^3_{i+1/2,j} &= \sqrt{\gamma} \frac{M_\infty}{Re_c} \begin{Bmatrix} 0 \\ -\frac{2}{3} \bar{\mu}_{i+1/2,j} \left(\frac{\partial u_k}{\partial x_k} \right)_{i+1/2,j} \hat{\mathbf{n}}_{i+1/2,j} \\ -\frac{2}{3} \bar{\mu}_{i+1/2,j} \left(\frac{\partial u_k}{\partial x_k} \right)_{i+1/2,j} \overline{u'}_{i+1/2,j} \end{Bmatrix} \\ \mathbf{G}'_{i,j+1/2} & \text{ obtained by considering increments on } j \text{ rather than } i\end{aligned}$$

The resulting order of accuracy in time is lowered to first order when Implicit Euler integration ($\theta = 1$) is used, to second order when Crank-Nicolson ($\theta = 1/2$) is used. The third order is recovered only for explicit calculations.

4.7 Numerical boundary conditions

In the Finite Volume approach, boundary conditions enter the domain only in the evaluation of fluxes near the boundary. A major problem in the enforcement of correct boundary conditions is due to the fact that the computational domain is bounded, while some of the conditions are known at infinity. For this reason, the enforcement of free-stream conditions on the bounded domain may cause spurious wave reflections, which may also lead to instability. A classic way to deal with this problem is to apply non-reflective boundary conditions [146], which on each boundary face linearizes the problem in the normal direction. The resulting system of equations is then cast in characteristic variables, which diagonalize the problem. As a result, one obtains a system of equations, with each equation describing a linear convection problem. One can then identify waves entering and leaving

the domain, and enforce the correct boundary conditions to avoid, or at least minimize, numerical reflection. This approach remains an approximation but guarantees good accuracy and stability. However, the FV approach appears to be somehow intrinsically non-reflective. Instead of explicitly use the characteristic approach to enforce the boundary conditions, it is possible to exploit the so-called ghost cells approach, in which cells outside the computational domain are introduced and contain the necessary boundary conditions. Using ghost cells has the advantage to let one use the same scheme also on the boundary (i.e. using the same formulas for the evaluation of fluxes also on boundaries). The introduction of ghost cells is also convenient, since they are needed for the parallelization of the code (see Sec. 4.8), on the virtual boundaries which define the mesh part on which a single processor works.

The different sets of boundary conditions used in this dissertation is now described.

Subsonic Inlet Boundary - Far Boundary. The free-stream values are imposed for all the conserved variables. Strictly, this is a supersonic inlet condition, and the resulting mathematical problem is ill-posed, since for subsonic inlet not all the informations travels from the outside to the inside of the domain.

Wall Boundary. It is a reflecting boundary conditions [134]. With this method, the velocity is reflected at the wall, such that the sum of velocity in the ghost cell and in the first inner cell (for fixed i) is zero. With this condition, the non-linear part of the Eulerian fluxes is automatically zero. The other conservative variables are extrapolated at zero order. In particular, for the pressure, this is aligned with the usual boundary layer assumption, while this condition on temperature translates into an adiabatic wall.

Subsonic Outlet Boundary. A zero-order extrapolation is used for all the conservative variables, except for the total energy per unit mass, which is instead computed assuming a pressure equal to the free-stream one. As explained by LeVeque [147], a zero-order extrapolation in the ghost cell of a FV scheme often gives a reasonable set of absorbing boundary conditions. As outlined by Pirozzoli and Colonius [148], the straightforward application of non-reflecting boundary conditions for subsonic outlet may lead to numerical drift, since the free-stream value of pressure is not necessarily preserved. The explicit imposition of the free-stream pressure in our method is a simple fix for this problem.

Setting the values in the ghost cells closes both the explicit and implicit parts of the scheme. The explicit fluxes closure is automatic since the fluxes can be all evaluated without any difference with respect to the inner fluxes. For the implicit part, it is less automatic, but the approach remains still straightforward. Recalling the resulting discrete system

$$\begin{bmatrix} \ddots & & & \\ & \ddots & & \\ & & \ddots & \\ -\alpha_l \theta \Delta t (\mathbf{L}^{\mathbf{A}}_{i,j}^l + \mathbf{L}^{\mathbf{D}}_{i,j}^l) & \mathbf{I} - \alpha_l \theta \Delta t (\mathbf{L}^{\mathbf{B}}_{i,j}^l + \mathbf{L}^{\mathbf{E}}_{i,j}^l) & -\alpha_l \theta \Delta t (\mathbf{L}^{\mathbf{C}}_{i,j}^l + \mathbf{L}^{\mathbf{F}}_{i,j}^l) & \\ & & & \ddots \\ & & & & \ddots \end{bmatrix} \begin{pmatrix} \Delta \mathbf{U}_{i,j-1}^l \\ \Delta \mathbf{U}_{i,j}^l \\ \Delta \mathbf{U}_{i,j+1}^l \\ \vdots \end{pmatrix} = \begin{pmatrix} \mathbf{RHS}_{i,j-1}^l \\ \mathbf{RHS}_{i,j}^l \\ \mathbf{RHS}_{i,j+1}^l \\ \vdots \end{pmatrix}$$

it is necessary to include in the vectors also the component on the ghost cells. For example,

considering the boundary $j = 1$, the resulting first block equation reads

$$\begin{aligned} & -\alpha_l \theta \Delta t \left(\mathbf{L}^{\mathbf{A}}_{i,1}^l + \mathbf{L}^{\mathbf{D}}_{i,1}^l \right) \Delta \mathbf{U}_{i,0}^l + \\ & + \left[\mathbf{I} - \alpha_l \theta \Delta t \left(\mathbf{L}^{\mathbf{B}}_{i,1}^l + \mathbf{L}^{\mathbf{E}}_{i,1}^l \right) \right] \Delta \mathbf{U}_{i,1}^l + \\ & -\alpha_l \theta \Delta t \left(\mathbf{L}^{\mathbf{C}}_{i,1}^l + \mathbf{L}^{\mathbf{F}}_{i,1}^l \right) \Delta \mathbf{U}_{i,2}^l = \mathbf{RHS}_{i,1}^l \end{aligned}$$

where the term $\Delta \mathbf{U}_{i,0}^l$ can be expressed from the boundary conditions, as

$$\Delta \mathbf{U}_{i,0}^l = \mathbf{A}_{BC} \Delta \mathbf{U}_{i,1}^l \quad (4.66)$$

with \mathbf{A}_{BC} readily obtained for the different boundary conditions.

Subsonic Inlet Boundary - Far Boundary.

$$\mathbf{A}_{BC} = \begin{bmatrix} 0 & 0 & 0 \\ 0 & 0 & 0 \\ 0 & 0 & 0 \end{bmatrix} \quad (4.67)$$

since we have steady boundary conditions.

Wall Boundary.

$$\mathbf{A}_{BC} = \begin{bmatrix} 1 & 0 & 0 \\ 0 & -\mathbf{I} & 0 \\ 0 & 0 & 1 \end{bmatrix} \quad (4.68)$$

since we reflect the velocity components.

Subsonic Outlet Boundary. This condition is less immediate, but still straightforward. We have to state this condition in terms of primitive variables, since we extrapolate all variables except pressure, for which we assume the free-stream fixed value.

$$\begin{aligned} \Delta \mathbf{V}_{\mathbf{P}_{i,0}}^l &= \begin{bmatrix} 1 & 0 & 0 \\ 0 & \mathbf{I} & 0 \\ 0 & 0 & 0 \end{bmatrix} \Delta \mathbf{V}_{\mathbf{P}_{i,1}}^l, & \Delta \mathbf{V}_{\mathbf{P}}^l &= \mathbf{P}_{\mathbf{P}} \Delta \mathbf{U}^l, \\ \mathbf{P}_{\mathbf{P}_{i,0}} \Delta \mathbf{U}_{i,0}^l &= \begin{bmatrix} 1 & 0 & 0 \\ 0 & \mathbf{I} & 0 \\ 0 & 0 & 0 \end{bmatrix} \mathbf{P}_{\mathbf{P}_{i,1}} \Delta \mathbf{U}_{i,1}^l, \\ \Delta \mathbf{U}_{i,0}^l &= \mathbf{P}_{\mathbf{P}_{i,0}}^{-1} \begin{bmatrix} 1 & 0 & 0 \\ 0 & \mathbf{I} & 0 \\ 0 & 0 & 0 \end{bmatrix} \mathbf{P}_{\mathbf{P}_{i,1}} \Delta \mathbf{U}_{i,1}^l \end{aligned}$$

Since $\mathbf{P}_{\mathbf{P}}$ (and $\mathbf{P}_{\mathbf{P}}^{-1}$) only depends on ρ and \mathbf{u} , for a subsonic outlet we have $\mathbf{P}_{\mathbf{P}_{i,0}} = \mathbf{P}_{\mathbf{P}_{i,1}}$,

thus obtaining

$$\mathbf{A}_{BC} = \mathbf{P}_{\mathbf{p}_{i,1}}^{-1} \begin{bmatrix} 1 & 0 & 0 \\ 0 & \mathbf{I} & 0 \\ 0 & 0 & 0 \end{bmatrix} \mathbf{P}_{\mathbf{p}_{i,1}} \quad (4.69)$$

We illustrate first the procedure in the case of $j = 1$. Expressing $\Delta \mathbf{U}_{i,0}^l$ as just explained, we obtain the modified first block equation

$$\begin{aligned} & \left[\mathbf{I} - \alpha_l \theta \Delta t \left(\mathbf{L}^{\mathbf{B}}_{i,1}^l + \mathbf{L}^{\mathbf{A}}_{i,1}^l \mathbf{A}_{BC} + \mathbf{L}^{\mathbf{E}}_{i,1}^l + \mathbf{L}^{\mathbf{D}}_{i,1}^l \mathbf{A}_{BC} \right) \right] \Delta \mathbf{U}_{i,1}^l + \\ & \quad - \alpha_l \theta \Delta t \left(\mathbf{L}^{\mathbf{C}}_{i,1}^l + \mathbf{L}^{\mathbf{F}}_{i,1}^l \right) \Delta \mathbf{U}_{i,2}^l = \mathbf{RHS}_{i,1}^l \end{aligned}$$

A similar procedure for $j = N$ yields

$$\begin{aligned} & - \alpha_l \theta \Delta t \left(\mathbf{L}^{\mathbf{A}}_{i,N}^l + \mathbf{L}^{\mathbf{D}}_{i,N}^l \right) \Delta \mathbf{U}_{i,N-1}^l + \\ & + \left[\mathbf{I} - \alpha_l \theta \Delta t \left(\mathbf{L}^{\mathbf{B}}_{i,N}^l + \mathbf{L}^{\mathbf{C}}_{i,N}^l \mathbf{A}_{BC} + \mathbf{L}^{\mathbf{E}}_{i,N}^l + \mathbf{L}^{\mathbf{F}}_{i,N}^l \mathbf{A}_{BC} \right) \right] \Delta \mathbf{U}_{i,N}^l = \mathbf{RHS}_{i,N}^l \end{aligned}$$

Thus we can solve the block-tridiagonal system in the N unknowns $\Delta \mathbf{U}_{i,j}^l$.

The applied boundary conditions do not lower the order of accuracy of the scheme, which results second-order accurate in space and up to third order accurate in time, depending on whether we run explicit or implicit calculations.

4.8 Parallelization

The code is written in Fortran 90, it uses domain decomposition, and it fully exploits the Message Passing Interface (MPI) paradigm for the parallelism. Fortran 90 was released as ISO/IEC standard 1539:1991 in 1991 and an ANSI Standard in 1992. Among the features allowed by Fortran 90, parallelization is particularly important for the used code. “MPI is a message-passing application programmer interface, together with protocol and semantic specifications for how its features must behave in any implementation.” The goals of MPI are high performance, scalability, and portability, and remains the dominant model used in high-performance computing today. Basically, the parallelization has been implemented dividing the numerical domain in a certain number of subdomain, by assigning the solution of the equations in every single block to a single process, which is assigned to a single CPU to have the best (possible) performance.

Chapter 5

ONERA C1xb SRM

In this chapter the results of the Implicit Large Eddy Simulation (ILES) of the flow in a simple solid rocket motor configuration are presented. The specific test case under investigation is the three-dimensional ONERA C1xb SRM, experimentally tested at ONERA and on which several numerical investigation have been carried out in the literature by means of RANS and URANS simulations to predict the occurrence of the coupling between vortex shedding and pressure oscillations, leading to an aeroacoustic feedback loop.

In Sec. 5.1 and Sec. 5.2 of this chapter the test case is described, giving information about the SRM geometry, the computational domain, its discretization, as well as global information about the simulation. Section 5.3 presents the ILES results of the C1xb SRM. In particular, in Sec. 5.3.1 the flowfield characteristics are briefly described. In Sec. 5.3.2 the statistical and the spectral properties of the wall pressure signals are studied in depth through a Fourier analysis in the frequency domain and a space-time correlation analysis. Finally, in Sec. 5.3.3 the aeroacoustic feedback loop is discussed and the acoustic feedback frequency is compared with that predicted by an acoustic feedback model proposed in the literature.

5.1 Test case description

The ONERA C1xb is a simple, laboratory-scale SRM model, whose geometry is represented in Fig. 1.12. It has a length of 0.785 m and is characterized by a downstream end of the grain located in the middle of the chamber, which is a velocity antinode of the first even axial mode. The diameter of the rocket chamber is $d_r = 0.055$ m. This motor was carefully designed to investigate the coupling of periodic vortex shedding and pressure oscillations and various firing tests were performed considering several composite propellants with different mass fractions and particle diameters [15]. The present study considers only single-phase ideal-gas flow computations, whose results can be directly compared with the experimental tests performed with the Butalite propellant, without the addition of alumina particles. This assumption is consistent with previous numerical studies [16, 31], according to which the dominant aspect to be captured in order to describe the pressure-oscillation phenomenon is the hydroacoustic coupling between the instability of mean-shear flow and the acoustic modes of the chamber. It is worth to notice that, given the geometry of the grain, this solid rocket motor is characterized by corner vortex shedding (see Sec. 1.2.2).

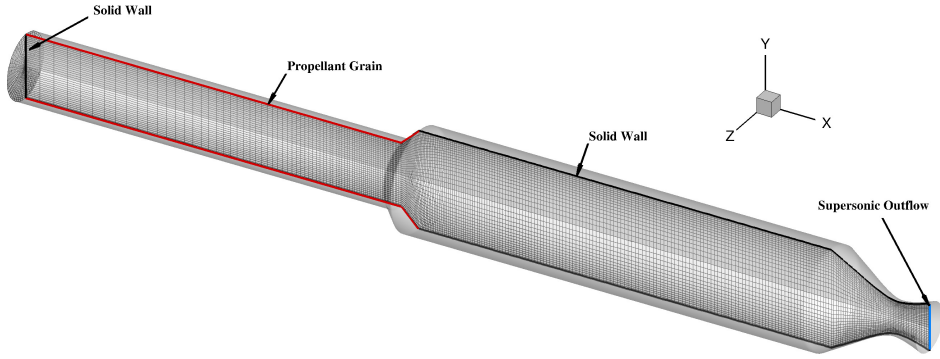


Figure 5.1: Three-dimensional visualization of the computational domain and mesh for the simulation of the C1xb test case. For clarity, only 1 node every 4 is shown in the mesh.

A three-dimensional schematic of the computational domain adopted for the simulation is presented in Fig. 5.1. The domain reproduces the C1xb geometry at a firing time corresponding to a 3 mm grain burned layer, a condition that has been previously considered in many studies [31, 34] and for which several set of data from 2D simulations are available. The igniter presence at the SRM head-end is not considered in the study.

A fully-structured and wall-orthogonal mesh was generated using the conformal mapping algorithm of Driscoll and Vavasis [149], implemented in the open-source tool *gridgen-c*. To select the grid resolution, a preliminary sensitivity study was performed by means of unsteady, axi-symmetric computations. The final mesh, shown in Fig. 5.1, consists of $N_I \cdot N_J \cdot N_K = 1088 \cdot 128 \cdot 192$ cells, for a total number of approximately 26.74 million cells. The grid resolution changes in both the axial and radial direction, whereas it is constant in the azimuthal one, where the spacing is 0.0327 rad. In the first chamber Δx is approximately constant, with $\Delta x = 3.2 \cdot 10^{-3}$ m ($\Delta x/d_r = 0.058$). Starting from the grain edge, to better capture the vortex shedding and the shear-layer evolution, the resolution is increased in the second chamber, where $\Delta x = 7.8 \cdot 10^{-4}$ m ($\Delta x/d_r = 0.014$). In the radial direction Δy varies with a hyperbolic tangent function from an average value $\Delta y = 4.5 \cdot 10^{-4}$ m ($\Delta y/d_r = 0.0082$) at the motor axis up to an average wall spacing $\Delta y = 1.5 \cdot 10^{-4}$ m ($\Delta y/d_r = 0.0027$).

The physical values used for the ONERA C1xb on its 3 mm burned configuration are reported in Table 5.1, where ρ_p is the propellant density, V_c is the propellant burning rate, \dot{m} is the injection mass flow rate, T_f is the flame temperature, c is the speed of sound, R is the perfect gas constant, μ is the dynamic viscosity, γ is the ratio of specific heats, and Pr is the Prandtl number.

ρ_p (kg/m ³)	V_c (m/s)	\dot{m} (kg/s/m ²)	T_f (K)	c (m/s)	R (J/kg/K)	μ (kg/m/s)	γ	Pr
1586	$4.18 \cdot 10^{-3}$	6.62948	2224	1031	384.513	$7 \cdot 10^{-5}$	1.243	0.495

Table 5.1: Physical values used for the simulation of the ONERA C1xb test case [15].

Concerning the boundary conditions (see also Fig. 5.1), a constant mass flow rate and temperature are imposed at the injecting wall according to Table 5.1, whereas the inert walls are treated as no-slip and adiabatic. We recall that, as common in this type of simulations [31], the grain regression is not taken into account and the geometrical configuration of the SRM is considered fixed during the computation. This assumption is strongly justified by the disparity (at least 3-4 orders

	PC Head	PC 1	PC 2	PC 3	PC 4	PC 5	PC 6	PC Aft
x, (m)	0.0000	0.4000	0.4500	0.5000	0.5500	0.6000	0.6500	0.7205
y, (m)	0.0220	0.0425	0.0425	0.0425	0.0425	0.0425	0.0425	0.0307

Table 5.2: Position along the chamber of the experimental/numerical pressure probes (denoted as PC #).

of magnitude) between the time scales associated to the fluid dynamics and acoustics instabilities and the regression rate of the grain.

First, an axi-symmetric computation is started from rest and, after an initial transient, a statistically steady condition is achieved, with the occurrence of sustained pressure oscillations. The final 2D solution was used to initialize the 3D ILES by means of a full revolution of 360 degrees. It is worth to highlight that a continuous forcing was not used to sustain the transition process of the shear layer. To promote the development of turbulence, random perturbations were only added at the initial time of the 3D simulation to the axial velocity field, with maximum magnitude of 3% of the injection velocity. We point out that the capability of correctly triggering the Kelvin-Helmholtz instability in developing shear layers is one of the major issues in this kind of simulations. According to Shur et al. [131], in all practically meaningful computations, the grids capable of resolving this instability are currently non-affordable. In the present case, we do not use any additional model to enhance the transition of the detached shear layer. In such a way we can estimate the effectiveness of a pure ILES.

The 3D computation was run with a time step $\Delta t = 7.1 \cdot 10^{-8} s$ and a relatively long time span was simulated $T = 0.116 s$, which guarantees coverage of frequencies down to at least $f_{min} \approx 8.62 Hz$. A total of 500 full three-dimensional fields have been collected at time intervals of $5.4 \cdot 10^{-5} s$ for post-processing purposes. Furthermore, samples of the pressure field at the wall have been recorded at shorter time intervals of $3.1 \cdot 10^{-6} s$ to guarantee sufficient resolution for the frequency analysis. Running with 1088 processors of the Tier-0 system Marconi (Cineca Supercomputing facility), the cost of the simulation was approximately 3.5 Mio CPU hours.

5.2 Computational strategy

As already mentioned in Chapter 2, we solve the three-dimensional Navier-Stokes equations for a compressible, viscous, heat-conducting gas

$$\begin{aligned} \frac{\partial \rho}{\partial t} + \frac{\partial(\rho u_j)}{\partial x_j} &= 0, \\ \frac{\partial(\rho u_i)}{\partial t} + \frac{\partial(\rho u_i u_j)}{\partial x_j} + \frac{\partial p}{\partial x_i} - \frac{\partial \tau_{ij}}{\partial x_j} &= 0, \\ \frac{\partial(\rho E)}{\partial t} + \frac{\partial(\rho Eu_j + pu_j)}{\partial x_j} - \frac{\partial(\tau_{ij} u_i - q_j)}{\partial x_j} &= 0, \end{aligned} \quad (5.1)$$

where ρ is the density, u_i is the velocity component in the i -th coordinate direction ($i = 1, 2, 3$), E is the total energy per unit mass, p is the thermodynamic pressure, τ_{ij} and q_j are the viscous stress

tensor and the heat flux vector, defined as

$$\tau_{ij} = 2\rho\nu \left(S_{ij} - \frac{1}{3} S_{kk} \delta_{ij} \right) \quad q_j = -\rho c_p \left(\frac{\nu}{\text{Pr}} \right) \frac{\partial T}{\partial x_j} \quad (5.2)$$

where S_{ij} is the strain-rate tensor, ν the kinematic viscosity, depending on temperature T through Sutherland's law and Pr is the molecular Prandtl number.

The simulations have been carried out by means of the in-house finite-volume flow solver described in Chapter 4, which solves the compressible Navier-Stokes equations on structured grids. The convective terms are discretized using a finite volume Godunov-type method which comprises the approximate Roe Riemann solver and seventh-order Weighted-Essentially Non-Oscillatory (WENO) reconstructions of the cell-face values of the flow variables. The gradients normal to the cell faces needed for the viscous fluxes, are evaluated through second-order central-difference approximations, obtaining compact stencils and avoiding numerical odd-even decoupling phenomena. A low-storage, fourth-order, explicit Runge-Kutta algorithm [150] is used for time advancement of the semi-discretized ODEs' system.

Turbulent flow computations are carried out using the Implicit Large-Eddy Simulation (ILES) approach [151], in which the functional reconstruction of the convective terms is carried out using high-resolution flux-limiting methods [152]. As mentioned in Sec. 3.2.2, ILES provides a promising practical alternative to conventional LES and it does not require additional (turbulence) modeling [119], since the numerical dissipation inherent to the WENO part of the numerical flux can be exploited as a subgrid scale (SGS) model [118]. The accuracy and reliability of the flow solver have been assessed in a series of recent studies dedicated to both ILES and Delayed Detached Eddy Simulations (DDES) of compressible turbulent flows [2, 153].

5.3 Results

5.3.1 Flowfield organization

In this section we provide a brief overview of the flow organization in the ONERA C1xb SRM, based on the analysis of both mean and instantaneous quantities from the ILES computations. Fig. 5.2 shows contours of both the mean axial velocity field and of the mean Mach number in the motor. Statistical averaging was performed over the azimuthal direction and over time, using a total number of 500 three-dimensional flow samples. The flow is injected into the chamber from the burning propellant grain and is characterized by a strong axial inhomogeneity, with a constant acceleration from the closed head end up to the motor nozzle, where supersonic flow conditions are reached. Proceeding in the axial direction in the first chamber, a boundary layer is seen to develop, whose thickness rapidly increases due to the effect of surface injection. The profiles of the axial and radial velocity, extracted at several stations and reported in Fig. 5.3 as a function of the wall-normal direction, are in very good agreement with the asymptotic, laminar Taylor-Culick solution (see Sec. 1.2.1) for axisymmetric flows [11, 154]. It is worth pointing out that previous experimental [155–157] and numerical studies [158] have shown that such laminar solution is extremely robust, and it persists (in the mean) also at high values of the injection and axial-flow Reynolds numbers (Re_s, Re_c),

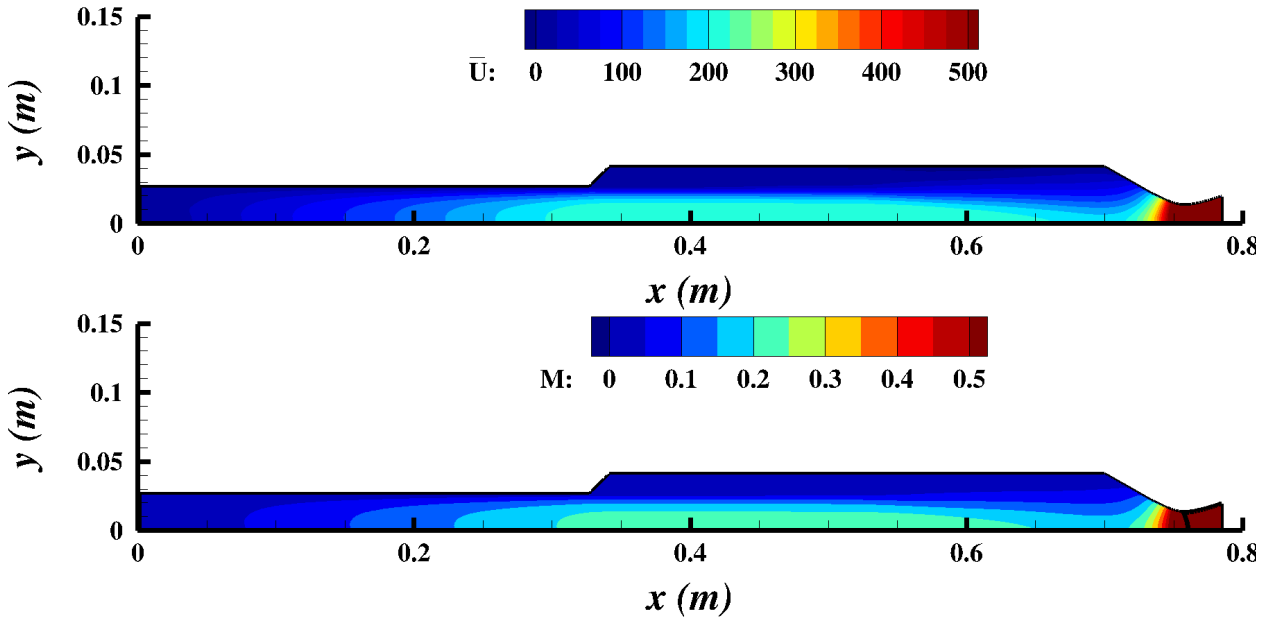


Figure 5.2: Contours of (top) mean axial velocity and (bottom) mean Mach number from ILES

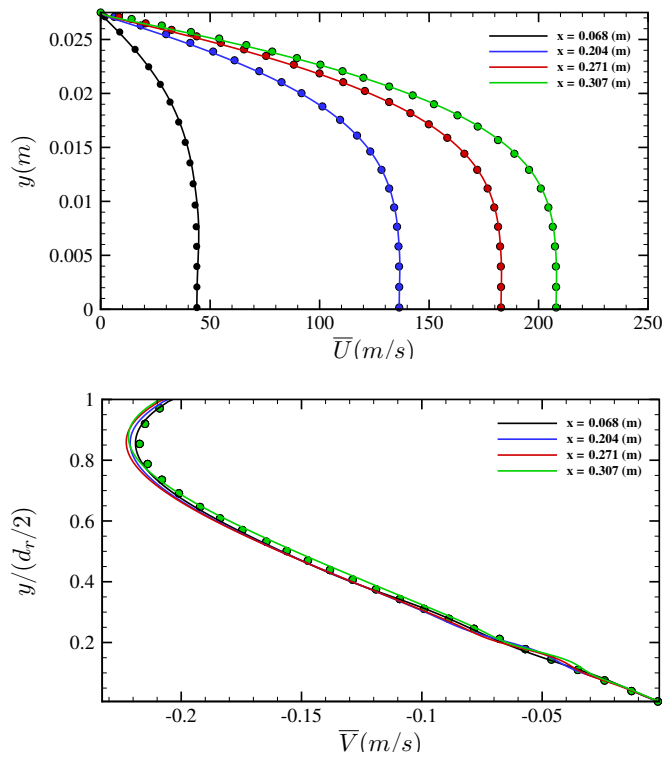


Figure 5.3: Comparison of (left) mean axial velocity and (right) mean radial velocity distribution from ILES (lines) at various stations with the theoretical solution (symbols).

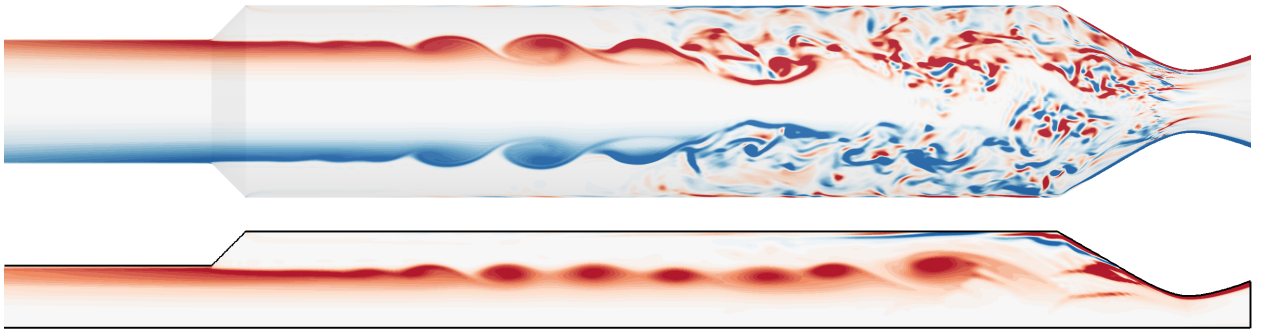


Figure 5.4: Contours of instantaneous spanwise vorticity in a longitudinal x-y plane for (a) the 3D ILES and (b) the 2D simulation. Blue and red contours represent clockwise and counter-clockwise rotating vortices. Sixty-four levels in the range $-25 < \omega_z T_{\text{ref}} < 25$ ($T_{\text{ref}} = 1.08 \cdot 10^{-3}$ s) are shown.

despite the flow is highly turbulent over most of the chamber cross-section. Changes in the mean axial distribution with respect to the Taylor-Culick solution have only been found at extremely large values of Re_c (greater than 10^5), that are not reached in the present configuration, characterized by an axial-flow Reynolds number $Re_c \approx 9 \cdot 10^4$ at the grain edge. Therefore, the Taylor-Culick solution obtained by the present ILES is expected to be representative of the experimental flow conditions in the first chamber.

The salient unsteady features of the flow in the SRM are illustrated in Fig. 5.4, where contours of the instantaneous vorticity field are reported in a longitudinal slice for ILES (top panel). For comparison purposes, contours of the vorticity field from the 2D simulation are also shown in the same figure (bottom panel). In both cases it is observed as the shear layer, developed along the injecting wall, detaches at the grain edge and a Kelvin-Helmholtz hydrodynamic instability is observed to occur, leading to a quasi-periodic vortex shedding. In the 2D case, the shear layer quickly grows past the grain edge and coherent vortices are found to roll-up. Then, they are convected in the axial direction and impinge against the aft-end of the chamber before being convected through the motor nozzle. In the 3D case, in the initial part of the shear-layer development a similar shedding of vortices is observed, that, however, due to the three-dimensionality of the phenomenon, break up generating turbulent structures elongated in the flow direction. These structures break into smaller and smaller structures as a result of the energy cascade phenomenon and are finally convected out of the domain through the SRM nozzle. The three-dimensional visualization reported in Fig. 5.5, where turbulent structures are extracted by means of an isosurface of the Q criterion [159], well highlights the destabilization process of the annular rollers detached from the edge, with the subsequent development of 3D perturbations and the transition to fine-scale turbulence. It is worth to remind that forcing was not required to sustain this transition process and that small random disturbances were only added at the initial time of the 3D computation.

5.3.2 Analysis of the wall-pressure signature

In this section a statistical analysis of the wall-pressure signature is carried out to characterize the level of pressure oscillations and frequency content of the signals in both the 2D and 3D simulations. Emphasis is given to the role played by the transition to turbulence observed to occur in the second

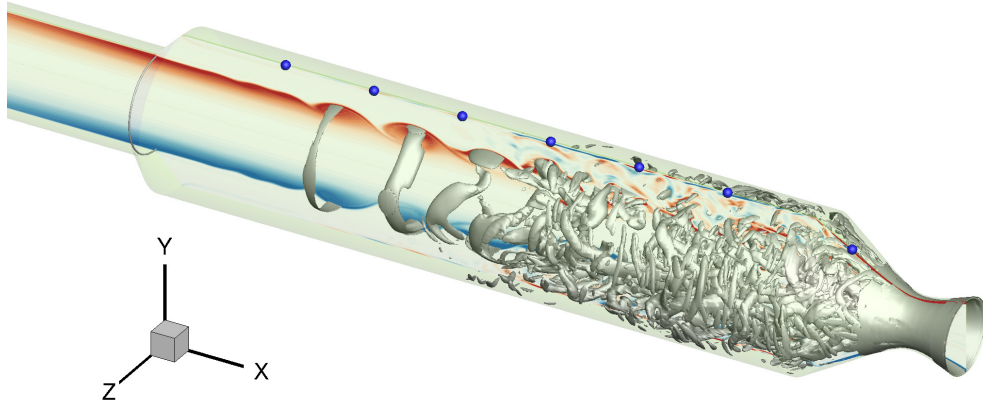


Figure 5.5: Visualization of turbulent structures through an iso-surface of the Q criterion. The blue circles denote the position of the experimental pressure probes.

chamber for the ILES case. Indeed, since the pressure oscillations are due to the coupling between the shear-layer structures and the acoustic longitudinal modes, the differences previously noticed between the 2D and 3D simulations are expected to induce strong repercussions on the acoustic coupling in the chamber and on the level of wall-pressure fluctuations. To that purpose, pressure signals are sampled at several axial positions corresponding to the location of the experimental probes, reported in Table 5.2 and visualized in Fig. 5.5.

Time history and root mean square

The time histories of pressure oscillations obtained in the 2D simulation are compared with those obtained in the 3D case in Fig. 5.6 for four representative probes. The first macroscopic feature highlighted by the pressure signals is the remarkable difference in the oscillation level, that is significantly lower in the 3D case for all the probes analyzed, particularly at the closed head end. Moreover, the shape of the 2D signals appear to be more regular than in the 3D case, where the pressure fluctuations are characterized by a more stochastic behavior that reflects the turbulent content of the simulation and the energy cascade phenomenon.

To provide quantitative evidence of the different behavior predicted by ILES, the distribution of the root-mean-square wall pressure fluctuations along the chamber wall p_{rms} is reported in Fig. 5.7, compared with the reference experimental data [15] and with data obtained by previous 2D numerical simulations [31, 160]. First, as a major result, it is observed that the rms distribution predicted by ILES closely reproduces the experimental behavior, characterized by low levels of pressure oscillations at the motor head end and along the whole grain surface. Then in the second chamber, where the turbulent shear layer develops, the intensity of pressure fluctuations gradually increases up to a maximum immediately before the beginning of the nozzle, representing the main source of the acoustic generation in the combustion chamber. The current 2D results generally agree with those of previous numerical studies, with the exception of the head end, where our p_{rms} is higher than the values reported from literature. We verified that this is an effect of the higher resolution here adopted and the use of a coarser grid leads to decreased values of wall-pressure fluctuations at the motor head end. Nevertheless, the present results globally confirm the higher level of pressure fluctuations predicted by all the simulations performed in a two-dimensional framework. Such ob-

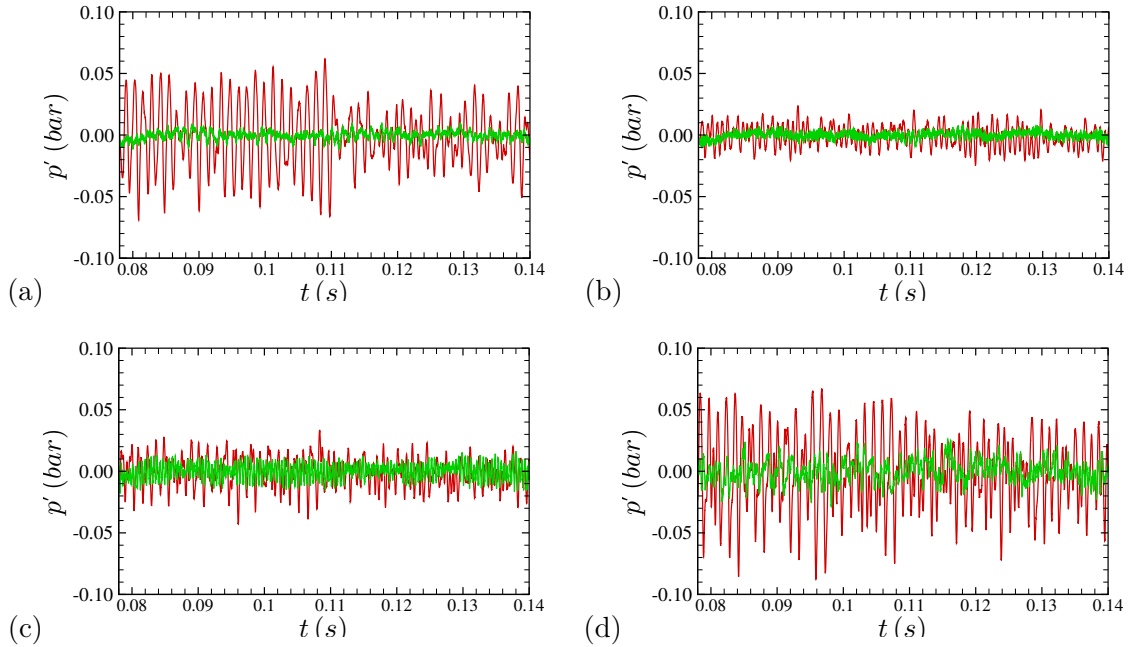


Figure 5.6: Comparison of the pressure oscillation signals extracted from 2D (red solid lines) and 3D (green solid lines) simulations at representative probes: (a) PC head, (b) PC 1, (c) PC 3 and (d) PC 5.

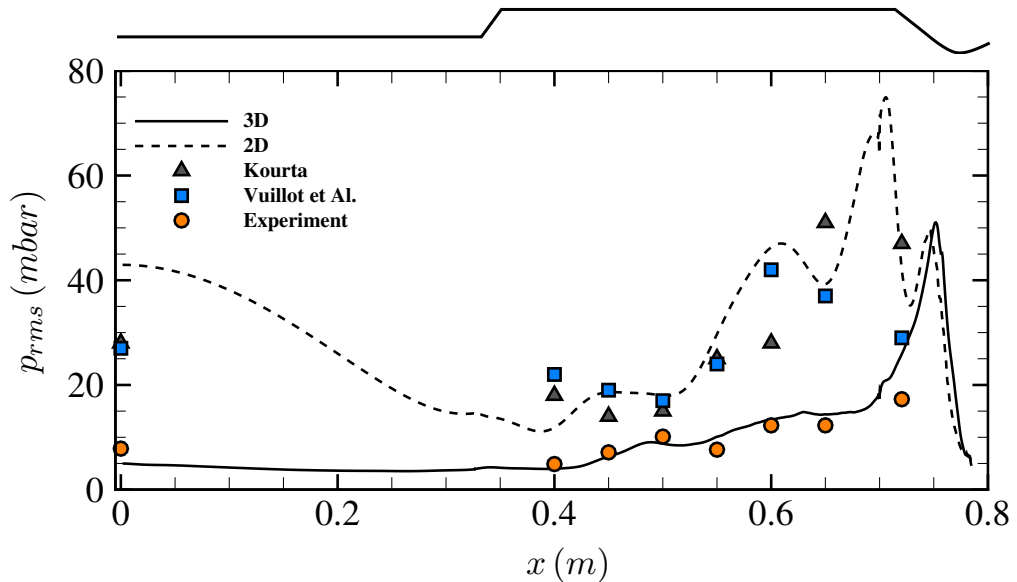


Figure 5.7: Distribution of the rms pressure fluctuations for the current 2D and 3D simulations, compared with reference experimental data (circles) and previous 2D computations.

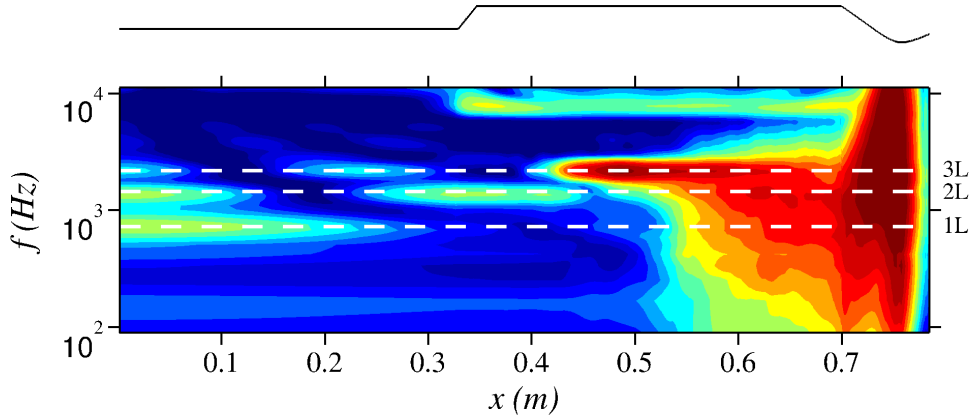


Figure 5.8: Contours of premultiplied power spectral densities ($f \cdot E_{pp}$) of the wall pressure signals as a function of the axial position and frequency from ILES. Sixteen contour levels are shown in exponential scale between $1.5 \cdot 10^3 \text{ Pa}^2$ and $5 \cdot 10^5 \text{ Pa}^2$.

servations seem to corroborate the original speculations made by Vuillot and Lupoglazoff [32], and reveal that capturing the turbulent break-up of the vortical structures shed by the grain edge is essential to correctly predict the acoustic coupling in the chamber and estimate the level of pressure oscillations in the SRM. The main effect of turbulence is to disrupt the coherence of the rollers seen in the axisymmetric computations, that impinging on the nozzle wall at the end of the motor produce the occurrence of large pressure disturbances travelling upstream and inducing the large level of pressure oscillations observed in the 2D data.

Frequency Fourier analysis

The premultiplied wall-pressure spectra $f \cdot E_{pp}(f)$ are reported in Fig. 5.8 as a function of both the axial coordinate x and frequency f for ILES. This representation as a two-dimensional map provides a complete picture of the spatial distribution of the energy of the pressure fluctuations along the SRM wall and of the contribution of the different frequencies to the total signal energy. The power spectral densities (PSD) have been estimated based on the Welch method, i.e., subdividing the overall pressure record into a number of segments ($N_{seg} = 10$) with 50% overlapping, which are individually Fourier-transformed. The frequency spectra are then obtained by averaging the periodograms of the various segments, thus minimizing the variance of the PSD estimator. Finally, for visualisation purposes, the Konno-Ohmachi smoothing [161] has been applied, whose filter function guarantees a constant bandwidth on a logarithmic scale. Note that, since the frequency axis is reported in log scale, the spectra are premultiplied by the frequency f so that the figure provides a direct perception of the amount of energy contained in a specific frequency range. The spectral map shows that the first three longitudinal acoustic modes ($L_1 = 724 \text{ Hz}$, $L_2 = 1448 \text{ Hz}$, $L_3 = 2172 \text{ Hz}$), identified by the horizontal white lines, dominate the pressure signal at the head end of the motor, with the higher peak corresponding to first axial mode. Moving downstream, the second axial mode becomes relevant in the middle of the chamber, between $0.25 \text{ m} < x < 0.45 \text{ m}$, in the region where the shear layer detaches from the grain and starts its development. The most interesting feature in the map is the appearance of a dominant peak at $x \approx 0.49 \text{ m}$, locked on a frequency corresponding to the third longitudinal mode $L_3 = 2172 \text{ Hz}$. Inspection of the frequency

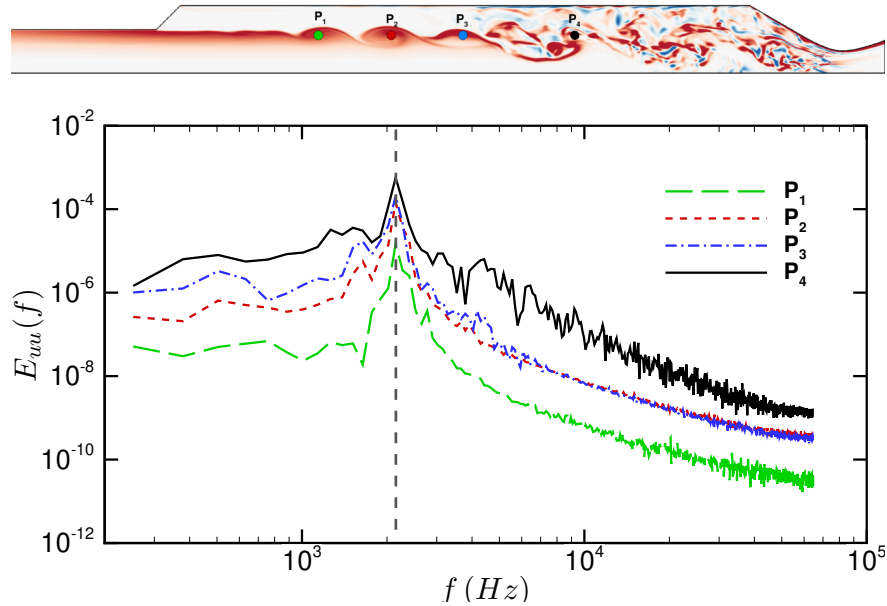


Figure 5.9: Frequency spectrum of the axial velocity component at several probes in the shear layer from ILES.

spectrum of the axial velocity signal from probes inside the shear layer (see Fig. 5.9) reveals that L_3 is also the frequency of the vortex shedding in the second chamber. This coupling on the third mode between pressure oscillations and vortex shedding was observed experimentally by Lupoglazoff and Vuillot [17], who connected it to the large turbulence levels in the early part of the firing, but it was never observed in 2D simulations. The appearance of this peak in the present ILES is thus significant because it reconciles the numerical prediction with the experimental observations. It also highlights the importance of capturing the transition process of the shear layer by means of high-fidelity numerical simulations to correctly predict the flow behavior and the level of pressure oscillations in the SRM. Finally, moving further downstream ($x > 0.6$ m) the pressure spectra are seen to gradually broaden, as expected in this region where the turbulent flow is fully developed and high-frequency fluctuations are excited by small-scale turbulent structures.

Space-time correlation analysis

Additional insights into the propagation of pressure disturbances in the SRM can be gained by inspection of the space-time correlation coefficient, defined as

$$C_{pp}(x_0, \Delta x, \Delta \theta, \Delta \tau) = \frac{R_{pp}(x_0, \Delta x, \Delta \theta, \Delta \tau)}{[R_{pp}(x_0, 0, 0, 0)]^{1/2} [R_{pp}(x_0, \Delta x, 0, 0)]^{1/2}}, \quad (5.3)$$

where

$$\overline{R_{pp}(x_0, \Delta x, \Delta \theta, \Delta \tau)} = \overline{p'_w(x_0, \theta, t) p'_w(x_0 + \Delta x, \theta + \Delta \theta, t + \Delta \tau)} \quad (5.4)$$

is the space-time correlation function, Δx and $\Delta \theta$ are the spatial separations in the axial and azimuthal directions, $\Delta \tau$ is the time delay, and the overbar denotes averages taken with respect to the azimuthal direction and time. Note that due to the inhomogeneity of the flow in the axial

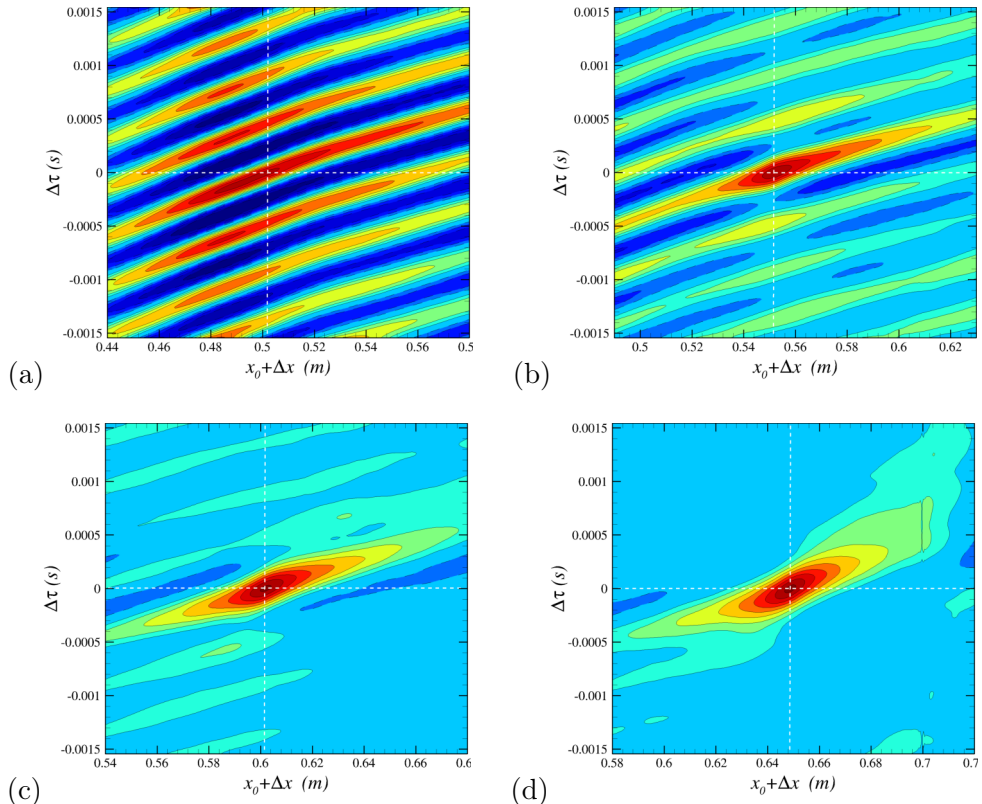


Figure 5.10: Contours of the space-time pressure correlation coefficient at representative probes from ILES: (a) PC 3 probe, (b) PC 4 probe, (c) PC 5 probe, (d) PC 6 probe. Sixteen equally spaced levels are shown between -0.5 and 1.

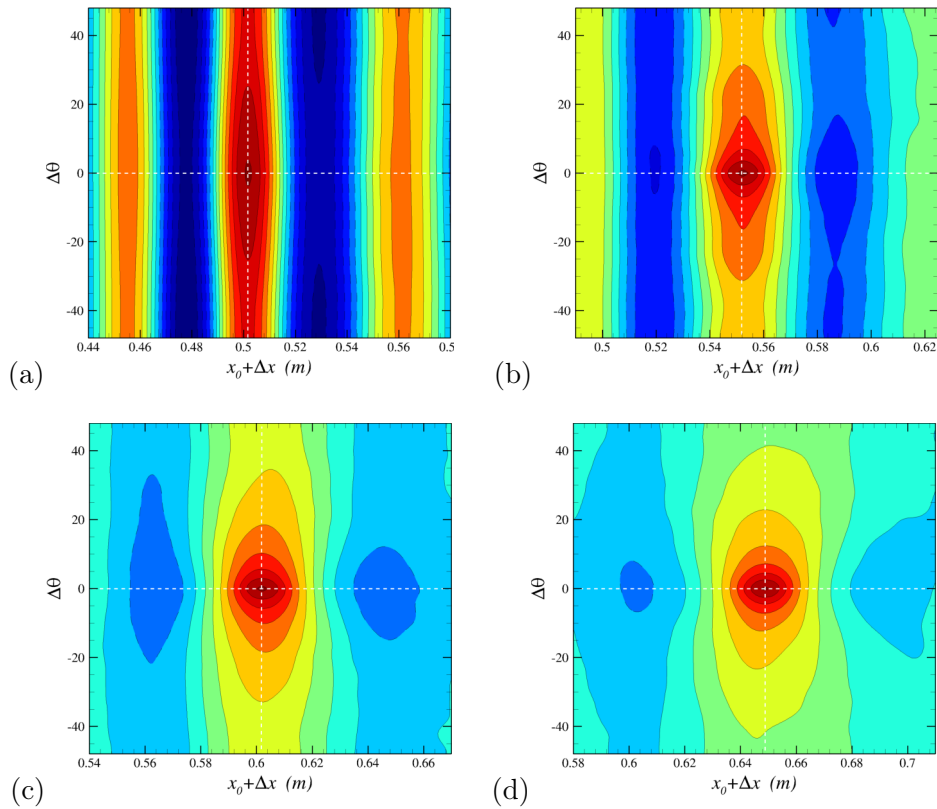


Figure 5.11: Contours of the two-point spatial correlation coefficient of the wall pressure at representative probes from ILES: (a) PC 3 probe, (b) PC 4 probe, (c) PC 5 probe, (d) PC 6 probe. Sixteen equally spaced levels are shown between -0.5 and 1.

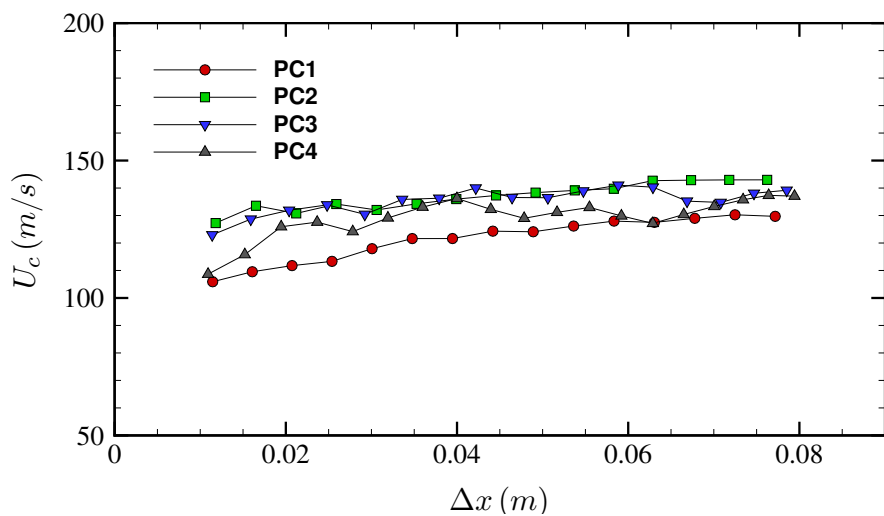


Figure 5.12: Distribution of the local convection velocity of the pressure-carrying eddies at several probes.

direction, C_{pp} explicitly depends on the axial position x_0 used to compute the correlation. Figure 5.10 reports contours of the space-time correlation coefficient $C_{pp}(x_0, \Delta x, 0, \Delta\tau)$ obtained from the ILES simulation at four representative stations along the C1xb SRM wall (x_0 corresponding to probes from PC3 to PC6). In all cases the shape of the contours in the space-time plane reflects the convective nature of the pressure field, with the pressure signal that is characterized by the downstream propagation of the pressure-carrying eddies. At PC3, the map highlights very well the signature of the shear-layer vortices, whose coherence produces the presence of alternate regions of high positive and negative correlation. Moving at the downstream stations (PC4, PC5 and PC6), the rollers influence gradually weakens, and the space time correlation tends to assume the typical shape observed in a turbulent boundary layer [162]. Similar considerations can be drawn for contours of the two-point spatial correlation $C_{pp}(x_0, \Delta x, \Delta\theta, 0)$, reported in Fig. 5.11 for ILES. At the beginning of the shear layer development (PC3) the pressure field is perfectly correlated in the azimuthal direction and the distance between two consecutive peaks provide an estimate of the distance between the eddies, in the range $0.045 \div 0.05$ m. Then, after the breakup of the rollers and the transition to fully-developed turbulence (PC4 and PC5), such coherence is gradually lost and at PC6 the two-point correlation is similar to that found in turbulent boundary layers [163]. In fact circular contours are observed for small spatial separations, associated with the nearly isotropic nature of small-scale eddies, whereas for large separations, the isolines become more elongated in the azimuthal direction, reflecting the anisotropic nature of the pressure carried eddies at the large scales.

From the space-time correlation maps of Fig. 5.10 it is possible to estimate the convection velocity (U_c) of the shear layer vortices carrying the pressure disturbances in the C1xb SRM. Following Wills [164], the convection speed corresponding to a given spatial separation Δx is defined as the ratio $\Delta x / \Delta\tau$ taken at the time delay value where the correlation coefficient attains a maximum. The resulting convection speed for the various pressure probes are displayed in Fig. 5.12, as a function of the spatial separation Δx . The convection velocities, are observed to weakly depends on the spatial separation and a slight increase is observed moving in the axial direction, from PC1 to PC4. When compared with the mean flow velocity taken at the axial location corresponding to the grain edge (\bar{U}_e) (see Fig. 5.2), the ratio $k = U_c / \bar{U}_e \approx 0.6$ is obtained, in close agreement with the value reported in Flatau and VanMoorhem [165] and Dotson et al. [166].

5.3.3 Acoustic feedback frequency

Having characterized the wall pressure signature in the SRM, it is worth to compare the computed vortex shedding frequency with that predicted by the acoustic feedback model developed by Rossiter [167] and applied by Dotson et al. [166] for the Titan IV SRM upgrade. The model was originally developed for the flow over rectangular cavities and it is based on the following building blocks: i) vortices are formed by the roll-up of the shear layer generated at an upstream point (the grain edge in the current configuration); ii) they are convected in the downstream direction and impinge on a surface (the nozzle wall); iii) an acoustic disturbance travels back in the upstream direction; iv) the perturbation reaches the upstream point, inducing the formation of a new vortex that rolls-up, closing the feedback loop. According to Powell [168], Rockwell [169], the vortex shedding period T

is given by

$$(m - \alpha) T = l/U_c + l/c \quad (5.5)$$

where l is the distance between the corner edge and the impingement point (stand-off distance), c is the speed of sound, α is a (small) correction factor that takes into account the delay between the vortex impingement and the generation of the acoustic perturbation (usually assumed in the range $0 \div 0.25$, see Dotson et al. [166]) whereas the value m , denoted as stage number, represents the number of vortices in the region between the grain edge and the nozzle. In the current configuration the stage number is $m = 6$, a value that can be inferred from the qualitative inspection of Fig. 5.4 but also computed as $m = \text{int}(l/d_v)$, where $d_v \approx 0.048$ m is the average distance between two consecutive vortices in the shear layer. By exploiting the ratio between the convection and the flow velocity $k = 0.6$, eq. (5.5) can be applied to estimate the vortex shedding frequency, that results

$$f_{AM} = \frac{\bar{U}_e}{l} \frac{m - \alpha}{M + 1/k} \quad (5.6)$$

where M is the Mach number. Considering the distance between the grain edge and the nozzle $l = 0.35$ m, an average value of the mean Mach number in the chamber ($M \approx 0.22$), an average flow velocity $\bar{U}_e = 220$ m/s, $k = U_c/\bar{U}_e = 0.6$, $\alpha = 0$ (see Flatau and VanMoorhem [165]) and the stage number $m = 6$, eq. (5.6) provides $f_{AM} \approx 2000$ Hz, corresponding to a Strouhal number $St_{AM} = f_{AM} l / \bar{U}_e \approx 3.18$, in good agreement with the frequency computed from ILES, $f = 2160$ Hz ($St \approx 3.43$).

Chapter 6

Dual Bell Nozzle

In this chapter the delayed detached eddy simulation DDES methodology has been used for studying the aeroacoustic resonance phenomenon inside an axi-symmetric rocket nozzle geometry, with a high value of the nozzle pressure ratio (NPR), resulting in a complex flow conditions. The case under investigation is a three-dimensional sub-scale Dual-Bell (DB) nozzle in a highly over-expanded regime, which has been experimentally tested at the DLR, and on which several numerical investigation have been carried out in the literature by means of RANS and URANS simulations.

In Sec. 6.1 and Sec. 6.2 of this chapter the test case is described, giving information about the geometry of the DB nozzle, the computational domain and its generation, as well as global information about the performed DDES simulation.

In Sec. 6.3 the results of the DDES are described. At the beginning, in Sec. 6.3.1, the flowfield characteristics are shown. In the following Sec. 6.3.2 the study focused on the unsteady pressure signature on the nozzle wall, through the use of Fourier-based spectral analysis. With the aim of identifying the cause of the aerodynamic side loads, the spectral properties of the wall-pressure unsteady signals in the azimuthal wavenumber space are shown in Sec. 6.3.3, in order to isolate the effect of each modes and to reveal the role of the DB inflection point on the aeroacoustic feedback loop. Finally, in Sec. 6.3.4 the aerodynamic loads distribution is discussed.

6.1 Test case description

The present investigation is carried out on the dual-bell geometry experimentally tested at DLR [65], characterized by a throat radius $r_t = 0.01$ m, a wall inflection angle $\alpha_i = 9^\circ$, a base area ratio

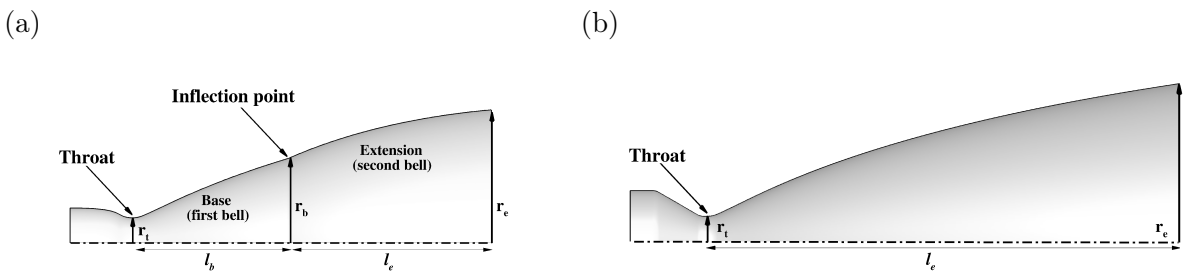


Figure 6.1: Schematic of (a) the dual-bell nozzle geometry and (b) a conventional truncated ideal contour (TIC) nozzle.

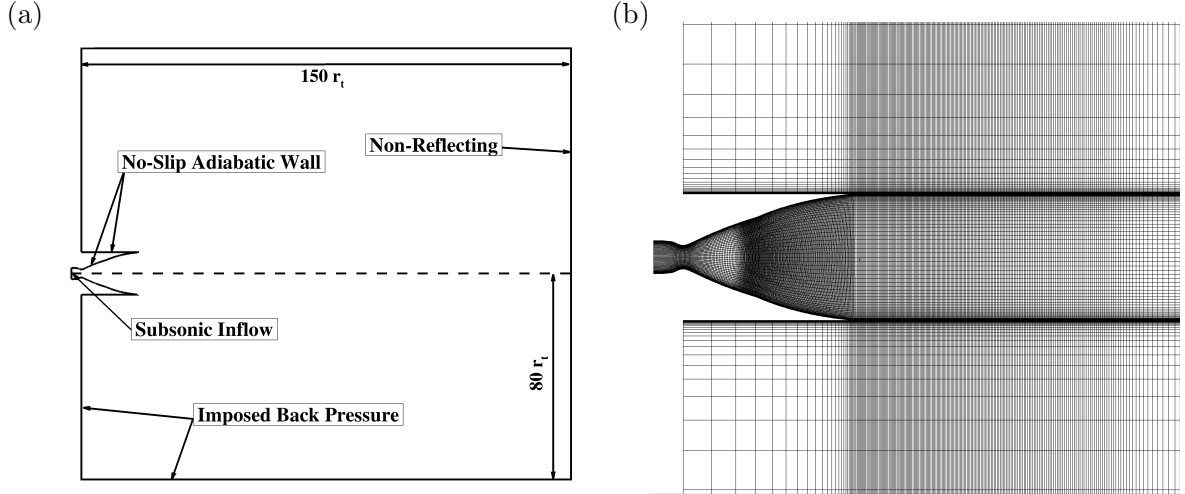


Figure 6.2: Schematic of (a) the computational domain and (b) the computational grid adopted for DDES in the x - y plane (only one every 8th grid nodes is shown).

$\epsilon_B = r_b^2/r_t^2 = 11.3$, an extension area ratio $\epsilon_E = r_e^2/r_t^2 = 27.1$, with the extension displaying a constant wall-pressure profile (CP). The nozzle pressure ratio is fixed at the value 45.7, since at this NPR the nozzle flow experiences a symmetric shock separation located exactly at the inflection point. The other parameters of the simulation were chosen to reproduce the operating conditions of the experimental campaign. In particular, the total temperature T_0 and the static ambient temperature T_a have been set equal to 300 K. The nozzle Reynolds number is

$$Re = \frac{\rho_0 a_0 r_t}{\mu_0} = \frac{\sqrt{\gamma}}{\mu_0} \frac{p_0 r_t}{\sqrt{R_{air} T_0}} = 1.03 \cdot 10^7, \quad (6.1)$$

where ρ_0 is the density, a_0 the speed of sound and $\mu_0 = \mu(T_0)$ is the molecular viscosity taken at the stagnation-chamber condition. The three-dimensional computational domain includes the external ambient (see Fig. 6.2) that extends up to $150 r_t$ in the longitudinal direction and $80 r_t$ in the radial one from the symmetry axis. The boundary conditions are imposed as follows: total temperature, total pressure and flow direction are enforced at the nozzle inflow, while on the outflow boundary at the end of the external domain a non-reflecting boundary condition is implemented. A back-pressure equal to the ambient pressure p_a is imposed at the other boundaries. The no-slip adiabatic condition is prescribed for the nozzle walls. The mesh resolution was selected following a preliminary sensitivity study carried out on steady-state axisymmetric RANS computations, for which convergence of the separation location was obtained. The RANS solution was also used to initialise the three-dimensional DDES simulation. The development of turbulent structures and the passage from modelled to resolved turbulence was triggered by adding random perturbations to the streamwise velocity field only at the initial time of the 3D computation. Those perturbations have a maximum magnitude of 3% of the inflow velocity and a flat spectrum. We point out that, in our approach, no resolved turbulence upstream of the separation is enforced. The computational domain is composed by 136 structured blocks in the x - y plane, each block discretized with 22×256 cells. The 3D mesh includes 256 cells in the azimuthal direction, for a total number of approximately 196 million cells. The computation was run with a time step $\Delta t = 4.65 \cdot 10^{-8}$ s and a relatively long time span was simulated $T = 0.0172$ s, which guarantees coverage of frequencies down to at least

Table 6.1: Dual-Bell and TIC nozzles geometrical parameters.

		DB	TIC
Throat radius	r_t	10 mm	19 mm
Area ratio	ϵ_E	27.1	38
Total length	L_{tot}/r_t	14.24	18.44

$f_{min} \approx 58$ Hz. A total of 80 full three-dimensional fields have been collected at time intervals of $2.15 \cdot 10^{-4}$ s for post-processing purposes. Furthermore, samples of the pressure field at the wall and in an azimuthal plane have been recorded at shorter time intervals of $2.34 \cdot 10^{-6}$ s to guarantee sufficient resolution for the frequency analysis.

In the following, the results for the dual bell are compared with those recently obtained for a truncated ideal contour (TIC) nozzle with free-shock separation (FSS) operating at $NPR = 30.35$, experimentally tested at the University of Texas at Austin and simulated with the same methodology here exposed [95]. The mesh resolution of the TIC computation was similar to that here employed for the dual-bell nozzle, being the two cases characterized by a similar Reynolds number. Basic geometric properties of the TIC nozzle are a throat radius of $r_t = 0.019$ m, an exit radius of $r_e = 0.117$ m and a throat-to-exit length of $L = 0.351$ m. A summary of the main geometrical parameters of both the dual bell and TIC nozzle is reported in Table 6.1. An extensive analysis on the flow unsteadiness and wall-pressure signature for the TIC nozzle can be found in Martelli et al. [95]. Here, novel results for that geometry are presented concerning the analysis of the aerodynamic side loads, compared in Sec. 6.3.4 with those generated in the dual-bell nozzle.

6.2 Computational strategy

As already mentioned in Chapter 2 and recalled in Sec. 5.2, we consider the three-dimensional Navier-Stokes governing equations for a compressible, viscous and heat-conducting gas in conservation form

$$\begin{aligned} \frac{\partial \rho}{\partial t} + \frac{\partial(\rho u_j)}{\partial x_j} &= 0, \\ \frac{\partial(\rho u_i)}{\partial t} + \frac{\partial(\rho u_i u_j)}{\partial x_j} + \frac{\partial p}{\partial x_i} - \frac{\partial \tau_{ij}}{\partial x_j} &= 0, \\ \frac{\partial(\rho E)}{\partial t} + \frac{\partial(\rho Eu_j + pu_j)}{\partial x_j} - \frac{\partial(\tau_{ij} u_i - q_j)}{\partial x_j} &= 0, \end{aligned} \quad (6.2)$$

where ρ is the density of the flow, u_i denotes the velocity component in the i -th coordinate direction ($i = 1, 2, 3$), E is the total energy per unit mass and p is the thermodynamic pressure. τ_{ij} and q_j denote the total stress tensor and total heat flux, that are given by the sum of a viscous and a turbulent contribution, according to

$$\tau_{ij} = 2\rho(\nu + \nu_t)S_{ij}^* \quad q_j = -\rho c_p \left(\frac{\nu}{Pr} + \frac{\nu_t}{Pr_t} \right) \frac{\partial T}{\partial x_j} \quad (6.3)$$

where the Boussinesq hypothesis is applied through the introduction of the eddy viscosity ν_t (defined by the turbulence model), S_{ij}^* is the traceless strain-rate tensor and ν the kinematic viscosity,

depending on temperature T through the Sutherland's law. The molecular and turbulent Prandtl numbers Pr and Pr_t are considered constant and equal to 0.72 and 0.9, respectively.

The numerical methodology employed in this study is a calibrated version of the delayed detached eddy simulation method [129], an efficient and powerful hybrid RANS/LES technique well suited to capture the unsteadiness of high-Reynolds number turbulent flows (see Sec. 3.4). The current implementation is based on the Spalart-Allmaras (SA) turbulence model, which solves a transport equation for a pseudo eddy viscosity $\tilde{\nu}$

$$\frac{\partial(\rho\tilde{\nu})}{\partial t} + \frac{\partial(\rho\tilde{\nu}u_j)}{\partial x_j} = c_{b1}\tilde{S}\rho\tilde{\nu} + \frac{1}{\sigma} \left[\frac{\partial}{\partial x_j} \left[(\rho\nu + \rho\tilde{\nu}) \frac{\partial\tilde{\nu}}{\partial x_j} \right] + c_{b2}\rho \left(\frac{\partial\tilde{\nu}}{\partial x_j} \right)^2 \right] - c_{w1}f_w\rho \left(\frac{\tilde{\nu}}{\tilde{d}} \right)^2, \quad (6.4)$$

where \tilde{d} is the model length scale, f_w is a near-wall damping function, \tilde{S} is a modified vorticity magnitude, and $\sigma, c_{b1}, c_{b2}, c_{w1}$ are model constants. The pseudo eddy viscosity $\tilde{\nu}$ is directly linked to the eddy viscosity ν_t through $\nu_t = \tilde{\nu} f_{v1}$, where the correction function f_{v1} is used to guarantee the correct near-wall boundary-layer behavior. As already mentioned in Sec. 3.4.3, the DDES approach the turbulence model automatically switches between a pure RANS mode, active in flow regions with attached boundary layers, to a pure LES mode, active in flow regions detached from the wall, where the computation can directly resolve the large scale, energy containing eddies. This objective is achieved by defining the length-scale \tilde{d} in (6.4) as

$$\tilde{d} = d_w - f_d \max(0, d_w - C_{DES} \Delta), \quad (6.5)$$

where d_w is the distance from the nearest wall, Δ is the subgrid length-scale that controls the wavelengths resolved in LES mode and C_{DES} is a calibration constant set equal to 0.65 in the original model. On the basis of previous calibration studies performed on DDES of a sub-scale rocket nozzle [95, 153] the constant C_{DES} has been set equal to 0.20 and the function f_d here employed is

$$f_d = 1 - \tanh \left[(16r_d)^3 \right], \quad r_d = \frac{\tilde{\nu}}{k^2 d_w^2 \sqrt{U_{i,j} U_{i,j}}}, \quad (6.6)$$

where $U_{i,j}$ is the velocity gradient and k the von Karman constant. The f_d function, that is built in such a way that its value is 0 in boundary layers and 1 in LES regions, represents the main difference between the DDES strategy and the original DES approach [112], denoted as DES97. It guarantees that attached boundary layers are always treated in RANS mode, even in the case of extremely fine grids, thus allowing to alleviate the well-known phenomenon of modeled stress depletion, which in turn can lead to grid-induced separation [129]. The sub-grid length scale is specified according to the formulation proposed by Deck [124], and it depends on the flow itself, through f_d as

$$\Delta = \frac{1}{2} \left[\left(1 + \frac{f_d - f_{d0}}{|f_d - f_{d0}|} \right) \Delta_{\max} + \left(1 - \frac{f_d - f_{d0}}{|f_d - f_{d0}|} \right) \Delta_{\text{vol}} \right], \quad (6.7)$$

with $f_{d0} = 0.8$, $\Delta_{\max} = \max(\Delta x, \Delta y, \Delta z)$ and $\Delta_{\text{vol}} = (\Delta x \cdot \Delta y \cdot \Delta z)^{1/3}$. The main idea of this formulation is to take advantage of the f_d function to switch between Δ_{\max} , needed to shield

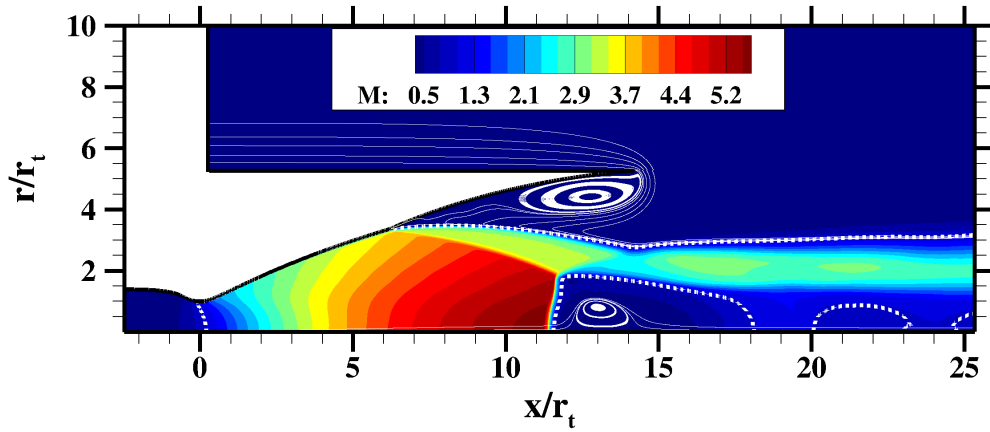


Figure 6.3: Contours of the averaged Mach number field from DDES. The white dashed line denotes the sonic level.

the boundary layer, and Δ_{vol} , needed to ensure a rapid destruction of modelled viscosity to unlock the Kelvin-Helmholtz instability and accelerate the passage to resolved turbulence in the separated shear layer.

The simulations have been carried out by means of the in-house finite-volume flow solver described in Chapter 4, which solves the compressible Navier-Stokes equations on structured grids. The solver have been widely employed in the past to investigate the dynamics of turbulent, separated flows in transonic and supersonic rocket nozzles, involving complex shock-waves/boundary-layer interactions [2, 103, 153]. In the flow regions away from the shock, the spatial discretization consists of a centered, second-order, energy consistent scheme, that makes the numerical method extremely robust without the addition of numerical dissipation [136]. This feature is particularly useful in the flow regions treated in LES mode, where in addition to the molecular, the only relevant viscosity should be that provided by the turbulence model. Strong compressions in the flow are identified by means of the Ducros shock sensor [140], that is used to switch the discretization of the convective terms of the governing equations to third-order Weighted Essentially Non Oscillatory reconstructions for cell-faces flow variables. The viscous fluxes are evaluated through compact, second-order central-difference approximations. A low-storage, third-order Runge-Kutta algorithm [150] is used for time advancement of the semi-discretized ODEs' system.

6.3 Results

6.3.1 Flowfield organisation

The main features of the flow pattern inside the dual-bell nozzle are reported in Fig. 6.3, which shows a longitudinal $x - r$ plane with the iso-contours of the mean Mach-number field, obtained by averaging in time and in the azimuthal direction. At the selected NPR, the flow is separated and anchored at the inflection point, generating a free shear layer. A shock system arises comprising the conical separation-shock, a Mach-disk reflection and a second conical shock, which re-directs the shear layer in a direction almost parallel to the nozzle axis. The dual-bell extension is characterized by a considerable subsonic turbulent recirculating region. The flow downstream of the Mach disk is initially subsonic, then it experiences an expansion process across a fluid-dynamic throat, that is

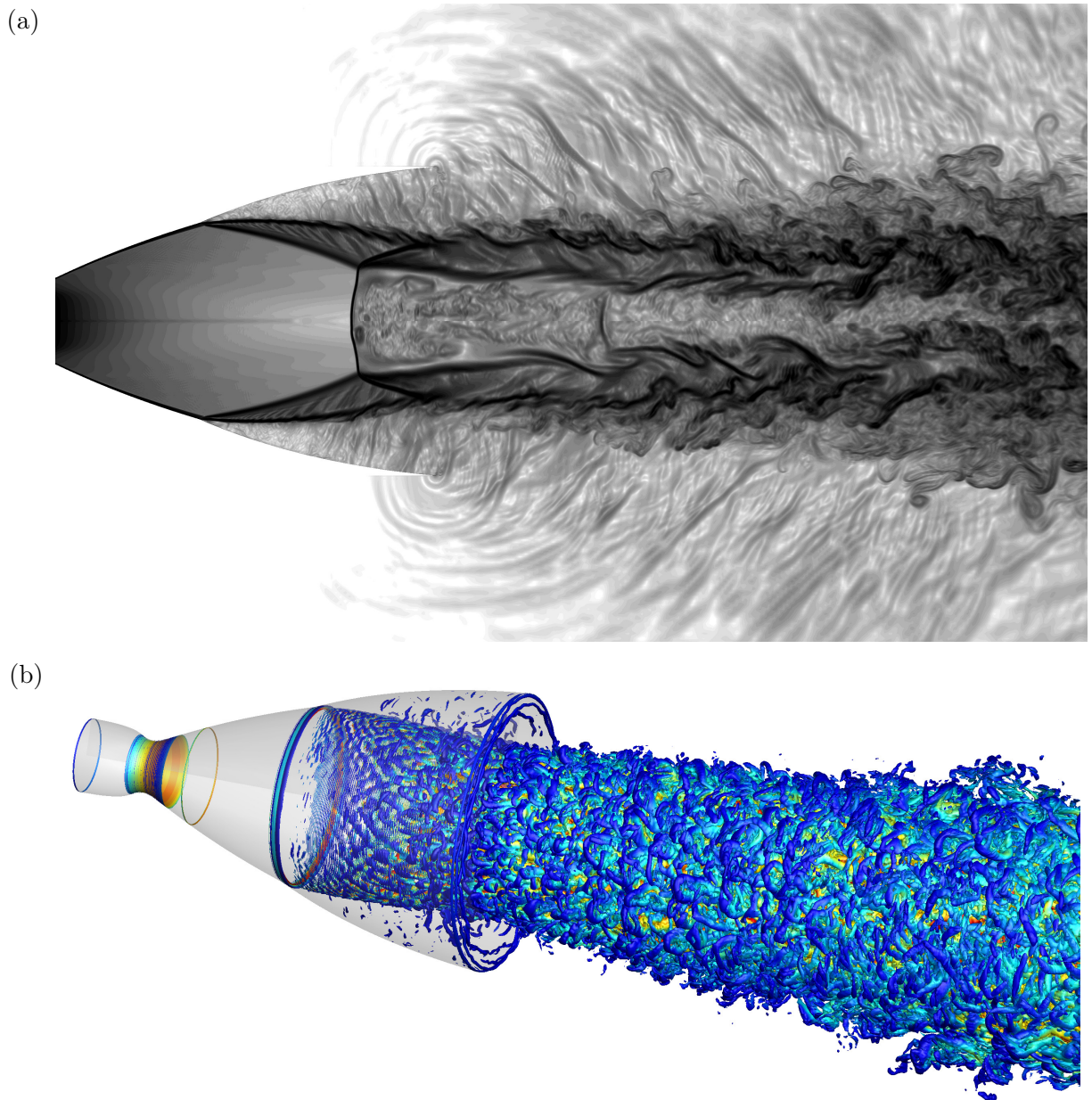


Figure 6.4: Visualisation of (a) the instantaneous density-gradient magnitude (numerical Schlieren) in an x-y plane and of (b) turbulent structures through an iso-surface of the Q criterion, coloured with the local value of the longitudinal velocity.

visible from the sonic line, and again accelerates to a supersonic velocity. Then a new shock appears to balance the pressure of the flow to the ambient level. It is also interesting to observe the presence of a recirculating region near the nozzle axis downstream the Mach disk. This region is fed by the vorticity produced by the shock curvature, which causes an entropy gradient in the radial direction and hence vorticity according to the Crocco's theorem.

The unsteadiness of the flow is highlighted by Fig. 6.4 (a), where contours of the density-gradient magnitude are displayed in a longitudinal $x-r$ plane. The developing turbulent structures of the two co-annular supersonic shear layers are well visible. The external shear layer originates from the jet detachment from the wall and the internal one originates from the triple point of the Mach reflection. The two layers merge downstream in the external ambient, where the Mach waves irradiated by the vortices are well visible. It is also possible to observe fine turbulent structures emitted by the Mach disk, coherently with the observation reported above on the entropy gradient generation due to the shock bending. The Q-criterion is generally used to identify the tube-like structures from a qualitative point of view [159]. In this work a modified definition of the Q-criterion has been adopted to include the effects of compressibility [170]. Let $A = \nabla \mathbf{u}$ be the gradient velocity tensor and $A^* = (A - \frac{1}{3} \nabla \cdot \mathbf{u} I)$ its traceless part, turbulent structures are extracted by visualising regions with a positive iso-value of the second invariant of A^* , defined as $Q^* = -\frac{1}{2} A_{ij}^* A_{ji}^*$, since in these regions rotation exceeds the strain. An isosurface of the Q-criterion is shown in Fig. 6.4 (b), coloured according to the value of the streamwise velocity component. It shows that the Kelvin-Helmotz instability of the initial part of the shear layer is not characterised by the coherent toroidal vortices which can be found in incompressible flows. Instead, we observe that oblique modes dominate the initial part of the shear layer, then leading to the generation of small-scale three-dimensional structures, well resolved by the present DDES approach. The differences in the initial shear layer development observed with respect to the typical pattern of low-speed flows can be attributed to the large local convective Mach number ($M_c \approx 1$) at the beginning of the detached shear layer, which changes the shear-layer instability process [171]. A similar behavior was observed by Martelli et al. [95] in a conventional TIC nozzle with flow separation and by Simon et al. [172] in a supersonic cylindrical base flow.

6.3.2 Analysis of the wall-pressure signature

The spatial evolution of the mean wall pressure (\bar{p}_w/p_a), averaged in time and in the azimuthal direction, is presented in Fig. 6.5(a), compared with the reference experimental data [65]. The figure is normalized with the ambient pressure for comparison purposes. The mean wall pressure decreases until the separation point, which is located at the inflection point, then the oblique shock causes a sudden increase up to a plateau value close to the ambient pressure level. The numerical data are in good agreement with the experimental ones. In particular, the right values of wall pressure in the turbulent recirculating zone indicates that the LES-branch simulation is able to correctly capture the momentum exchange between the main jet and the separated flow, dominated by the high convective Mach number of the shear layer [173]. A small difference is only observed in the average position of the separation point, that can be attributed to the inevitable transition delay from RANS to LES [131]. The standard deviation of the wall-pressure signal (σ_w/p_w) is shown in Fig. 6.5(b) and compared with the corresponding experimental values. The distribution of σ_w/p_w

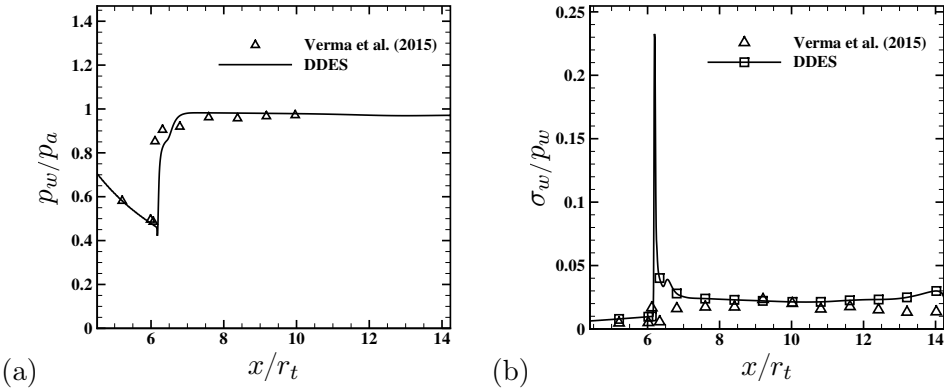


Figure 6.5: Comparison of the distribution of the normalized mean wall pressure (a) and standard deviation of wall-pressure fluctuations (b) with experimental data.

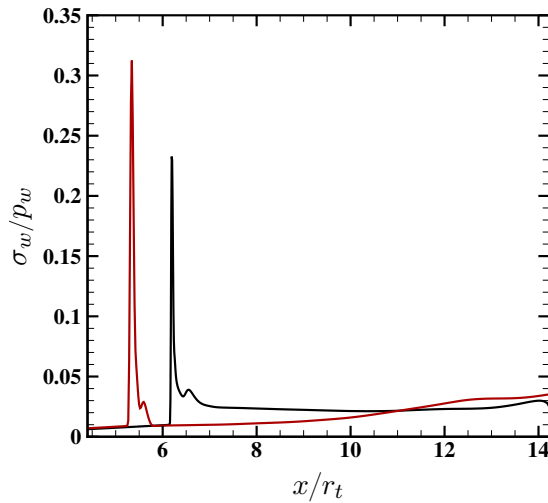


Figure 6.6: Comparison between dual-bell and TIC nozzles of the standard deviation of wall-pressure fluctuations. The black solid line refers to the dual-bell nozzle while the red solid one to the TIC.

along the longitudinal axis is typical of shock-wave/turbulent boundary layer interactions [174], characterised by a dominant sharp peak at the separation-shock location and followed downstream by a lower and almost constant level in the zone where the turbulent shear layer develops. The numerical standard deviation agrees with the experimental behavior, especially in the turbulent recirculating zone. It seems that the sharp peak predicted by the DDES at the shock location is not captured by the experimental measurements, probably due to the probe spacing. Indeed, the flow separation is fixed at the inflection point, therefore the pressure fluctuations are confined in a very narrow spatial range. The dual-bell standard deviation of the wall-pressure fluctuations is also compared with that of the TIC nozzle in Fig. 6.6. It is possible to note that the TIC distribution is characterised by a higher value in correspondence of the peak and by a more marked drop downstream of the shock location. Then the energy level of the pressure fluctuation gradually increases during the development of the shear layer. The dual-bell nozzle instead has a more flat trend downstream of the peak.

To provide a global picture of the pressure energy distribution along the nozzle wall and in the frequency domain, contours of the premultiplied wall-pressure spectra $G(f) f/\sigma^2$ are reported

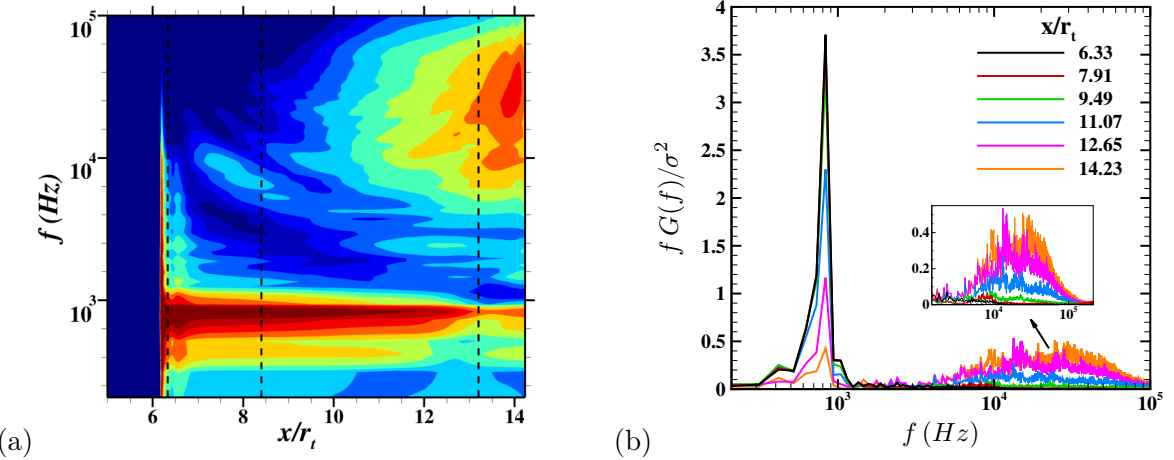


Figure 6.7: Dual-bell nozzle: (a) contours of premultiplied power spectral densities $G(f) \cdot f / \sigma^2$ of the wall-pressure as a function of the streamwise location and frequency; (b) axial evolution of the normalized spectra at representative streamwise locations. Eleven contour levels are shown in exponential scale between $5 \cdot 10^{-4}$ and 0.1.

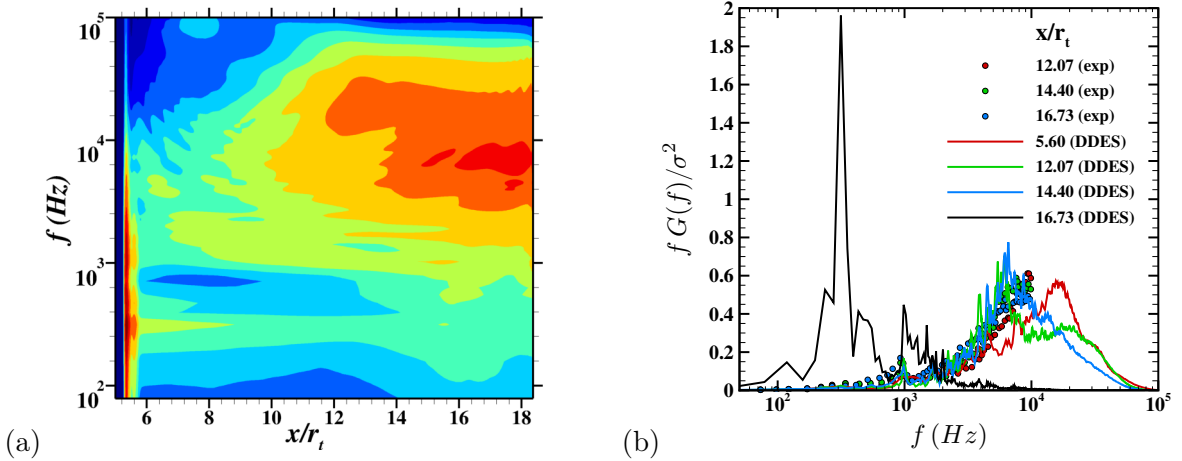


Figure 6.8: TIC nozzle: (a) contours of premultiplied power spectral densities $G(f) \cdot f / \sigma^2$ of the wall-pressure as a function of the streamwise location and frequency; (b) axial evolution of the normalized spectra at representative streamwise locations. Eleven contour levels are shown in exponential scale between $5 \cdot 10^{-4}$ and 0.1. The circles in (b) denote reference experimental data [42].

Table 6.2: Comparison of the shock motion peak frequencies with the experimental data.

x/r_t	calibrated DDES		Exp. [65]	
	f (Hz)	St	f (Hz)	St
6.33	833	0.057	775	0.053
8.40	833	0.057	764	0.052
13.20	833	0.057	787	0.054

in Fig. 6.7(a) with respect to the longitudinal coordinate x/r_t and frequency f . This graphical representation of the contour map is useful to provide a complete vision of the energy distribution in the space (along the nozzle wall) and in the frequency domain. The Welch method is used to calculate the power spectral densities (PSD) of the entire pressure signal, which has been subdivided into 12 segments with an overlap of 50%. Each segment is then Fourier-transformed and the final frequency spectrum is obtained by averaging each periodograms in order to reduce the variance of the individual power measurement. Moreover, the Konno-Ohmachi smoothing [161] has been used for graphical visualisation purposes and to ensure a constant bandwidth on a logarithmic scale through its filter function. It may be worthwhile to remember that the spectra are premultiplied by the frequency f to provide a direct estimation of the energy content inside a specific frequency range. From the spectral map, it is possible to observe the presence of two regions characterised by high fluctuation energy. The first zone of interest is located near the separation-shock average location ($x/r_t \approx 6.3$, see Fig. 6.3) and is characterised by a broad bump in the low-medium frequency range and very narrow in the longitudinal direction, that is clearly associated to the signature of the unsteady shock motion. The peak of this bump is at a frequency of ~ 830 Hz and its footprint is well visible in the spatial direction until the end of the nozzle. According to Baars et al. [42] and Martelli et al. [95] the low-frequency peak can be attributed to an acoustic resonance, which can be described by the one-quarter acoustic standing wave model [69] in open-ended pipes. The resonance frequency f_{ac} can be expressed as follows,

$$f_{ac} = \frac{a_\infty}{4(L + \varepsilon)} \quad (6.8)$$

where $a_\infty = 345\text{m/s}$ is the ambient speed of sound and $L = l_e = 0.0804\text{ m}$ is the distance between the inflection point and the nozzle lip. This distance should correspond to the pipe length in the 1D acoustic model and ε is an opened-end empirical correction parameter [66]. According to Proschanka et al. [66] this parameter can vary between $0.5L$ and 0 giving a range of frequency between 715 Hz and 1073 Hz, which include the numerical peak frequency of 833 Hz. It should also be considered that the presence of a large turbulent recirculating region, the unsteady detached shear layer and the area ratio variation in the second bell increase the difference of the present situation with the acoustic pipe 1D model. The second region characterized by high levels of pressure fluctuations is located downstream of the separation shock, in a high-frequency range between $f = 10^4$ and 10^5 Hz. The spectral map highlights that this second (broad) peak at high-frequency gradually appears moving in the downstream direction, and it is associated with the development of the separated shear layer, from which pressure disturbances are emitted through vortices that are convected downstream at high speed.

For a better quantification of the evolution of the wall-pressure frequency content along the longitudinal axis, Fig. 6.7(b) shows the premultiplied spectra at six axial equispaced probes. The peaks associated to the shock movement have very high amplitudes at ≈ 833 Hz and they persist for almost all the stations considered. Starting from the first probe the energy content of the shock peak tends to reduce along the x-axis whereas the energy contribution of the separated shear layer rises in amplitude at higher frequencies. Table 6.2 reports the peak frequencies of the spectra (attributed to the acoustic resonance) at the three different axial stations corresponding to the location of the experimental probes (black dashed lines in Fig. 6.7a). There is a rather good agreement between the

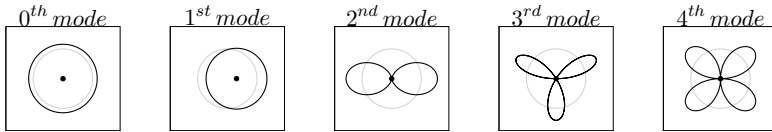


Figure 6.9: Physical interpretation of the Fourier azimuthal decomposition. Solid black lines refer to the real ($m > 0$) part of the Fourier coefficients, solid grey lines refer to the unit circle.

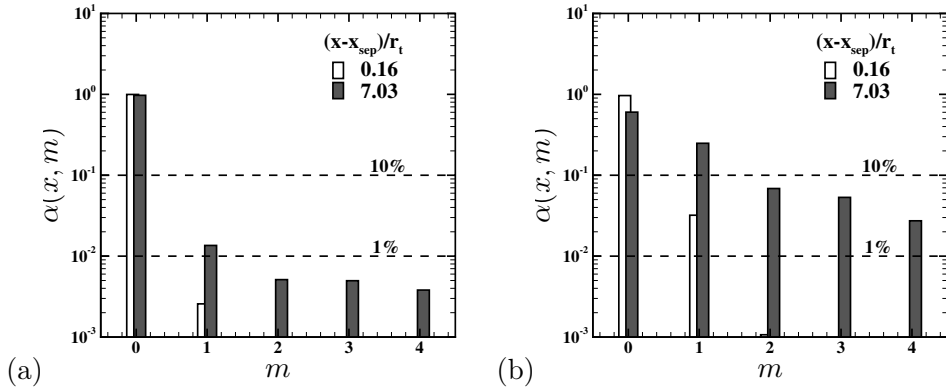


Figure 6.10: Normalized eigenspectra of the Fourier modes as fraction of resolved energy per mode at two different axial stations: (a) dual-bell nozzle and (b) TIC nozzle.

numerical results (833 Hz) and the experiments (between 775 Hz and 787 Hz), since the deviation from the experimental values falls within the uncertainty of the numerical spectra ($f_{min} = 58$ Hz). In addition Verma et al. [65] shows that the acoustic tone persists all along the second bell also in the experiment.

Fig. 6.8 shows the frequency spectra of the wall-pressure fluctuations corresponding to the TIC nozzle, as also reported in Martelli et al. [95]. In this case, to provide a further experimental-numerical validation, premultiplied spectra are reported at three axial stations corresponding to positions where experimental data from dynamic Kulite transducers are available. The main quantitative difference is that the footprint of the shock oscillation decreases much rapidly in the longitudinal direction with respect to the dual-bell case. Furthermore, the TIC wall-pressure signature presents some non-negligible energy in the intermediate frequency range (around 1 kHz) visible in both the numerical and experimental spectra, whereas the dual-bell nozzle show a very small energy content in the medium frequency range (around ≈ 2300 Hz). As previously speculated by Jaunet et al. [92] and then confirmed by Martelli et al. [95], this intermediate-frequency peak can be attributed to a screech-like mechanism with a antisymmetric-type mode occurring inside the nozzle. This aspect is deeply discussed in the following section.

6.3.3 Azimuthal decomposition of the pressure field

The proper way to correlate the frequency and energy content of the wall-pressure signature with the aerodynamic side loads is to evaluate the Fourier azimuthal wavenumber-frequency spectrum, defined as

$$\phi_{pp}(x, m, f) = \int_{-\infty}^{\infty} \int_0^{2\pi} R_{pp}(x, 0, \Delta\theta, \Delta\tau) e^{-i(m\Delta\theta + f\Delta\tau)} d(\Delta\theta) d(\Delta\tau), \quad (6.9)$$

with R_{pp} indicating the space-time correlation function of the wall-pressure fluctuations:

$$R_{pp}(x, \Delta x, \Delta\theta, \Delta\tau) = \langle p'_w(x, \theta, t) p'_w(x + \Delta x, \theta + \Delta\theta, t + \Delta\tau) \rangle \quad (6.10)$$

where Δx and $\Delta\theta$ are the spatial separations in the streamwise and azimuthal directions, $\Delta\tau$ is the time delay, and $\langle \rangle$ denotes averaging with respect to the azimuthal direction (exploiting homogeneity) and time. The symbol m indicates the mode number in the azimuthal direction, also called Fourier-azimuthal wavenumber and it is noteworthy to remember that the asymmetric mode $m = 1$ is the only one capable of providing a contribution to the side loads, as also shown in Fig. 6.9 where the real part ($m > 0$) of the first five Fourier azimuthal modes is reported. Following Baars et al. [42], we introduce the total resolved energy $\Lambda(x)$ for each longitudinal station of the nozzle as:

$$\Lambda(x) = \sum_m \lambda^{(m)}(x) \quad (6.11)$$

where $\lambda^{(m)}(x)$ is the variance of the m^{th} time-dependent Fourier-azimuthal mode coefficient. On the base of these definitions it is possible to show in Fig. 6.10 the eigenspectra of the Fourier modes as fractions of the resolved energy per mode $\alpha(x, m)$:

$$\alpha(x, m) = \frac{\lambda^{(m)}(x)}{\Lambda(x)}, \quad (6.12)$$

for two axial stations for both nozzles. The axial distances are evaluated from the separation location and normalized with throat radius for comparison purposes. Starting with the dual-bell nozzle case, Fig. 6.10 (a), it is evident that the energy of the zeroth mode is by far the dominant one along the nozzle. The energy of the mode $m = 1$ is nearly negligible near the separation location and shows an increment at the downstream station, but always remaining a small fraction (1.8% at most) of the total resolved energy. The higher modes appear to be non-negligible (but always less than 1%) only at the downstream station. The picture highlighted by Fig. 6.10 (b) for the TIC nozzle is rather different. Indeed, it is possible to appreciate a non-negligible decrease of the energy of the zeroth mode along the nozzle and an important growth of the first mode, that at $(x - x_{\text{sep}})/r_t = 7.03$ provides a 30% contribution to the total resolved energy. The energy of the higher modes is still negligible near the shock location, giving a minimal contribution only at the downstream station. To evaluate the frequency content of the time-dependent Fourier azimuthal coefficients, their power spectral densities are computed for both nozzles. Fig. 6.11 shows the spectra for the symmetric ($m = 0$) and asymmetric ($m = 1$) modes at the same two axial stations of Fig. 6.10. To compare the two different nozzles, a Strouhal (St) number is introduced as in Tam et al. [175]:

$$St = f \frac{D_j}{U_j}, \quad (6.13)$$

where U_j is the fully expanded jet velocity

$$U_j = \sqrt{\gamma RT_0} \frac{M_j}{\sqrt{1 + \frac{\gamma-1}{2} M_j^2}}, \quad (6.14)$$

Table 6.3: Modes peak frequency, St and St* numbers for Dual-Bell and TIC nozzles.

$(x - x_{sep})/r_t$	f (Hz)				St				St*			
	$m = 0$		$m = 1$		$m = 0$		$m = 1$		$m = 0$		$m = 1$	
	DB	TIC	DB	TIC	DB	TIC	DB	TIC	DB	TIC	DB	TIC
0.16	830	315	2330	996	0.057	0.038	0.16	0.12	0.10	0.13	0.29	0.40
7.03	830	315	2330	996	0.057	0.038	0.16	0.12	0.10	0.13	0.29	0.40

T_0 is the stagnation temperature, γ the specific heat ratio, R the air constant, M_j is the fully adapted Mach number, which is a function of the nozzle pressure ratio through the isentropic relation. The length-scale D_j is computed as a function of M_j , the design Mach number M_d and the nozzle exit diameter D through the mass flux conservation

$$\frac{D_j}{D} = \left(\frac{1 + \frac{\gamma-1}{2} M_j^2}{1 + \frac{\gamma-1}{2} M_d^2} \right)^{\frac{\gamma+1}{4(\gamma-1)}} \left(\frac{M_d}{M_j} \right)^{1/2}. \quad (6.15)$$

Bearing in mind the picture of the wall-pressure power spectral densities (Fig. 6.7(a) and 6.8(a)), we see in Fig. 6.11 (a) that the high energy peaks characterising the shock region, at 833 Hz ($St = 0.057$) for the dual-bell nozzle and at 315 Hz ($St = 0.038$) for the TIC nozzle, belong to the symmetric mode. In the dual-bell case, the zeroth mode maintains its importance along the nozzle, while an energy decrease can be observed in the TIC case, Fig. 6.11 (c), coherently with the contours in Fig. 6.8a. As far as the asymmetric mode is concerned, we see in Fig. 6.11 (b) and (d) that the dual-bell shows some energy around ≈ 2300 Hz ($St = 0.16$) and that this peak persists downstream. The same picture appears for the TIC case, but with a much higher energy contribution: near the shock it appears a clear tone at approximately 1 kHz ($St = 0.12$). Moving downstream, the peak at $St = 0.12$ is still the most important but now some energy appears, as in the dual-bell case, at higher frequencies (around $St \approx 0.6$), indicating the presence of the asymmetric mode in the turbulent shear layer. As already shown by Baars et al. [42], Jaunet et al. [92] and Martelli et al. [95] it seems clear that the flow separation in a TIC nozzle is characterised by a shock movement which is mainly symmetric (piston-like oscillation) but with some energy present in the antisymmetric mode. This last mode, together with the higher ones, characterises also the detached shear layer, as shown by its footprint on the wall-pressure signature. This scenario is quite different from that observed in the dual-bell case, where the energy of the anti-symmetric mode is almost negligible with respect to that of the symmetrical one. All the peaks frequencies and St numbers of Fig. 6.11 are reported in Table 6.3. It is also adopted a modified Strouhal number $St^* = f \frac{L}{U_j}$, where L is the distance between the mean separation point and the nozzle exit plane as defined before. From the data reported in the table it can be seen that L is, as expected, a better length scale for the acoustic resonance and in fact, the peak St^* 's for the $m = 0$ mode are very similar for the two nozzles. On the contrary, it seems that D_j is a better length scale for the antisymmetric mode and now the St 's are closer.

The very low energy content of the first azimuthal mode in the dual-bell nozzle, with respect to the TIC case, is an indication that the dual bell working in sea-level mode at the present NPR should not develop a significant level of side loads. Jaunet et al. [92] and Martelli et al. [95] speculated

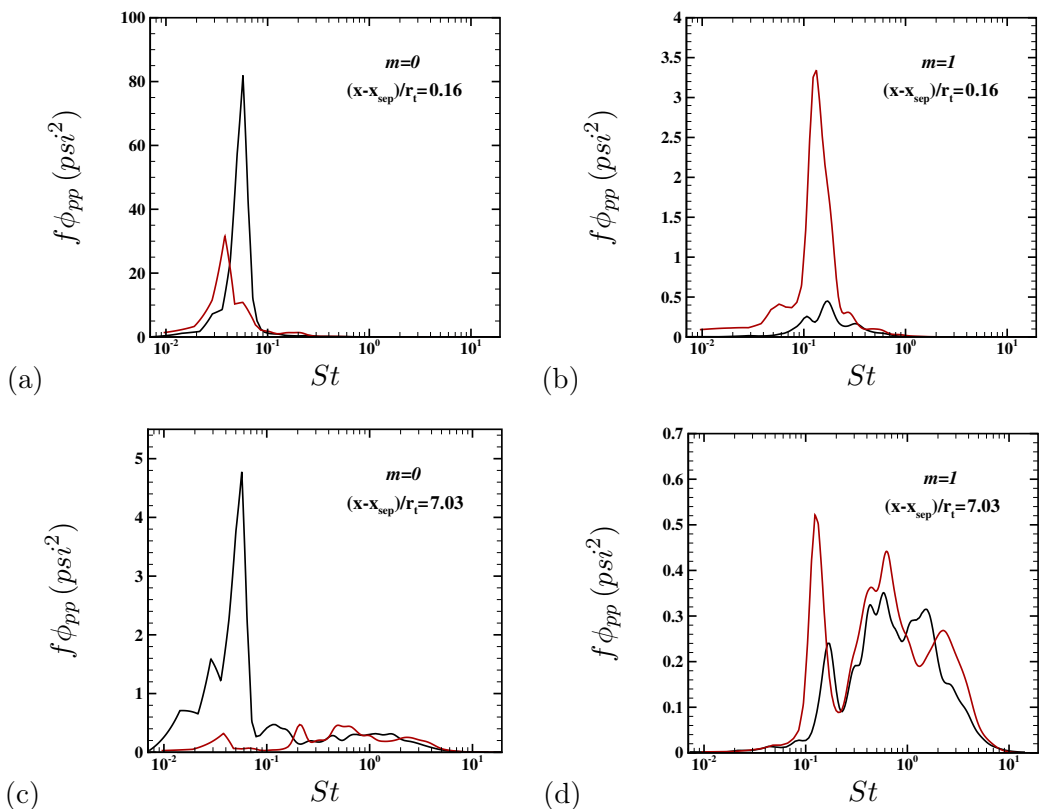


Figure 6.11: Premultiplied spectra of the zeroth (left) and first (right) Fourier azimuthal mode at $x - x_{sep} = 0.16r_t$ (a,b) and $7.03r_t$ (c,d). The black solid line refers to the dual nozzle while the red solid one to the TIC. For visualization purposes, different scales are applied to the various figures

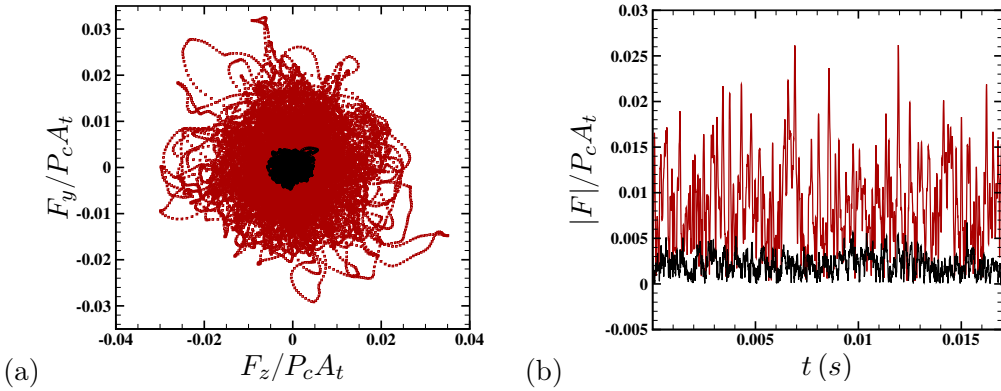


Figure 6.12: Comparison between dual-bell and TIC nozzles of the time distribution of the side-loads components F_y and F_z (a) and magnitude $|F|$ (b). The black symbols and solid line refer to the dual-bell nozzle while the red symbols and solid line to the TIC.

the existence of a screech-like mechanism inside conventional nozzles, with free shock separation, associated to this antisymmetric mode. Martelli et al. [95] proposed a path for the feedback loop, involving the downstream propagation of hydrodynamic instabilities along the shear layers and in the nozzle core downstream the Mach disk and the upstream traveling of the acoustic waves, generated by the interaction of the vortices with the shock cells, in the subsonic turbulent recirculating region inside the nozzle. Indeed, according to Powell [4, 5], every aeroacoustic resonance in high-speed jets can be decomposed into four main processes: i) the downstream propagation of energy through hydrodynamic instabilities, ii) an acoustic generation process in which the downstream perturbations are converted into upstream perturbations, iii) the upstream propagation of these disturbances, iv) the generation of new hydrodynamic instabilities through the forcing of a sensitive point excited by the upstream acoustic waves (the nozzle lip in external screech). The last process is generally called receptivity process [1]. In the TIC nozzle, this process involves the forcing of the separation line and of the separation shock, which induces the generation of a new hydrodynamic instability. In the dual-bell nozzle the antisymmetric mode is only slightly excited due to the presence of the inflection point that anchors the separation shock and constrains its movement. In particular, the inflection point induces the shock to move symmetrically, thus modifying the efficiency of the receptivity process (η_r) of the feedback loop, which hampers the generation of the first azimuthal mode. A quantitative analysis and comparison of the side-loads generation in the dual-bell and TIC nozzles is reported in the following section.

6.3.4 Aerodynamic loads distribution

The wall-pressure distribution is integrated along the nozzle wall (longitudinal and azimuthal direction) to obtain the time distribution of the side-loads components (F_y and F_z) and magnitude ($|F| = \sqrt{F_y^2 + F_z^2}$), which are reported in Fig. 6.12. The thrust and side-loads components are calculated by integration of the wall-pressure field as

$$F_x(t) = \int_{S_{nozzle}} [p_a - p_w(t, x, \theta)] \cdot n_x dS, \quad (6.16)$$

$$F_y(t) = \int_{S_{nozzle}} [p_a - p_w(t, x, \theta)] \cdot n_y dS, \quad (6.17)$$

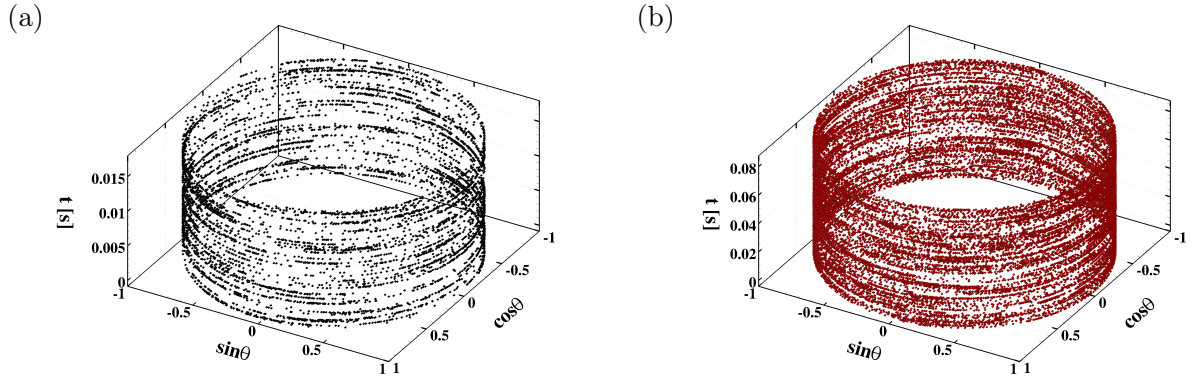


Figure 6.13: Time history of side-loads direction: (a) Dual-Bell and (b) TIC nozzle.

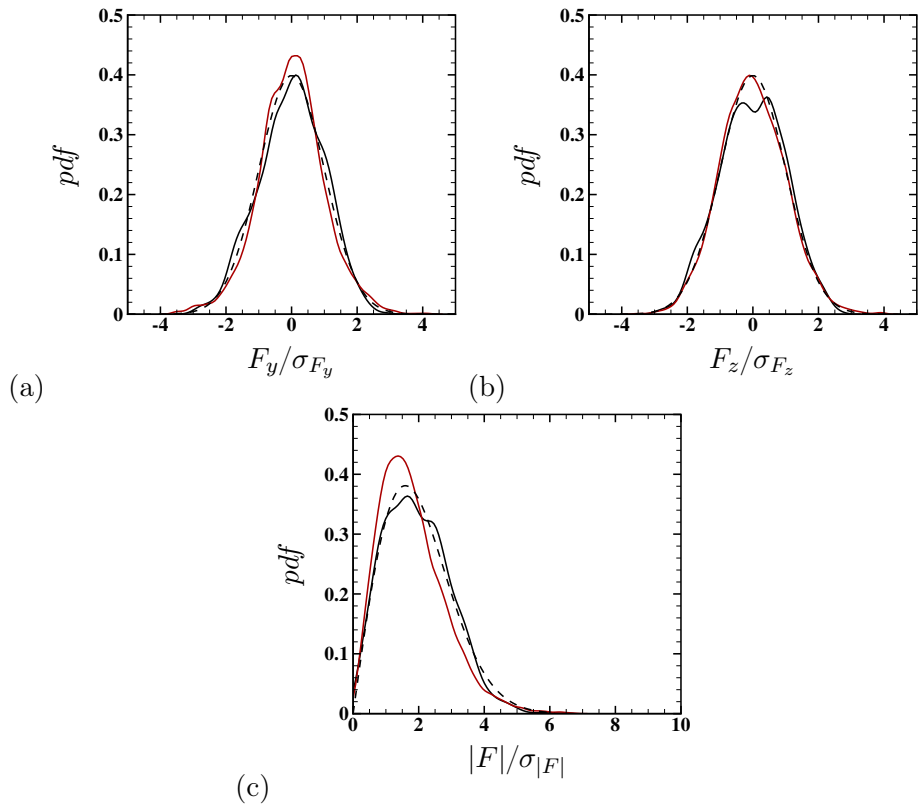


Figure 6.14: Comparison between the dual-bell and TIC nozzles of the probability density function of the side-loads components (a,b) and magnitude (c). Black solid lines represent the dual-bell nozzle, the red solid lines represent the TIC nozzle while the black dashed line is the theoretical distribution.

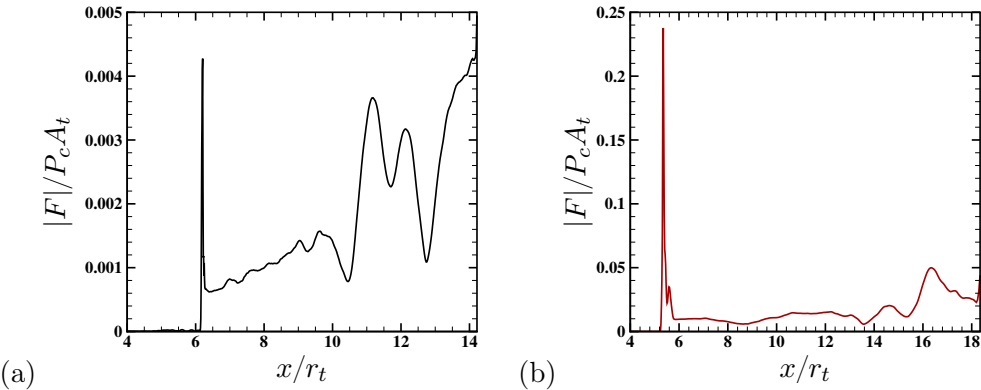


Figure 6.15: Evolution along the x-axis of the side-loads magnitude averaged in time for (a) the dual-bell and (b) TIC nozzle. For visualization purposes, different scales are applied to the figures

$$F_z(t) = \int_{S_{nozzle}} [p_a - p_w(t, x, \theta)] \cdot n_z dS. \quad (6.18)$$

The figures highlight that the side-loads components oscillate around the zero mean value and have a randomic distribution in time. Consistently with the previous discussion on the energy of the asymmetric $m = 1$ mode, the magnitude of the aerodynamic side loads in the TIC nozzle is found to be remarkably higher than that observed in the dual-bell nozzle. The experimental side-loads time history is not available from Verma et al. [65], therefore, the numerical results are compared with the experimental data of Génin and Stark [58], where a test campaign on a similar subscale dual-bell nozzle (named DB2) was performed. This nozzle has a slightly different area ratio of the second bell ($\epsilon_e = 24$) and a different inflection angle ($\alpha_i = 5^\circ$). The simulation results show an averaged value of the side loads of 3.26 N, which well agrees with the value of 3.42 N obtained by the experiments. The time evolution of the side-loads vector direction ($\cos(\theta)$, $\sin(\theta)$) with respect to the z axis, is reported in Fig. 6.13 as a function of time. This figure shows that the side loads have not a preferential direction in the space, similarly to the results obtained by Deck and Guillen [88], who performed a numerical campaign to predict side loads in a sub-scale TIC nozzle. The probability density functions of $F_y(t)$, $F_z(t)$ and $|F|(t)$ are shown in Fig. 6.14 (a), (b) and (c) respectively for both nozzles. It clearly appears that the side-loads components are two independent normal random variables with zero mean value and the same standard deviation, thus indicating that their distribution is Gaussian. Indeed, the numerical distribution well fit the theoretical Gaussian one. As a consequence, the probability distribution of $|F|$, Fig. 6.14(c), is a Rayleigh distribution, as shown by Dumnov [78], who studied the experimental statistical distribution of side loads in a sub-scale nozzle.

To better characterize the origin of the aerodynamic side loads, and identify the nozzle regions that most contribute to their generation, the axial distribution of the side-loads magnitude averaged in time is shown in Fig. 6.15 for the dual-bell and the TIC geometry. These profiles have been obtained by integrating the wall-pressure, at each streamwise location, along the azimuthal direction and averaging in time. As far as the dual bell is concerned, Fig. 6.15(a) shows a peak in correspondence of the separation-shock location, followed by a gradual increase until the end of the second bell, associated with the development of the turbulent shear layer. This behaviour is in close agreement with the observations made on the spatial distribution of the first Fourier azimuthal

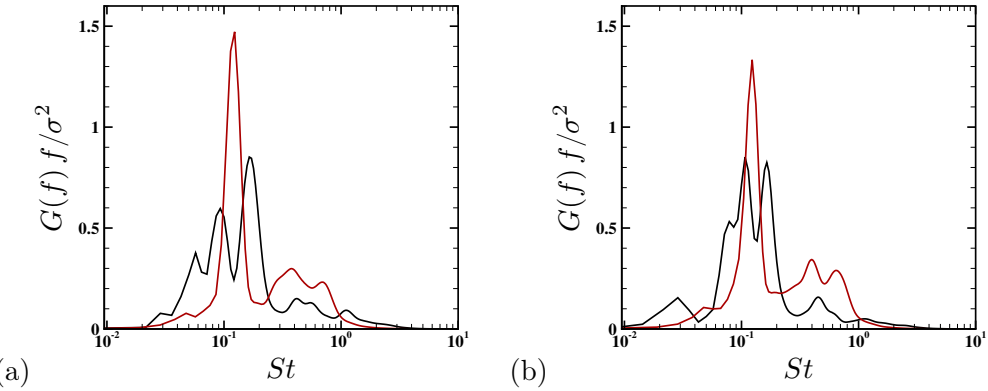


Figure 6.16: Normalized premultiplied power spectral densities of the side-loads components F_y (a) and F_z (b). The black solid line refers to the DB nozzle while the red solid one to the TIC.

mode. The axial distribution of the side-loads in the TIC nozzle, Fig. 6.15 (b), further confirms the larger intensity of the lateral force for this type of nozzle. In this case, a strong peak is found in the proximity of the shock location, whereas a flat contribution is observed in the divergent section of the nozzle. It is worth to notice that these trends are qualitatively similar to that obtained by Deck and Guillen [88]. The Fourier spectra of the lateral forces F_y and F_z for both nozzles are reported in Fig. 6.16. It is clearly visible that both components in the TIC nozzle are characterized by a predominant peak at a Strouhal number approximately equal to 0.12, corresponding as expected to the peak frequency of the first Fourier azimuthal mode (see Table 6.3). The dual-bell nozzle shows a picture a little bit different: the spectrum of F_y is characterized by a rather large bump with the highest peak centered at $S_t = 0.16$, that is the characteristic peak frequency of the anti-symmetric mode, while the spectrum of F_z shows a bump split in two peaks at $S_t = 0.1$ and $S_t = 0.16$. The difference in the behavior is most probably due to the fact that the anti-symmetric mode is less energetic and coherent than the one characterizing the TIC nozzle. Finally, the dimensionless longitudinal component of the force $F_x/(p_c A_t)$, corresponding to the thrust coefficient, is reported in Fig. 6.17(a) for both geometries. The two nozzles are characterised by similar levels of thrust oscillation. In particular, for the DB nozzle the fluctuation of the thrust coefficient from its mean value reaches a maximum departure of 1.37% and a standard deviation value of 0.74%. For the TIC nozzle these fluctuations have a standard deviation of 0.42% with a maximum departure of 1.02%. The value of the thrust coefficient fluctuation varies depending on several factors, including the operating regime. This behaviour can be observed for example in the study of Proschanka et al. [66] on a sub-scale dual-bell nozzle, where the standard deviation of the thrust coefficient, calculated with respect to the NPR, is around 2.8%. This is valid both in the up-ramping and down-ramping process. A similar value is obtained by Moríñigo and Salvá [48] for a sub-scale J-2S TOC nozzle, where the deviation of the thrust oscillation amplitude is around 2%. The spectra of the thrust coefficients reported in Fig. 6.17 (b) show that all the energy is concentrated at the frequency corresponding to the acoustic resonance given by the piston-like shock movement, $St^*=0.10$ and 0.13 for the dual-bell and TIC nozzle, respectively. This implies that, in the design phase, the level of vibrations at lift-off and during the first part of the trajectory (first operating mode), that are detrimental for the engine structure and the payload, must be carefully addressed.

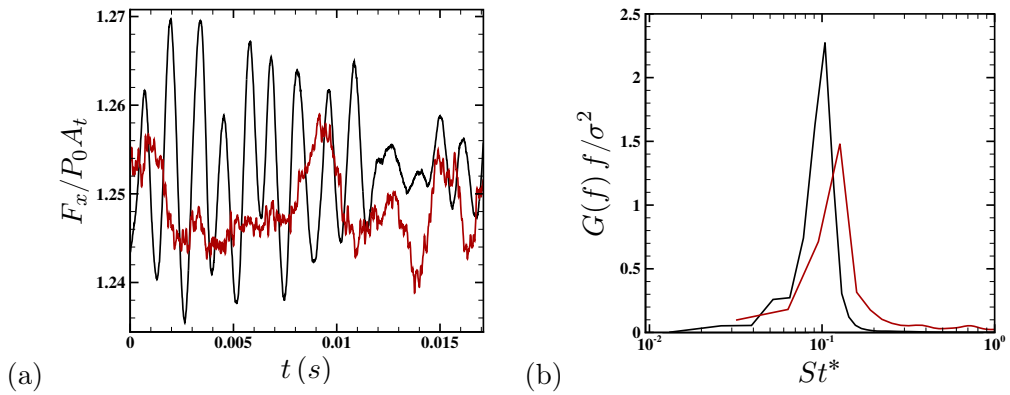


Figure 6.17: (a) Time history of the thrust coefficient $F_x/(p_0 A_t)$ for the dual-bell and TIC nozzles and (b) corresponding premultiplied power spectral densities. The black solid line denotes the dual-bell nozzle, the red solid line refers to the TIC nozzle.

Chapter 7

Conclusions and future work

High-fidelity numerical simulations of compressible turbulent flows for space applications have been carried out for the purpose of predicting aeroacoustic resonance phenomena. The flow instabilities developing inside SRMs and the aerodynamic side-loads generated by Shock-Wave/Boundary-Layer Interaction (SWBLI) in rocket nozzles during the ascent phase of space launchers are a consequence of these aeroacoustic resonance phenomena and lead to possible damage of the payload and of the launcher structure. For this reason, a laboratory scale SRM and a sub-scale rocket nozzle have been investigated, which are respectively the ONERA C1xb SRM and the Dual-Bell nozzle. The importance of studying the flow unsteadiness in SRMs is related to the fact that the possible coupling between the hydrodynamic instabilities and the acoustic resonant modes can trigger pressure and thrust oscillations, which can damage the motor structures, the thrust vector control system and the payload comfort. On the other hand, the importance of studying the SWBLI phenomenon in over-expanded rocket nozzles lies in the fact that the non-symmetric unsteady flow conditions can yield global off-axis forces, the side-loads, that can adversely affect the structural integrity of the nozzle and decrease its lifespan and reusability. Although several studies in the last decades, a clear physical understanding of the flow unsteadiness is still lacking for both cases and a correct evaluation of the aeroacoustic feedback loop is crucial in the design phase of these systems. The experiments suffer from the lack of flow measurements inside SRMs and rocket nozzles, due to the challenging flow conditions and the absence of optical access, and also for this reason numerical simulations represent an important complementary tool to approach this study. From the numerical point of view, it is worth noticing that the challenge in simulating these flows in a wide range of Mach numbers, at high Reynolds numbers and in the presence of walls is to adequately simulate the interaction of shock waves with large and small scale turbulence, the transition to turbulence and all the phenomena associated with the aeroacoustic feedback loop.

The coupling between vortex shedding and pressure oscillations in a small-scale solid rocket motor has been investigated through a 3D implicit large-eddy simulation of the single-phase, compressible Navier-Stokes equations. The simulation reproduced the ONERA C1xb SRM geometry at a firing time corresponding to a 3 mm grain burned layer, a configuration close to ignition for which all previous 2D axi-symmetric computations presented in literature failed to predict the level of pressure oscillations, leading to a remarkable overestimate with respect to the experimental data. We found that the present 3D ILES provides a significant improvement in the prediction of the

wall-pressure signature, and an excellent agreement was obtained for the distribution of the root-mean-square wall-pressure fluctuations along the whole motor wall. This behavior was attributed to the capability of the full-scale 3D approach to capture the break-up and transition to fine-scale turbulence of the shear-layer rollers shed by the grain edge in the motor chamber, thus confirming the original speculations made by Lupoglazoff and Vuillot [17]. The main effect of turbulence is to disrupt the coherence of the vortices seen in the axisymmetric computations. In fact, these vortices, impinging on the nozzle wall at the end of the motor, produce the occurrence of large pressure disturbances travelling upstream and inducing the large level of pressure oscillations obtained in the 2D computations. The frequency spectra of the wall-pressure fluctuations show that first three longitudinal acoustic modes ($L_1 = 724$ Hz, $L_2 = 1448$ Hz, $L_3 = 2172$ Hz) dominate the pressure signal at the head end of the motor. In the middle of the chamber, where the shear layer detaches from the propellant edge, the second axial mode becomes relevant. A dominant peak locked on the third axial mode is found at $x \approx 0.49$ m that, as also shown by the frequency spectrum of the axial velocity in the shear layer, corresponds to the vortex shedding frequency in the motor chamber. This coupling on the third mode between pressure oscillations and vortex shedding was observed experimentally by Lupoglazoff and Vuillot [17], and it is also supported by the acoustic feedback model developed by Rossiter [167], which provides a vortex shedding frequency $f_{AM} \approx 2143$ Hz in excellent agreement with the frequency computed from ILES (2163 Hz). The results of the present SRM study demonstrate that, at least for the flow conditions and SRM configuration considered, characterized by high shear levels, the correct prediction of the aeroacoustic feedback loop and of the pressure oscillation level in SRMs with corner vortex shedding must rely on the use of high-fidelity 3D simulations, capable of capturing the energy cascade process and the development of fine-scale turbulent structures in the motor chamber.

Subsequently, the aeroacoustic resonance phenomenon has been studied through a calibrated delayed detached eddy simulation of a dual-bell nozzle working in an over-expanded condition with the flow separation anchored at the wall-inflection point. The main goal of the investigation was to figure out the effectiveness of the wall discontinuity as a flow-separation control device for the aeroacoustic feedback mechanism occurring inside the nozzle itself. The study has been conducted by analyzing the spectral content of the wall-pressure signature, with the purpose of evaluating the aerodynamic loads and comparing them with those experienced by a truncated ideal contour (TIC) nozzle [95]. The latter is a well known conventional nozzle that suffers the onset of side loads when operating with an internal flow separation, because of the aeroacoustic coupling developing inside it. The dual-bell nozzle geometry has been specified following the experimental work of Verma et al. [65], whose data have been used to assess the accuracy of the simulation. The analysis of the unsteady wall-pressure signals showed a good agreement of the mean wall pressure and the standard deviation of the pressure fluctuations along the nozzle with the experimental data, although the standard deviation peak at the shock location seemed to be slightly over-predicted. The spectral analysis highlighted the presence of an acoustic tone at ≈ 0.8 kHz, associated with the shock motion. This tone appeared to persist all along the nozzle wall, as also confirmed by the experimental trend, and it was found to be an acoustic resonance, its frequency being associated with a one-quarter standing wave that develops between the mean separation shock location and the nozzle lip. Also the TIC nozzle was characterized by a strong tone in the low frequency range, even if its energy

decreases along the nozzle wall. Both nozzles also showed the presence of oscillation energy in the high frequency range (between 10 kHz and 100 kHz), originated by the turbulent detached shear layer. The analysis carried out in the wavenumber-frequency space revealed that the low-frequency peaks of both geometries are associated to the zero-th azimuthal Fourier mode, which is symmetric and whose energy contribution is dominant in the total fluctuation energy. This piston-like (or breathing) symmetric mode is responsible for the generation of thrust fluctuations, as also seen in the C1xb SRM case. The second important contribution came from the first antisymmetric mode, which is the only one to be non-symmetric and capable of triggering lateral forces. In particular, the TIC nozzle was characterized by a tone in the intermediate frequency range, (≈ 1 kHz, $St=0.12$), as already shown in literature [42, 92, 95]. This characteristic frequency reasonably agrees with the empirical correlation for the characteristic frequency of the screech phenomenon [175], suggesting the presence of a feedback loop similar to that observed for overexpanded external jets. A similar agreement was also displayed by the experimental results of Jaunet et al. [92]. However, those authors did not find any trace of the screech tone in the external ambient, so they speculated the existence of a screech-like mechanism inside the nozzle sustained by the presence of the internal subsonic flow region downstream of the Mach disk, which may provide a support for possibly upstream propagating waves. From the numerical findings of Martelli et al. [95], the peak at approximately 1000 Hz in the spectra results strictly linked to the intermittent vortex shedding activity of the Mach disk. The vortices emitted from the Mach disk propagate in the streamwise direction and interact with the second shock cell, irradiating acoustic waves able to travel upstream in the outer subsonic region. These perturbations excite new instabilities of the shear layer and of the shock system, closing a feedback-loop. The first Fourier azimuthal mode is instead only slightly excited in the dual-bell nozzle with a peak at approximately 2300 Hz ($St=0.16$). Its energy is almost negligible with respect to the zero-th mode and much lower with respect to the TIC case. Therefore, the triggering of the antisymmetric mode seems to be suppressed by the presence of the inflection point, which mainly forces a symmetric shock movement, altering the receptivity process of the separation line to the upstream travelling acoustic disturbances. The evaluation of the aerodynamic lateral forces revealed a distribution which is qualitatively similar for both geometries and approximately equal to the Rayleigh distribution, as found by Dumnov [78]. The mean magnitude of the lateral force in the dual bell well agrees with the experimental value of Génin and Stark [58], and it is an order of magnitude lower than the side loads found in the TIC nozzle. On the other hand, the fluctuation of the thrust coefficient is similar in both cases and of the order of 1% with respect to the mean value. This aspect should be considered in the design phase and carefully evaluated to avoid annoying vibrations on the payload and engine structure.

Possible future developments of the present work could be related to the study of the aeroacoustic resonance phenomenon in different systems and/or configurations and through the implementation of different high-fidelity numerical methods and schemes. From the SRMs point of view, the study could be extended to study full-scale SRMs or flow configurations characterized by parietal vortex shedding. This issue, as well as the investigation of other important topics as the role of combustion noise on the vortex shedding triggering or two-phase flow effects on acoustic oscillations, are left for future studies. Concerning the rocket nozzles, a more extensive comparison spanning a wider range of parameters in terms of NPRs, wall-inflection angles and second-bell design wall-

pressure gradients, could be certainly interesting for a future investigation. Moreover, the study of a way of controlling the SWBLI, as, for example, a secondary transverse injection into the divergent section of the nozzle, could be a possible development in the subject matter of side-loads reduction.

Appendix A

Transforms

A.1 Fourier Transform

In this section a brief reference to the fundamental definitions, properties and theorems of the Fourier transforms will be provided. A more complete description is given in [111] and in other standard texts on the theme. The following introduction is given for a function in the generic variable x and in the generic transformed variable k . These two can be interpreted both as time and angular frequency or as space coordinate and wavenumber in a certain direction.

A.1.1 Transform and Inverse Transform

The Fourier transform of a given function $f(x) : \mathbb{R} \rightarrow \mathbb{R}$ is

$$\hat{f}(k) = \mathcal{F}\{f(x)\} := \frac{1}{2\pi} \int_{\mathbb{R}} f(x)e^{-ikx} dx \quad (\text{A.1})$$

whereas, the inverse Fourier transform is

$$f(x) = \mathcal{F}^{-1}\{f(x)\} := \int_{\mathbb{R}} \hat{f}(k)e^{ikx} dk \quad (\text{A.2})$$

A Fourier transform pair $(f - \hat{f})$ is formed if the necessary condition of convergence of the integrals (A.2)-(A.2) is shown.

The definition of the argument of the exponential functions in the formulas above is just conventional and certainly not unique, since for example in some books the negative exponent is in the inverse transform or the factor 2π is splitted in different portions between the transform and the inverse transform. The chosen convention is used and reported in authoritative sources as [111] and [176]. In table A.1 some example of fundamental Fourier pairs.

A.1.2 Convolution Theorem

Given two functions $f(x)$ and $g(x)$, the convolution product is defined as

$$[f * g](x) := \int_{\mathbb{R}} f(y)g(x-y)dy = \int_{\mathbb{R}} f(x-y)g(y)dy \quad (\text{A.3})$$

$f(x)$	$f(k)$
1	$\delta(k)$
$\delta(t)$	$\frac{1}{2\pi}$
$\sin(ct)$	$\frac{k^2 + c^2}{k}$
$\cos(ct)$	$\frac{k}{k^2 + c^2}$
e^{ax}	$\frac{1}{ik - a}$

Table A.1: Fourier pairs of common functions.

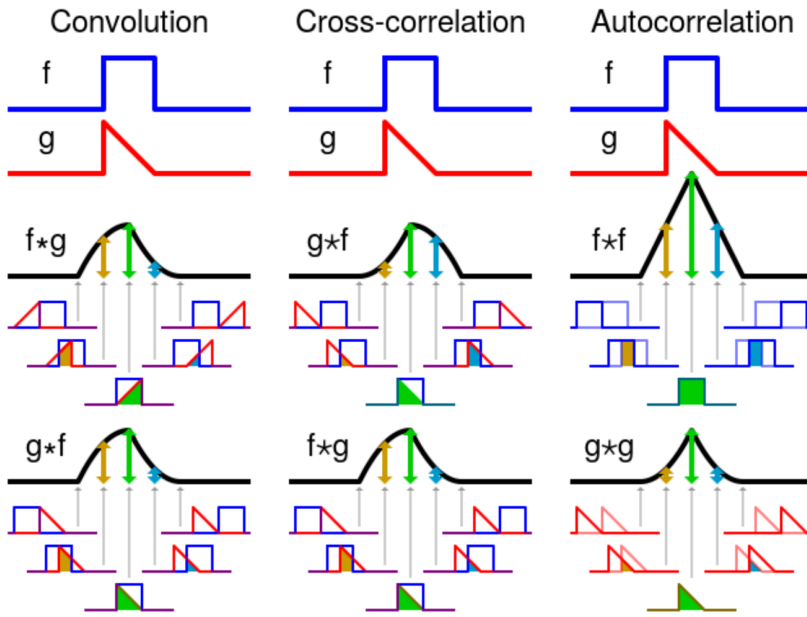


Figure A.1: A visual explanation of the convolution product and the difference between convolution and correlation.

Theorem 2 (Convolution Theorem): The Fourier transform of the convolution product between two functions $f(x)$ and $g(x)$ is given by the product of their Fourier transforms, $\hat{f}(k)$ and $\hat{g}(k)$,

$$\mathcal{F}\{[f * g](x)\} = \mathcal{F}\{f(x)\}\mathcal{F}\{g(x)\} = \hat{f}(k)\hat{g}(k) \quad (\text{A.4})$$

A.1.3 Parseval's theorem

Considering the integral of the product of two functions, that have correspondent Fourier transforms, can be useful in energy considerations about the signal. In Fourier domain, Parseval theorem is of fundamental importance in these considerations. Its generalization to non Fourier series, e.g. wavelet case, is the Plancherel theorem.

Theorem 3 (Parseval Theorem): Suppose that $f(x)$ and $g(x)$ are two square integrable function one has

$$\int_{-\infty}^{+\infty} f(t)g(t)dt = 2\pi \int_{-\infty}^{+\infty} \hat{f}(k)\hat{g}^*(k)dk \quad (\text{A.5})$$

For the case in which $f(x) = g(x)$ and hence $\hat{f}(k) = \hat{g}(k)$, the interpretation of this form of the theorem is that the total energy of a signal can be calculated by summing power-per-sample across time or spectral power across frequency or power spectral density ($PSD(k)$)

$$\int_{-\infty}^{+\infty} f(t)^2 dt = 2\pi \int_{-\infty}^{+\infty} \hat{f}(k) \hat{f}^*(k) dk = 2\pi \int_{-\infty}^{+\infty} \hat{f}(k)^2 dk = \int_{-\infty}^{+\infty} PSD(k) dk \quad (\text{A.6})$$

A.1.4 Basic properties

Below some essential properties of Fourier transforms are reported without demonstration.

Translation in x -space The Fourier transform of a translated function in x -space is given by the product of $\hat{f}(k)$ with an exponential function

$$f(x - y) \rightarrow \hat{f} e^{-iky} \quad (\text{A.7})$$

Dilatation in x -space The Fourier transform of a dilatated function in x -space, with $a > 0$, is

$$f(x/a) \rightarrow a\hat{f}(ak) \quad (\text{A.8})$$

Real $f(x)$ functions If a function $f(x)$ is real, then one can say that

$$\hat{f}(-k) = \hat{f}^*(k) \quad (\text{A.9})$$

where the * symbol indicates the complex conjugation operation.

If a function is purely real and even, its transform is a real even function; if a function is purely real and odd, its transform is purely imaginary and odd.

Product in x -space The Fourier transform of the product of two functions in x -space is given by the convolution of the transforms of the two functions

$$f(x)g(x) \rightarrow \int_{\mathbb{R}} \hat{f}(\chi) \hat{g}(k - \chi) d\chi \quad (\text{A.10})$$

Derivation in x -space The Fourier transform of n -derivative in x -space is given by

$$\frac{d^n}{dx^n} f(x) \rightarrow (ik)^n \hat{g}(k) \quad (\text{A.11})$$

A.1.5 Extension to the n -dimensional Case

The definitions explained above can be extended for a function $f(x_i)$ with a variable $x_i \in \mathbb{R}^n$, defining the wavenumber vector $k_i \in \mathbb{R}^n$. The Fourier transform is given by

$$\hat{f}(k_i) = \mathcal{F}\{f(x_i)\} := \left(\frac{1}{2\pi}\right)^n \int_{\mathbb{R}^n} f(x_i) e^{-ik_i x_i} dx_i \quad (\text{A.12})$$

and the inverse Fourier transform is

$$f(x_i) = \mathcal{F}^{-1}\{\hat{f}(k_i)\} := \int_{\mathbb{R}^n} \hat{f}(k_i) e^{ik_i x_i} dk_i \quad (\text{A.13})$$

Appendix B

Numerical Issues

The following discussion, inspired by a lecture's presentation of the Professor Chi-Wang Shu of the Brown University [177], is just an intuitive and very approximate explanation of some numerical concepts introduced in ch.3. For the sake of simplicity just the one-dimensional hyperbolic conservation law will be considered

$$u_t + f(u)_x = 0 \quad (\text{B.1})$$

which can have discontinuous solutions even if the initial condition is smooth and where the speed of sound is defined as

$$a(u) = f'(u) \quad (\text{B.2})$$

Discretizing the computational domain into cells $I_i = [x_{i-1/2}, x_{i+1/2}]$, in which the cell sizes Δx_i , it is possible to define the computational variables as the cell averages

$$\bar{u}_i = \frac{1}{\Delta x_i} \int_{x_{i-1/2}}^{x_{i+1/2}} u(x) dx \quad (\text{B.3})$$

A finite volume scheme approximates (B.1) in its integral form, or

$$\frac{d}{dt} \bar{u}_i + \frac{1}{\Delta x_i} (f(u_{i-1/2}) - f(u_{i+1/2})) = 0 \quad (\text{B.4})$$

Given (B.4), a form to express $f(u)$ is needed and a reconstruction procedure approximates $u_{i\pm 1/2}$.

With regard of the expression of the flux function f , Lax-Friedrichs flux splitting has been named in chapter 4, whereas concerning approximation of $u_{i\pm 1/2}$, WENO reconstruction has been used in the artificial diffusion.

B.1 Lax-Friedrichs Flux Splitting

The basic idea of the flux splitting procedure is the mathematical decomposition of the flux $f(u)$ in two part, the first, $f^+(u)$, being associated to a positive sound speed and so connected to waves that propagates towards positive coordinate, and the second, $f^-(u)$, associated to negative speed of sound and waves propagating towards negative x , or

$$f(u) = f^+(u) + f^-(u), \quad a^+(u) = \frac{df^+}{du} \geq 0, \quad a^-(u) = \frac{df^-}{du} < 0, \quad \forall u \quad (\text{B.5})$$

Being $\hat{f}_{i+1/2}^+$ the numerical flux that uses a "+"-type upwind scheme applied to $f^+(u)$ and $\hat{f}_{i+1/2}^-$ the result of the application of a "-"-type upwind scheme applied to $f^-(u)$ the total numerical flux can be expressed as the sum of the two

$$\hat{f}_{i+1/2} = \hat{f}_{i+1/2}^+ + \hat{f}_{i+1/2}^- \quad (\text{B.6})$$

The Lax-Friedrichs flux splitting is based on the decomposition

$$f^\pm(u) = \frac{1}{2}(f(u) \pm \alpha u), \quad \alpha = \max_u |f'(u)| \quad (\text{B.7})$$

where α is a parameter indicating the maximum possible value of the sound speed on all the assumed values at a certain time instant.

Other possible flux splitting procedures exist, e.g. Steger&Warming flux splitting.

B.2 WENO Reconstruction

A typical reconstruction procedure consists of choosing consecutive cells near $x_{i+1/2}$, e.g. the two neighbours of $x_{i+1/2}$: I_i and I_{i+1} . These cells form the so called stencil of the reconstruction.

The reconstruction procedure seeks a polynomial function $p(x)$ whose cell average over each cell I_i in the stencil agrees with the given \bar{u}_i . Having defined the coefficients of the polinomy it is possible to take $u_{i+1/2} = p(x_{i+1/2})$.

Entering in the details for a reconstruction that uses \bar{u}_{i-1} , \bar{u}_i and \bar{u}_{i+1} values with a second order polynomial $p(x)$, one imposes

$$\frac{1}{\Delta x_{i-1}} \int_{x_{i-3/2}}^{x_{i-1/2}} p(x) dx = \bar{u}_{i-1} \quad (\text{B.8a})$$

$$\frac{1}{\Delta x_i} \int_{x_{i-1/2}}^{x_{i+1/2}} p(x) dx = \bar{u}_i \quad (\text{B.8b})$$

$$\frac{1}{\Delta x_{i+1}} \int_{x_{i+1/2}}^{x_{i+3/2}} p(x) dx = \bar{u}_{i+1} \quad (\text{B.8c})$$

and the approximation is

$$u_{i+1/2} = p(x_{i+1/2}) \quad (\text{B.9})$$

where $u_{i+1/2}$ can be written as a linear combination of the given cell averages because the procedure is linear.

Given the presence of possible discontinuities in the field, an ideal numerical scheme should be high order accurate in smooth regions and (essentially) non-oscillatory in correspondance of shocks. However the Godunov theorem states that these two properties cannot be fulfilled together by a linear schemes (schemes that are linear to (B.1) with constant $f'(u)$).

WENO schemes provide an example of a nonlinear scheme, where the nonlinearity of the algorithm is only at the stage of choosing the stencils used in the reconstruction procedure.

The first procedure that was thought to avoid stencil which crosses the discontinuity, so as not to have spurious oscillations, was the Essentially Non-Oscillatory (ENO) reconstruction that uses

a uniform high order polynomy and a locally adaptive stencil, where among several candidates only one is chosen according to local smoothness.

Instead of ENO, WENO does not use a lonely stencil, but a linear combination of all candidate stencil with weights on each candidate that are a nonlinear function of the cell averages. This method provides a cleaner programming with no "if" statements in the stencil choosing process and some accuracy advantages over ENO.

The practical steps are:

1. repetition of the general procedure described before for reconstruction for all the R substencils (fig.B.1) in order to find the substencils' approximations $u_{i+1/2}^{(r)}$ with $r = 1, \dots, R$.
2. finding of the nonlinear weights w_r such that

$$u_{i+1/2} = \sum_{r=1}^R w_r u_{i+1/2}^{(r)} \quad (\text{B.10})$$

is both accurate in smooth region and non-oscillatory for shocks. If $u(x)$ is smooth in all the substencils the nonlinear weights are very similar to the linear weights γ_r that verify an homologous relation to (B.10) that is accurate but oscillatory in the shock regions. If $u(x)$ has a discontinuity in a certain substencil S_k , then w_k is very small.

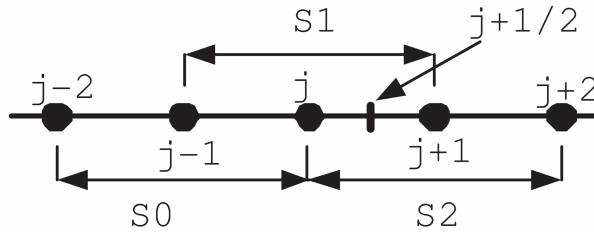


Figure B.1: Three substencils for the reconstruction at $x_{j+1/2}$ using three cells in each stencil. [177]

A robust choise of the nonlinear weights [139] is

$$w_r = \frac{\tilde{w}_r}{\sum_{k=1}^R \tilde{w}_k}, \quad \tilde{w}_r = \frac{\gamma_r}{(\epsilon + \beta_r)^2} \quad (\text{B.11})$$

where $\epsilon = 10^{-6}$ typically and the smoothness indicator β_k is a measure of smoothness of $u(x)$ in the substencil S_r .

B.3 Runge-Kutta time-integration

Runge-Kutta methods are a family of implicit and explicit iterative methods used in temporal discretization for the approximate solutions of ordinary differential equations. The most widely used method is the so called RK4 (a fourth-order method, i.e. local truncation error on the order of (Δt^5)).

Let an initial value problem be specified as follows

$$y' = f(t, y), \quad y(t_0) = y_0 \quad (\text{B.12})$$

where y is a time function that the method wants to approximate during its time evolution.

The conceptual idea is derived by the Taylor series evaluated in t_{n+1} , centered in t_n , truncated at a certain order. This expression allows to calculate the value at a subsequent time respect to t_n , approximating it with the evaluation at a time t_{n+1} along the curve described by the first considered derivatives.

The Runge-Kutta methods obtains the approximation moving on a straight line, instead of the above mentioned curve, with an angular coefficient that is a linear combination of the assumed value of $f(t, y)$ in relevant points belonging to $[t_n, t_{n+1}]$.

Considering a time step $\Delta t = t_{n+1} - t_n > 0$, one has that

$$y_{n+1} = y_n + \frac{\Delta t}{6}(k_1 + 2k_2 + 2k_3 + k_4) \quad (\text{B.13})$$

with

$$k_1 = f(t_n, y_n) \quad (\text{B.14a})$$

$$k_2 = f\left(t_n + \frac{\Delta t}{2}, y_n + \Delta t \frac{k_1}{2}\right) \quad (\text{B.14b})$$

$$k_3 = f\left(t_n + \frac{\Delta t}{2}, y_n + \Delta t \frac{k_2}{2}\right) \quad (\text{B.14c})$$

$$k_4 = f(t_n + \Delta t, y_n + \Delta t k_3) \quad (\text{B.14d})$$

B.3.1 Explicit Runge-Kutta Methods

A generalization of the RK4 is given by

$$y_{n+1} = y_n + \Delta t \sum_{i=1}^s b_i k_i \quad (\text{B.15})$$

where

$$k_1 = f(t_n, y_n) \quad (\text{B.16a})$$

$$k_2 = f(t_n + c_2 \Delta t, y_n + \Delta t(a_{21} k_1)) \quad (\text{B.16b})$$

$$k_3 = f(t_n + c_3 \Delta t, y_n + \Delta t(a_{31} k_1 + a_{32} k_2)) \quad (\text{B.16c})$$

$$\vdots \quad (\text{B.16d})$$

$$k_s = f(t_n + c_s \Delta t, y_n + \Delta t(a_{s1} k_1 + a_{s2} k_2 + \dots + a_{s,s-1} k_{s-1})) \quad (\text{B.16e})$$

To specify a particular method, one needs to provide the integer s , that is the number of stages (in the code $s = 3$), the Runge-Kutta matrix a_{ij} (for $1 \leq j < i \leq s$), the weights b_i (for $i = 1, 2, \dots, s$) and the nodes c_i (for $i = 2, 3, \dots, s$).

A mnemonic device, the so called Butcher tableau, usually collects all these data in the form in tab.B.1.

	0				
c_2	a_{21}				
c_3	a_{31}	a_{32}			
\vdots	\vdots		\ddots		
c_s	a_{s1}	a_{s2}	\cdots		
0	b_1	b_2	\cdots	b_{s-1}	b_s

Table B.1: Butcher tableau for s -stages Runge-Kutta method.

Bibliography

- [1] D. E.-Mitchell. Aeroacoustic resonance and self-excitation in screeching and impinging supersonic jets—a review. *International Journal of Aeroacoustics*, 18(2-3):118–188, 2019.
- [2] A. Memmolo, M. Bernardini, and S. Pirozzoli. Scrutiny of Buffet Mechanisms in Transonic Flow. *International Journal of Numerical Methods for Heat & Fluid Flow*, 28(5):1031–1046, 2018.
- [3] K. Baskaran and K. Srinivasan. Aeroacoustic characteristics of subsonic flow from axisymmetric pipe-cavities. *Physics of Fluids*, 31(10):106107, 2019.
- [4] A. Powell. The noise of choked jets. *The Journal of the Acoustical Society of America*, 25(3):385–389, 1953.
- [5] A. Powell. On the mechanism of choked jet noise. *Proceedings of the Physical Society. Section B*, 66(12):1039, 1953.
- [6] C.D. Brown. *Spacecraft propulsion*. AIAA, 1996.
- [7] E. Cavallini. Modeling and numerical simulation of solid rocket motors internal ballistics. *Rome: Sapienza University of Rome*, 2010.
- [8] J. Anthoine. Experimental and numerical study of aeroacoustic phenomena in large solid propellant boosters. 2000.
- [9] M.K. King. A model of erosive burning of composite propellants. *Journal of Spacecraft and Rockets*, 15(3):139–146, 1978.
- [10] F. Vuillot. Vortex-shedding phenomena in solid rocket motors. *Journal of Propulsion and Power*, 11(4):626–639, 1995.
- [11] G.I. Taylor. Fluid flow in regions bounded by porous surfaces. *Proceedings of the Royal Society of London. Series A. Mathematical and Physical Sciences*, 234(1199):456–475, 1956.
- [12] R. Dunlap, A.M. Blackner, R.C. Waugh, R.S. Brown, and P.G. Willoughby. Internal flow field studies in a simulated cylindrical port rocket chamber. *Journal of Propulsion and Power*, 6(6):690–704, 1990.
- [13] J. Griffond, G. Casalis, and J.P. Pineau. Spatial instability of flow in a semiinfinite cylinder with fluid injection through its porous walls. *European Journal of Mechanics-B/Fluids*, 19(1):69–87, 2000.

- [14] Y. Fabignon, J. Dupays, G. Avalon, F. Vuillot, N. Lupoglazoff, G. Casalis, and Prévost M. Instabilities and pressure oscillations in solid rocket motors. *Aerospace Sci. Tech.*, 7:191–200, 2003.
- [15] J. Dupays, M. Prévost, P. Tarrin, and F. Vuillot. Effects of Particulate Phase on Vortex Shedding Driven Oscillations in Solid Rocket Motors. In *32nd Joint Propulsion Conference and Exhibit*, page 3248, 1996.
- [16] N. Lupoglazoff and F. Vuillot. Numerical simulation of vortex shedding phenomenon in 2D test case solid rocket motors. In *30th Aerospace Sciences Meeting and Exhibit*, page 776, 1992.
- [17] N. Lupoglazoff and F. Vuillot. Comparison between firing tests and numerical simulation of vortex shedding in a 2-D test solid motor. In *23rd Fluid Dynamics, Plasmadynamics, and Lasers Conference*, page 3066, 1993.
- [18] G.A. Flandro and H.R. Jacobs. Vortex generated sound in cavities. AIAA Paper 73-1014, 1973.
- [19] J. Anthoine, J.-M. Buchlin, and A. Hirschberg. Effect of nozzle cavity on resonance in large SRM: theoretical modeling. *Journal of Propulsion and Power*, 18(2):304–311, 2002.
- [20] J. Anthoine, J.-M. Buchlin, and J.-F. Gué. Effect of nozzle cavity on resonance in large SRM: numerical simulations. *Journal of Propulsion and Power*, 19(3):374–384, 2003.
- [21] F. Stella and F. Paglia. Pressure oscillations in solid rocket motors: Numerical study. *Aerospace Science and Technology*, 15:53–59, 2011.
- [22] G.A. Flandro and J. Majdalani. Aeroacoustic Instability in Rockets. *AIAA journal*, 41(3):485–497, 2003.
- [23] S. Balachandar, J.D. Buckmaster, and M. Short. The generation of axial vorticity in solid-propellant rocket-motor flows. *Journal of Fluid Mechanics*, 429:283, 2001.
- [24] S.V. Apte and V. Yang. A large-eddy simulation study of transition and flow instability in a porous-walled chamber with mass injection. *Journal of Fluid Mechanics*, 477:215–225, 2003.
- [25] T. Saad and J. Majdalani. On the Lagrangian optimization of wall-injected flows: from the Hart–McClure potential to the Taylor–Culick rotational motion. *Proceedings of the Royal Society A: Mathematical, Physical and Engineering Sciences*, 466(2114):331–362, 2010.
- [26] P. Venugopal, R.D. Moser, and F.M. Najjar. Direct numerical simulation of turbulence in injection-driven plane channel flows. *Physics of Fluids*, 20(10):105103, 2008.
- [27] B. Wasistho and R.D. Moser. Simulation strategy of turbulent internal flow in solid rocket motor. *Journal of Propulsion and Power*, 21(2):251–263, 2005.
- [28] J. Dupays. *Contribution à l'étude du rôle de la phase condensée dans la stabilité d'un propulseur à propergol solide pour lanceur spatial*. PhD thesis, Office national d'études et de recherches aérospatiales, 2003. URL <http://www.theses.fr/1996INPT063H>.

- [29] R.S. Brown, R. Dunlap, S.W. Young, and R.C. Waugh. Vortex shedding as a source of acoustic energy in segmented solid rockets. *Journal of Spacecraft and Rockets*, 18(4):312–319, 1981.
- [30] R. Dunlap and R.S. Brown. Exploratory experiments on acoustic oscillations driven by periodic vortex shedding. *AIAA J*, 19(3):408–409, 1981.
- [31] A. Kourta. Computation of Vortex Shedding in Solid Rocket Motors Using Time-Dependent Turbulence Model. *Journal of propulsion and power*, 15(3):390–400, 1999.
- [32] F. Vuillot and N. Lupoglazoff. Combustion and turbulent flow effects in 2D unsteady Navier-Stokes simulations of oscillatory solid rocket motors-First applications. In *34th Aerospace Sciences Meeting and Exhibit*, page 884, 1996.
- [33] F. Najjar, J. Ferry, B. Wasistho, and S. Balachandar. Full-Physics Large-Scale Multi-phase Large Eddy Simulations of Flow inside Solid Rocket Motors. In *38th AIAA/ASME/SAE/ASEE Joint Propulsion Conference & Exhibit*, page 4343, 2002.
- [34] A.D. French, M. Panelli, G. Di Lorenzo, A. Schettino, and F. Paglia. Combustion instability and pressure oscillation numerical simulation in a solid rocket motor. 2017.
- [35] J.D. Anderson. Modern Compressible Flow: With Historical Perspective (McGraw-Hill series in mechanical engineering). 1982.
- [36] J.A. Owczarek. Fundamentals of gas dynamics. international textbook company. *Scranton Penn*, 1964.
- [37] L. Nave and G. Coffey. Sea level side loads in high-area-ratio rocket engines. In *9th Propulsion Conference*, page 1284, 1973.
- [38] C.L. Chen, S.R. Chakravarthy, and C.M. Hung. Numerical investigation of separated nozzle flows. *AIAA journal*, 32(9):1836–1843, 1994.
- [39] F. Nasuti and M. Onofri. Viscous and inviscid vortex generation during nozzle flow transients. In *34th Aerospace Sciences Meeting and Exhibit*, page 76, 1996.
- [40] G. Hagemann, M. Frey, and W. Koschel. Appearance of restricted shock separation in rocket nozzles. *Journal of Propulsion and Power*, 18(3):577–584, 2002.
- [41] J. Östlund. *Flow processes in rocket engine nozzles with focus on flow separation and side-loads*. PhD thesis, 2002.
- [42] W.J. Baars, C.E. Tinney, J.H. Ruf, A.M. Brown, and D.M. McDaniels. Wall pressure unsteadiness and side loads in overexpanded rocket nozzles. *AIAA Journal*, 50(1):61–73, 2012.
- [43] R.H. Schmucker. Flow processes in overexpanded chemical rocket nozzles. Part 1: Flow separation. *NASA TM-77394*, 1984.
- [44] R.H. Schmucker. Flow process in overexpanded chemical rocket nozzles, Part 2: Side loads due to asymmetric separation. *NASA TM-77395*, 1984.

- [45] A.T. Nguyen, H. Deniau, S. Girard, and T.A. de Roquefort. Unsteadiness of flow separation and end-effects regime in a thrust-optimized contour rocket nozzle. *Flow, Turbulence and Combustion*, 71(1-4):161–181, 2003.
- [46] A. Gross and C. Weiland. Numerical simulation of separated cold gas nozzle flows. *Journal of propulsion and power*, 20(3):509–519, 2004.
- [47] S. Deck and A.T. Nguyen. Unsteady side loads in a thrust-optimized contour nozzle at hysteresis regime. *AIAA journal*, 42(9):1878–1888, 2004.
- [48] J.A. Moríñigo and J.J. Salvá. Three-dimensional simulation of the self-oscillating flow and side-loads in an over-expanded subscale rocket nozzle. *Proceedings of the Institution of Mechanical Engineers, Part G: Journal of Aerospace Engineering*, 220(5):507–523, 2006.
- [49] J. Ostlund, T. Damgaard, and M. Frey. Side-load phenomena in highly overexpanded rocket nozzles. *Journal of Propulsion and Power*, 20(4):695–704, 2004.
- [50] J. Ostlund and B. Muhammad-Klingmann. Supersonic flow separation with application to rocket engine nozzles. *Applied Mechanics Reviews*, 58(3):143–177, 2005.
- [51] G. Guderley and E. Hantsch. Beste formen fir achseymmetrische uberschallschubdiisen. *Zeitschrift für Flugwissenschaften*, 3(9), 1955.
- [52] G.V.R. Rao. Exhaust nozzle contour for optimum thrust. *Journal of Jet Propulsion*, 28(6):377–382, 1958.
- [53] G.V.R. Rao. Approximation of optimum thrust nozzle contours. *ARS J.*, 30:561, 1960.
- [54] G. Dumnov, G. Nikulin, and N. Ponomarev. Advanced rocket engine nozzles. In *32nd Joint Propulsion Conference and Exhibit*, page 3221, 1996.
- [55] G. Hagemann, H. Immich, T.V. Nguyen, and G. Dumnov. Advanced rocket nozzles. *Journal of Propulsion and Power*, 14(5):620–634, 1998.
- [56] F. Nasuti, M. Onofri, and E. Martelli. Role of wall shape on the transition in axisymmetric dual-bell nozzles. *Journal of propulsion and power*, 21(2):243–250, 2005.
- [57] E. Martelli, F. Nasuti, and M. Onofri. Numerical parametric analysis of dual-bell nozzle flows. *AIAA Journal*, 45(3):640–650, 2007.
- [58] C. Génin and R. Stark. Side loads in subscale dual bell nozzles. *Journal of Propulsion and Power*, 27(4):828–837, 2011.
- [59] F.B. Cowles and C.R. Foster. Experimental study of gas-flow separation in overexpanded exhaust nozzles for rocket motors. *NASA PR-N4-103*, 1949.
- [60] M. Horn and S. Fisher. Dual-bell altitude compensating nozzles. *NASA TR-N94-23057*, 1993.
- [61] H. Wong and R. Schwane. Numerical investigation of transition in flow separation in a dual-bell nozzle. In *Fourth Symposium on Aerothermodynamics for Space Vehicles*, volume 487, page 425, 2002.

- [62] F. Nasuti, M. Onofri, and E. Martelli. Numerical study of transition between the two operating modes of dual-bell nozzles. In *38th AIAA/ASME/SAE/ASEE Joint Propulsion Conference & Exhibit*, page 3989, 2002.
- [63] C. Génin and R. Stark. Flow transition in dual bell nozzles. *Shock Waves*, 19(3):265, 2009.
- [64] C. Génin and R. Stark. Experimental study on flow transition in dual bell nozzles. *Journal of Propulsion and Power*, 26(3):497–502, 2010.
- [65] S.B. Verma, A. Hadjadj, and O. Haidn. Unsteady flow conditions during dual-bell sneak transition. *Journal of Propulsion and Power*, 31(4):1175–1183, 2015.
- [66] D. Proschanka, Y. Koichi, H. Tsukuda, K. Araka, Y. Tsujimoto, T. Kimura, and K. Yokota. Jet oscillation at low-altitude operation mode in dual-bell nozzle. *Journal of Propulsion and Power*, 28(5):1071–1080, 2012.
- [67] D. Perigo, R. Schwane, and H. Wong. A numerical comparison of the flow in conventional and dual bell nozzles in the presence of an unsteady external pressure environment. In *39th AIAA/ASME/SAE/ASEE Joint Propulsion Conference and Exhibit*, page 4731, 2003.
- [68] L. Torngren. Correlation between outer flow and internal nozzle pressure fluctuations. In *Fourth Symposium on Aerothermodynamics for Space Vehicles*, volume 487, page 415, 2002.
- [69] H.Y.W. Wong. Theoretical prediction of resonance in nozzle flows. *Journal of Propulsion and Power*, 21(2):300–313, 2005.
- [70] S.B. Verma, R. Stark, and O. Haidn. Effect of ambient pressure fluctuations on dual-bell transition behavior. *Journal of Propulsion and Power*, 30(5):1192–1198, 2014.
- [71] I. Bolgar, S. Scharnowski, and C.J. Kähler. In-flight transition of a dual-bell nozzle–transonic vs. supersonic transition. 2019.
- [72] S. Loosen, M. Meinke, and W. Schröder. Numerical investigation of jet-wake interaction for a dual-bell nozzle. *Flow, Turbulence and Combustion*, pages 1–26, 2019.
- [73] A. Barklage, R. Radespiel, and C. Genin. Afterbody jet interaction of a dual-bell nozzle in supersonic flow. In *2018 Joint Propulsion Conference*, page 4468, 2018.
- [74] E. Martelli, B. Betti, and F. Nasuti. Flow separation response to unsteady external disturbances in dual bell nozzles. In *50th AIAA/ASME/SAE/ASEE Joint Propulsion Conference*, page 3998, 2014.
- [75] S. Loosen, M. Meinke, and W. Schröder. Numerical investigation of jet-wake interaction for a generic space launcher with a dual-bell nozzle. 2019.
- [76] C. Génin, A. Gernoth, and R. Stark. Experimental and numerical study of heat flux in dual bell nozzles. *Journal of Propulsion and Power*, 29(1):21–26, 2013.
- [77] E. Martelli, F. Nasuti, and M. Onofri. Numerical analysis of film cooling in advanced rocket nozzles. *AIAA Journal*, 47(11):2558–2566, 2009.

- [78] G.E. Dumnov. Unsteady side-loads acting on the nozzle with developed separation zone. *32nd AIAA/ASME/SAE/ASEE Joint Propulsion Conference and Exhibit*, (July):1–8, 1996.
- [79] M. Onofri, F. Nasuti, and M. Bongiorno. Shock generated vortices and pressure fluctuations in propulsive nozzles. In *36th AIAA Aerospace Sciences Meeting and Exhibit*, page 777, 1998.
- [80] M. Onofri and F. Nasuti. The physical origins of side loads in rocket nozzles. In *35th Joint propulsion conference and exhibit*, page 2587, 1999.
- [81] J. Mattsson, U. Hoegmann, and L. Torngren. A sub scale test programme on investigation of flow separation & side loads in rocket nozzles. In *Aerothermodynamics for space vehicles*, volume 426, page 373, 1999.
- [82] P. Reijasse, P. Servel, and R. Hallard. Synthesis of the 1998–1999 ONERA works in the FSCD working group. *ONERA Rept. RTS*, 49:4361, 1999.
- [83] M. Frey, R. Stark, H. Cieaki, F. Quessard, and W. Kwan. Subscale nozzle testing at the P6. 2 test stand. In *36th AIAA/ASME/SAE/ASEE Joint Propulsion Conference and Exhibit*, page 3777, 2000.
- [84] M. Frey and G. Hagemann. Restricted shock separation in rocket nozzles. *Journal of Propulsion and Power*, 16(3):478–484, 2000.
- [85] G. Hagemann and M. Frey. Shock pattern in the plume of rocket nozzles: needs for design consideration. *Shock Waves*, 17(6):387–395, 2008.
- [86] M. Frey, M. Terhardt, and G. Hagemann. Flow separation and side-load behavior of the Vulcain engine. In *35th Joint Propulsion Conference and Exhibit*, page 2762, 1999.
- [87] J. Ostlund and M. Jaran. Assessment of turbulence models in overexpanded rocket nozzle flow simulations. In *35th Joint Propulsion Conference and Exhibit*, page 2583, 1999.
- [88] S. Deck and P. Guillen. Numerical simulation of side loads in an ideal truncated nozzle. *Journal of Propulsion and Power*, 18(2):261–269, 2002.
- [89] T. Handa, M. Masuda, and K. Matsuo. Mechanism of shock wave oscillation in transonic diffusers. *AIAA journal*, 41(1):64–70, 2003.
- [90] W.J. Baars and C.E. Tinney. Transient wall pressures in an overexpanded and large area ratio nozzle. *Experiments in fluids*, 54(2):1468, 2013.
- [91] W.J. Baars, J.H. Ruf, and C.E. Tinney. Non-stationary shock motion unsteadiness in an axisymmetric geometry with pressure gradient. *Experiments in Fluids*, 56(5):92, 2015.
- [92] V. Jaunet, S. Arbos, G. Lehnasch, and S. Girard. Wall pressure and external velocity field relation in overexpanded supersonic jets. *AIAA Journal*, 55(12):4245–4257, 2017.
- [93] G. Raman. Supersonic jet screech: half-century from Powell to the present. *Journal of Sound and Vibration*, 225(3):543–571, 1999.

- [94] F. Bakulu, G. Lehnasch, V. Jaunet, E.G. da Silva, and S. Girard. Jet resonance in truncated ideally contoured nozzles. *Journal of Fluid Mechanics*, 919, 2021.
- [95] E. Martelli, L. Saccoccio, P. P. Ciottoli, C. E. Tinney, W. J. Baars, and M. Bernardini. Flow dynamics and wall-pressure signatures in a high-Reynolds-number overexpanded nozzle with free shock separation. *Journal of Fluid Mechanics*, 895:A29, 2020.
- [96] J.H. Ruf, D.M. McDaniels, and A.M. Brown. Details of side load test data and analysis for a truncated ideal contour nozzle and a parabolic contour nozzle. 2010.
- [97] M. Bernardini, M. Cimini, F. Stella, E. Cavallini, A. Di Mascio, A. Neri, and E. Martelli. Large-Eddy Simulation of Vortex Shedding and Pressure Oscillations in Solid Rocket Motors. *AIAA Journal*, 58(12):5191–5201, 2020.
- [98] M. Bernardini, M. Cimini, F. Stella, E. Cavallini, A. Di Mascio, A. Neri, F. Salvadore, and E. Martelli. Implicit Large-Eddy Simulation of Solid Rocket Motors using the Immersed Boundary Method. In *AIAA Propulsion and Energy 2021 Forum*, page 3696, 2021.
- [99] B.J. Olson and S.K. Lele. A mechanism for unsteady separation in over-expanded nozzle flow. *Physics of Fluids*, 25(11):110809, 2013.
- [100] A.D. Johnson and D. Papamoschou. Instability of shock-induced nozzle flow separation. *Physics of Fluids*, 22(1):016102, 2010.
- [101] S. Deck. Delayed detached eddy simulation of the end-effect regime and side-loads in an overexpanded nozzle flow. *Shock waves*, 19(3):239–249, 2009.
- [102] A. Shams, G. Lehnasch, P. Comte, H. Deniau, and T.A. de Roquefort. Unsteadiness in shock-induced separated flow with subsequent reattachment of supersonic annular jet. *Computers & Fluids*, 78:63–74, 2013.
- [103] E. Martelli, P.P. Ciottoli, M. Bernardini, F. Nasuti, and M. Valorani. Detached-Eddy Simulation of Shock Unsteadiness in an Overexpanded Planar Nozzle. *AIAA J*, 55(6):2016–2028, 2017.
- [104] T.J. Bogar, M. Sajben, and J.C. Kroutil. Characteristic frequencies of transonic diffuser flow oscillations. *AIAA journal*, 21(9):1232–1240, 1983.
- [105] R. Larusson, N. Andersson, and J. Östlund. Hybrid RANS-LES simulation of separated nozzle flow. In *52nd AIAA/SAE/ASEE Joint Propulsion Conference*, page 4670, 2016.
- [106] A.J. Smits and J.P. Dussauge. *Turbulent shear layers in supersonic flow*. Springer Science & Business Media, 2006.
- [107] A. Favre. Equations des Gaz Turbulents Compressibles. 2. Methode des Vitesses Moyennes Methode des Vitesses Macroscopiques Ponderees par la Masse Volumique. *Journal de Mecanique*, 4(4):391, 1965.
- [108] Langley Research Center. Implementing Turbulence Models into the Compressible RANS Equations. <https://turbmodels.larc.nasa.gov/implementrans.html> , .

- [109] P.R. Spalart and S. Allmaras. A one-equation turbulence model for aerodynamic flows. In *30th aerospace sciences meeting and exhibit*, page 439, 1992.
- [110] Langley Research Center. Spalart-Allmaras Model - Turbulence Modeling Resource. <https://turbmodels.larc.nasa.gov/spalart.html>, .
- [111] S.B. Pope. *Turbulent flows*. IOP Publishing, 2001.
- [112] P.R. Spalart, W.H. Jou, M. Strelets, and S.R. Allmaras. Comments on the feasibility of LES for wings, and on a hybrid RANS/LES approach. In *Advances in DNS/LES*, pages 137–147. Greyedn Press, 1997.
- [113] P.R. Spalart and C. Streett. Young-person’s guide to detached-eddy simulation grids. 2001.
- [114] J. Smagorinsky. General circulation experiments with the primitive equations: I. The basic experiment. *Monthly weather review*, 91(3):99–164, 1963.
- [115] K. Lilly. On the application of the eddy viscosity concept in the inertial sub-range of turbulence. *NCAR manuscript*, 123, 1966.
- [116] J.W. Deardorff. A numerical study of three-dimensional turbulent channel flow at large reynolds numbers. *Journal of Fluid Mechanics*, 41(2):453–480, 1970.
- [117] M. Germano, U. Piomelli, P. Moin, and W.H. Cabot. A dynamic subgrid-scale eddy viscosity model. *Physics of Fluids A: Fluid Dynamics*, 3(7):1760–1765, 1991.
- [118] E. Garnier, M. Mossi, P. Sagaut, P. Comte, and M. Deville. On the use of shock-capturing schemes for large-eddy simulation. *Journal of Computational Physics*, 153(2):273–311, 1999.
- [119] F.F. Grinstein, L.G. Margolin, and W.J. Rider. *Implicit large eddy simulation: computing turbulent fluid dynamics*. Cambridge university press, 2007. ISBN 9780521869829.
- [120] D.C. Wilcox et al. *Turbulence modeling for CFD*, volume 2. DCW industries La Canada, CA, 2006.
- [121] P. Sagaut, S. Deck, and M. Terracol. *Multiscale and multiresolution approaches in turbulence: LES, DES and hybrid RANS/LES methods: applications and guidelines*. World Scientific, 2013.
- [122] J. Fröhlich and D. von Terzi. Hybrid LES/RANS methods for the simulation of turbulent flows. *Progress in Aerospace Sciences*, 44(5):349–377, 2008.
- [123] M. Strelets. Detached eddy simulation of massively separated flows. In *39th Aerospace sciences meeting and exhibit*, page 879, 2001.
- [124] S. Deck. Recent Improvements in the Zonal Detached Eddy Simulation (ZDES) Formulation. *Theoretical and Computational Fluid Dynamics*, 26(6):523–550, 2012.
- [125] P.R. Spalart et al. The uses of DES: natural, extended, and improper. In *Invited presentation at the DESider Hybrid RAN-LES Symposium, Stockholm, Sweden*, 2005.

- [126] C. Mockett. *A Comprehensive Study of Detached Eddy Simulation*. Univerlagtuberlin, 2009.
- [127] N.V. Nikitin, F. Nicoud, B. Wasistho, K.D. Squires, and P.R. Spalart. An approach to wall modeling in large-eddy simulations. *Physics of fluids*, 12(7):1629–1632, 2000.
- [128] P.R. Spalart. Detached-Eddy Simulation. *Annual review of fluid mechanics*, 41:181–202, 2009.
- [129] P.R. Spalart, S. Deck, M.L. Shur, K.D. Squires, M.K. Strelets, and A. Travin. A new version of detached-eddy simulation, resistant to ambiguous grid densities. *Theoretical and computational fluid dynamics*, 20(3):181–195, 2006.
- [130] F.R. Menter and M. Kuntz. Adaptation of eddy-viscosity turbulence models to unsteady separated flow behind vehicles. In *The aerodynamics of heavy vehicles: trucks, buses, and trains*, pages 339–352. Springer, 2004.
- [131] M.L. Shur, P.R. Spalart, M.K. Strelets, and A.K. Travin. An enhanced version of DES with rapid transition from RANS to LES in separated flows. *Flow Turb. Combust.*, 95(4):709–737, 2015.
- [132] M.S. Gritskevich, A.V. Garbaruk, J. Schütze, and F.R. Menter. Development of DDES and IDDES Formulations for the $k-\omega$ Shear Stress Transport Model. *Flow, turbulence and combustion*, 88(3):431–449, 2012.
- [133] M.S. Gritskevich, A.V. Garbaruk, and F.R. Menter. Fine-tuning of DDES and IDDES Formulations to the $k-\omega$ Shear Stress Transport Model. *Progress in Flight Physics*, 5:23–42, 2013.
- [134] C. Hirsch. *Numerical computation of internal and external flows. Fundamentals of numerical discretization*, volume 1. John Wiley & Sons, 1988.
- [135] S. Pirozzoli. Generalized conservative approximations of split convective derivative operators. *Journal of Computational Physics*, 229(19):7180–7190, 2010.
- [136] S. Pirozzoli. Numerical methods for high-speed flows. *Annu. Rev. Fluid Mech.*, 43:163–194, 2011.
- [137] G.A. Blaisdell, E.T. Spyropoulos, and J.H. Qin. The effect of the formulation of nonlinear terms on aliasing errors in spectral methods. *Applied Numerical Mathematics*, 21(3):207–219, 1996.
- [138] C.A. Kennedy and A. Gruber. Reduced aliasing formulations of the convective terms within the Navier–Stokes equations for a compressible fluid. *Journal of Computational Physics*, 227(3):1676–1700, 2008.
- [139] G.S. Jiang and C.W. Shu. Efficient implementation of weighted ENO schemes. *Journal of computational physics*, 126(1):202–228, 1996.
- [140] F. Ducros, V. Ferrand, F. Nicoud, C. Weber, D. Darracq, C. Gachet, and T. Poinsot. Large-Eddy Simulation of the Shock/Turbulence Interaction. *Journal of Computational Physics*, 152(2):517–549, 1999.

- [141] C.W. Shu. High-order finite difference and finite volume WENO schemes and discontinuous Galerkin methods for CFD. *International Journal of Computational Fluid Dynamics*, 17(2):107–118, 2003.
- [142] R.M. Beam and R.F. Warming. An implicit finite-difference algorithm for hyperbolic systems in conservation-law form. *Journal of computational physics*, 22(1):87–110, 1976.
- [143] R.M. Beam and R.F. Warming. An implicit factored scheme for the compressible Navier-Stokes equations. *AIAA journal*, 16(4):393–402, 1978.
- [144] P.L. Roe. Approximate Riemann solvers, parameter vectors, and difference schemes. *Journal of computational physics*, 43(2):357–372, 1981.
- [145] P. Orlandi. *Fluid flow phenomena: a numerical toolkit*, volume 55. Springer Science & Business Media, 2012.
- [146] T.J. Poinsot and S.K. Lele. Boundary conditions for direct simulations of compressible viscous flows. *Journal of computational physics*, 101(1):104–129, 1992.
- [147] R.J. LeVeque. Finite-volume methods for non-linear elasticity in heterogeneous media. *International journal for numerical methods in fluids*, 40(1-2):93–104, 2002.
- [148] S. Pirozzoli and T. Colonius. Generalized characteristic relaxation boundary conditions for unsteady compressible flow simulations. *Journal of Computational Physics*, 248:109–126, 2013.
- [149] T.A. Driscoll and S.A. Vavasis. Numerical conformal mapping using cross-ratios and Delaunay triangulation. *SIAM Journal on Scientific Computing*, 19(6):1783–1803, 1998.
- [150] M. Bernardini and S. Pirozzoli. A General Strategy for the Optimization of Runge-Kutta Schemes for Wave Propagation Phenomena. *Journal of Computational Physics*, 228(11):4182–4199, 2009.
- [151] J. Boris, F.F. Grinstein, E. Oran, and R. Kolbe. New insights into Large Eddy Simulation. *Fluid Dyn Res*, 10:199–228, 1992.
- [152] C. Fureby and F.F. Grinstein. Large Eddy Simulation of high-Reynolds number free and wall-bounded flows. *Journal of Computational Physics*, 181(1):68–97, 2002.
- [153] E. Martelli, P. P. Ciottoli, L. Saccoccia, F. Nasuti, M. Valorani, and M. Bernardini. Characterization of unsteadiness in an overexpanded planar nozzle. *AIAA Journal*, 57(1):239–251, 2019.
- [154] F.E.C. Culick. Rotational axysymmetric mean flow and damping of acoustic waves in solid propellant rocket motors. *AIAA J*, 4:1462–1464, 1966.
- [155] W.E. Wageman and F.A. Guevara. Fluid flow through a porous channel. *Phys. of Fluids*, 3(6):878881, 1960.
- [156] K. Yamada, M. Goto, and N. Ishikawa. Simulative study on the erosive burning of solid rocket motors. *AIAA J*, 14:1170–1176, 1976.

- [157] R. Dunlap, P.G. Willoughby, and R.W. Hermsenr. Flowfield in the combustion chamber of a solid propellant rocket motor. *AIAA J.*, 12:1440–1442, 1974.
- [158] R.A. Beddini. Injection-induced flows in porous-walled ducts. *AIAA J.*, 24(11):1766–1773, 1986.
- [159] J. C. Hunt, A. A. Wray, and P. Moin. Eddies, stream, and convergence zones in turbulent flows. *Center for turbulence Research Report*, pages 193–208, 1988. URL <https://ntrs.nasa.gov/search.jsp?R=19890015184>.
- [160] F. Vuillot, N. Lupoglazoff, and J. Dupays. Simulation numerique du detachement tourbillonnaire dans un MPS: Premiere validation sur le Cas C1xb 3 mm brules. ONERA, TR RT 82/6133 EY, 1998.
- [161] K. Konno and T. Ohmachi. Ground-motion characteristics estimated from spectral ratio between horizontal and vertical components of microtremor. *Bulletin of the Seismological Society of America*, 88(1):228–241, 1998.
- [162] W.W. Willmarth. Pressure fluctuations beneath turbulent boundary layers. *Annual Review of Fluid Mechanics*, 7(1):13–36, 1975.
- [163] M. Bernardini and S. Pirozzoli. Wall pressure fluctuations beneath supersonic turbulent boundary layers. *Physics of Fluids*, 23(8):085102, 2011.
- [164] J.A.B. Wills. On convection velocities in thurbulent shear flows. *J. Fluid Mech.*, 20:417–432, 1964.
- [165] A. Flatau and W. VanMoorhem. Prediction of vortex shedding responses in segmented solid rocket motors. AIAA Paper 90-2073, 1990.
- [166] K.W. Dotson, S. Koshigoe, and K.K. Pace. Vortex shedding in a large solid rocket motor without inhibitors at the segment interfaces. *Journal of Propulsion and Power*, 13(2):197–206, 1997.
- [167] J.E. Rossiter. Wind-tunnel experiments on the flow over rectangular cavities at subsonic and transonic speeds. Aeronautical research council, ministry of aviation, reports and memoranda 3438, 1964. URL <http://resolver.tudelft.nl/uuid:a38f3704-18d9-4ac8-a204-14ae03d84d8c>.
- [168] A. Powell. On the Mechanism of Choked Jet Noise. *Proceedings of the Physical Society. Section B*, 66(12):1039–1056, 1953.
- [169] D. Rockwell. Oscillations of impinging shear layers. *AIAA J.*, 21(5):645–664, 1983.
- [170] S. Pirozzoli, M. Bernardini, and F. Grasso. Characterization of coherent vortical structures in a supersonic turbulent boundary layer. *J. Fluid Mech.*, 613:205–231, 2008.
- [171] N. D. Sandham and W. C. Reynolds. Three-dimensional simulations of large eddies in the compressible mixing layer. *J. Fluid Mech.*, 224:133–158, 1991.

- [172] F. Simon, S. Deck, P. Guillen, P. Sagaut, and A. Merlen. Numerical simulation of the compressible mixing layer past an axisymmetric trailing edge. *J. Fluid Mech.*, 591:215–253, 2007.
- [173] C. Pantano and S. Sarkar. A study of compressibility effects in the high-speed turbulent shear layer using direct simulation. *J. Fluid Mech.*, 451:329–371, 2002.
- [174] D. S. Dolling and C. T. Or. Unsteadiness of the shock wave structure in attached and separated compression ramp flows. *Exp. Fluids*, 3(1):24–32, 1985.
- [175] C.K.W. Tam, J.M. Seiner, and J.C. Yu. Proposed relationship between broadband shock associated noise and screech tones. *Journal of Sound and Vibration*, 110(2):309 – 321, 1986.
- [176] H. Tennekes and J.L. Lumley. *A first course in turbulence*. MIT press, 1972.
- [177] C.W. Shu. Finite Volume WENO Schemes. <http://dauns.math.tulane.edu/~kurganov/CliffordLectures2013/Shu1.pdf>.